

ABSTRACT

Title of Document: INTEGRATION AND
CHARACTERIZATION OF TOBACCO
MOSAIC VIRUS BASED
NANOSTRUCTURED MATERIALS IN
THREE-DIMENSIONAL MICROBATTERY
ARCHITECTURES

Konstantinos Gerasopoulos, Doctor of
Philosophy, 2012

Directed By: Professor Reza Ghodssi, Department of
Materials Science and Engineering

The realization of next-generation portable electronics, medical implants and miniaturized, autonomous microsystems is directly linked with the development of compact and efficient power sources and energy storage devices with high energy and power density. As the components of these devices are continuously scaled down in size, there is a growing demand for decreasing the size of their power supply as well, while maintaining performance comparable to larger assemblies.

This dissertation presents a novel approach for the development of microbattery electrodes that is based on integrating both micro and nano structured components for the formation of hierarchical electrodes. These electrodes combine both high energy density (enabled by the high surface area and mass loading) with high power density (due to the small thickness of the active battery materials). The key building block

technologies in this work are the bottom-up self-assembly and metallization of a biological template and the top-down microfabrication processes enabled by Microelectromechanical Systems (MEMS) technology. The biotemplate used is the *Tobacco mosaic virus* (TMV), a rod-like particle that can be genetically modified to express functional groups with enhanced metal binding properties. In this project, this feature is combined with standard microfabrication techniques for the synthesis of nanostructured energy-related materials as well as their hierarchical patterning in device architectures. Specifically, synthesis of anode (TiO_2) and cathode (V_2O_5) materials for Li-ion batteries in a core/shell configuration is presented, where the TMV biomineralization is combined with atomic layer deposition of the active material. These nanostructured electrodes demonstrate high energy storage capacities, high rate capabilities and superior performance to electrodes with planar geometries. In addition, a toolbox of biofabrication processes for the defined patterning of virus-templated structures has been developed. Finally, the nanocomposite electrodes are integrated with three-dimensional micropillars to form hierarchical electrodes that maintain the high rate performance capabilities of nanomaterials while exhibiting an increase in energy density compared to nanostructures alone. This is in accordance with the increase in surface area added by the microstructures. Investigation of capacity scaling for varying active material thickness reveals underlying limitations in nanostructured electrodes and highlights the importance of this method in controlling both energy and power density with structural hierarchy. These results present a paradigm-shifting technology for the fabrication of next-generation microbatteries for MEMS and microsystems applications.

INTEGRATION AND CHARACTERIZATION OF TOBACCO MOSAIC VIRUS
BASED NANOSTRUCTURED MATERIALS IN THREE-DIMENSIONAL
MICROBATTERY ARCHITECTURES

By

Konstantinos Dimitriou Gerasopoulos

Dissertation submitted to the Faculty of the Graduate School of the
University of Maryland, College Park, in partial fulfillment
of the requirements for the degree of
Doctor of Philosophy
2012

Advisory Committee:
Professor Reza Ghodssi, Chair
Professor Robert Briber
Professor Sheryl Ehrman
Professor Raymond Phaneuf
Professor Chunsheng Wang

© Copyright by
Konstantinos Dimitriou Gerasopoulos
2012

Dedication

...To my wife Irene, my parents, Dimitri and Eleni, and my brother, Vasili, for their love and support throughout the years. Also, Professor Maria Klapa, without whom none of this would have been possible...

Acknowledgements

I would like to acknowledge the help and contributions of my advisor, Professor Reza Ghodssi for his guidance and support throughout the course of this work. I would like to thank my Ph.D. Dissertation Committee members, Professor Robert Briber, Professor Sheryl Ehrman, Professor Raymond Phaneuf, and Professor Chunsheng Wang for their suggestions and feedback in shaping this work. I am grateful to the various sponsors of this research throughout the years, more specifically the Laboratory for Physical Sciences (LPS), the Maryland Technology Development Corporation, the National Science Foundation and the Department of Energy – Energy Frontiers Research Center at the University of Maryland.

A huge acknowledgement is due to all my close collaborators from the beginning of my Ph.D. career. Particularly, I would like to thank Professor James Culver, Professor Matthew McCarthy, Dr. Elizabeth Royston, Mr. Adam Brown, Dr. Xilin Chen, Dr. Juchen Guo, Mr. Xiaozhu Fan, Dr. Ekaterina Pomerantseva and Professor Parag Banerjee for their valuable contributions to my research accomplishments. I would like to acknowledge the assistance I received in the fabrication and characterization from the LPS clean room staff, the Maryland Nanocenter personnel (Dr. Jim O’Connor, Dr. Wen-An Chou, Dr. Li-Chung Lai, Mr. Tom Loughran, Mr. John Abrahams, and Mr. Jonathan Hummel). I would like to thank all the members of Professor Culver’s and Professor Wang’s Laboratories for providing generous help when necessary. I am extremely grateful to all the useful discussions, feedback and support I received from all my colleagues at the MEMS Sensors and Actuators Laboratory throughout the years,

Last but not least, I am grateful to my wife, Irene, my parents, Dimitri and Eleni, my brother Vasili, and my in-laws, George, Fotini and Maria, for all kinds of support they provided in the last 5 years.

Table of Contents

Contents

| | |
|--|-----|
| Dedication | ii |
| Acknowledgements | iii |
| Table of Contents | v |
| List of Tables | ix |
| List of Figures | x |
| Chapter 1 : Introduction | 1 |
| 1.1 Motivation | 2 |
| 1.2 Thesis Contributions | 6 |
| 1.3 Literature Review | 8 |
| 1.3.1 Other approaches for micro-power applications | 8 |
| 1.3.2 2D Microbatteries | 12 |
| 1.3.3 3D Microbatteries | 17 |
| 1.3.4 Nanostructured Micro/nano Batteries | 21 |
| 1.4 Thesis Objective and Structure | 26 |
| Chapter 2 : Review of Related Concepts and Processes | 28 |
| 2.1 Fundamentals of Battery Operation | 28 |
| 2.2 Biotemplating Processes | 32 |
| 2.3 The Tobacco mosaic virus | 35 |
| 2.3.1 General Background | 35 |
| 2.3.2 TMV Applications | 39 |

| | |
|---|----|
| 2.4 Patterning of Biological Materials | 43 |
| 2.5 1 st Generation TMV Microbattery | 45 |
| 2.6 Summary | 48 |
| Chapter 3 : Biofabrication Processes for the Patterned Assembly and Synthesis of Viral Nanotemplates | 50 |
| 3.1 Photolithographic Patterning of TMV | 51 |
| 3.1.1 Nickel-coated TMV Patterning | 52 |
| 3.1.2 Uncoated TMV Patterning | 55 |
| 3.2 Assembly on Three-dimensional Geometries | 61 |
| 3.3 Synthesis of Core/Shell Nanostructures Using the TMV | 64 |
| 3.4 Example: TMV Biofabrication for Superhydrophobic Surfaces | 68 |
| 3.5 Summary | 70 |
| Chapter 4 : Nanocomposite Virus-structured Core/Shell Electrodes for Li-ion Battery Applications | 72 |
| 4.1 Nanocomposite TMV/Ni/TiO ₂ Anodes | 73 |
| 4.1.1 Synthesis and Structural Characterization | 75 |
| 4.1.2 Electrochemical Characterization | 78 |
| 4.2 Virus-templated Ni/V ₂ O ₅ cathodes | 87 |
| 4.3 Virus-structured TMV/Ni/Si Anodes | 91 |
| 4.4 Summary | 93 |
| Chapter 5 : Three-dimensional, Hierarchical Microbattery Electrodes Using the TMV | 94 |
| 5.1 Design Considerations | 95 |

| | |
|--|-----|
| 5.2 Device Fabrication | 97 |
| 5.2.1 General Fabrication Scheme | 97 |
| 5.2.2 Mold Fabrication with KMPR | 98 |
| 5.2.3 Mold Fabrication with AZ 9260 | 101 |
| 5.2.3 Gold Electroplating..... | 103 |
| 5.2.4 TMV Nanostructure Assembly and Active Material Deposition | 105 |
| 5.3 Surface Area Enhancement Estimation | 110 |
| 5.4 Electrochemical Testing Results – Teflon/Stainless Steel Cell (TiO ₂ active material) | 115 |
| 5.5 Electrochemical Testing Results – Coin Cells (V ₂ O ₅ active material)..... | 121 |
| 5.5.1 Changes from Previous Set-up..... | 121 |
| 5.5.2 Energy Density Analysis..... | 123 |
| 5.5.3 Power Density Analysis..... | 131 |
| 5.6 Discussion on the Hierarchical Electrodes | 132 |
| 5.7 Summary | 135 |
| Chapter 6 : Summary and Future Work..... | 136 |
| 6.1 Summary of Work..... | 136 |
| 6.2 Summary of Accomplishments..... | 139 |
| 6.3 Future Outlook | 140 |
| 6.3.1 TMV coating..... | 141 |
| 6.3.2 Higher aspect ratio electrodes | 141 |
| 6.3.3 All-solid-state virus-structured microbatteries | 142 |
| Bibliography | 145 |

List of Tables

| | |
|---|----|
| TABLE 1: SUMMARY OF 2D MICROBATTERIES | 16 |
| TABLE 2: SUMMARY OF 3D MICROBATTERIES | 21 |
| TABLE 3: SUMMARY OF NANOSTRUCTURED MICROBATTERIES | 25 |

List of Figures

| | |
|--|----|
| Figure 1.1: a. Conceptual schematic of a smart-dust mote; b. SEM image showing a microsystem [2] | 2 |
| Figure 1.2: Parameters for the power requirements of a microsystem powered by a hybrid power supply [4]..... | 3 |
| Figure 1.3: Schematic of a (a) 2D parallel plate and a (b) tubular 3D battery showing the dimensions for the typical components [5] | 4 |
| Figure 1.4: (a) Process flow for the fabrication of carbide-derived carbon electrodes [12], (b) SEM of carbonized SU-8 pillars [10], (c) schematic of CNT-forest supercapacitor [11]..... | 10 |
| Figure 1.5: (a) High surface catalytic surface for SOFC using etching and ALD deposition [13], (b) optical image of a fuel cell microreactor [14]..... | 10 |
| Figure 1.6: (a) Schematic of the electromagnetic generator described in [19], (b) image of the thermoelectric generator structure of [22] and (c) cross-sectional view of a cantilever for piezoelectric energy harvesting [20]..... | 11 |
| Figure 1.7: (a) SEM image of the primary battery described in [23], (b) SEM image of the Mg/AgCl battery with water as the electrolyte [24], (c) SEM image of the side-by-side Ni/Zn microbattery of [26], and (d) schematic of the integrated intraocular pressure sensor system [28] | 14 |
| Figure 1.8: 2D Microbatteries with solid and polymer electrolytes; (a) in-situ cell image of the Oak Ridge 2D battery before testing, after first charge, and after first discharge, [30], (b) interdigitated sol-gel microbattery[33], (c) ink-jet printed microbattery[34] | 15 |

| | |
|--|----|
| Figure 1.9: C-MEMS carbon electrodes for 3-D microbatteries; (a) meso-carbon micro-beads on carbonized SU-8 posts [7], (b) SEM image showing full cell carbon-polypyrrole microbattery [35]..... | 17 |
| Figure 1.10: (a) image of meso-carbon micro-bead paste electrodes formed into pillars inside a silicon mold, (b) electroplated zinc microposts for a zinc-air microbattery [5] | 19 |
| Figure 1.11: (a) SEM image showing a perforated glass substrate mold [40], (b) SEM image showing the mold of (a) filled with the active materials, (c) SEM image showing LiCoO_2 (left) and $\text{Li}_4\text{Mn}_5\text{O}_{12}$ (right) sols inside a ceramic electrolyte [42], (d) cross section SEM image inside a silicon pore showing the current collector (TiN) and anode material (poly-Si) [46] | 20 |
| Figure 1.12: (a) Concept of nanorod fabrication in PC membrane template as presented in [47], (b) SEM image of Al/LiCoO ₂ nanorods [50], (c) TEM image of Al/TiO ₂ nanorods [51], (d) CNTs grown on AAO templates [48] | 23 |
| Figure 1.13: Schematic demonstration of a composite anode showing carbon nanofiber (a) and Si deposition (b) on a stainless steel substrate [56], (c) top-view and (d) cross-section SEM images of titania nanotubes [53] | 24 |
| Figure 1.14: Conceptual high - level approach describing the dissertation objective | 26 |
| Figure 2.1: Schematic showing operation of a commercial Li-ion battery [9]..... | 29 |
| Figure 2.2: Schematic showing the different length scales, shapes, and particles involved in biotemplating processes [61] | 33 |

Figure 2.3: (a) AFM image of selective DNA metallization through the use of the blocking RecA protein [80], (b) Co_3O_4 nanowire formed on the M13 bacteria virus [81]..... 34

Figure 2.4: : (a) TEM images of wild type viruses, (b) simplified schematic of the TMV structure [84]..... 36

Figure 2.5: Model of the TMV disk showing the various amino acids. Hydrophilic amino acids are colored white, water molecules are colored blue, polar hydrophilic amino acids have a green color and the charged hydrophilic ones are red [86] 37

Figure 2.6: Structural location of the TMV1cys mutation: (a) Top view showing half of a coat protein layer within the TMV rod and (b) 2X magnification of an edge view for the same coat protein layer..... 39

Figure 2.7: Synthesis of (a) nickel and (b) cobalt nanowires on the TMV [87]; (c) digital memory device using TMV templates [94]..... 40

Figure 2.8: (a) SEM image of Ni-coated TMV attached on a Au surface, (b) cross-section TEM of the Ni-coated TMV [91], (c) improved Pt cluster deposition on TMV2cys compared to wild type TMV [85]..... 42

Figure 2.9: (a) Patterning of TMV using micro-contact printing [101], (b) assembly of biomolecules using dip-pen nanolithography [99] 44

Figure 2.10: Conceptual schematic of TMV assembly using DNA hybridization on chitosan functionalized sites [107]..... 45

Figure 2.11: (a) Three-dimensional schematic of the 1st generation microbattery, (b) optical image of the microfluidic package developed for electrolyte circulation showing the microbattery with the fluidic and electrical connections..... 46

| | |
|--|----|
| 2.12: Charge/discharge curves for a TMV-structured Ni-Zn microbattery showing the first eight cycles of operation..... | 47 |
| 2.13: Capacity vs. cycle number for the device of 2.12..... | 47 |
| Figure 2.14: Voltage vs. capacity for microbatteries containing electrodes with and without TMV | 48 |
| Figure 3.1: Schematic representation of the lift-off patterning processes for nickel-coated TMV (a), uncoated TMV (b) and uncoated TMV with an etched recess – (a) Coated TMV: e-beam evaporation of Ti/Au (i), photolithography with positive or negative photoresist (ii), TMV assembly and Ni coating (iii) and removal of photoresist in acetone (iv). (b) Uncoated TMV: photolithography with positive photoresist (i), Ti/Au evaporation (ii), TMV assembly (iii), lift-off of Au and TMV in a developer mixture or acetone (iv). (c) Uncoated TMV. After photolithography, a shallow recess (1 μm) is etched using DRIE (i), steps (ii), (iii) and (iv) are identical | 52 |
| Figure 3.2: Generalized schematic of the TMV self-assembly and nickel-coating process..... | 53 |
| Figure 3.3: SEM images of patterned nickel-coated TMV features; (a) microfabricated virus-coated lines with size and spacing of 2 μm and (b) close up view of the textured surface..... | 54 |
| Figure 3.4: Images of TMV coated chips patterned in developer:buffer 1:5 mixture (left column) and acetone (right column) (a, e) optical images of chip surface showing that coated gold has been removed selectively, (b, f) AFM height scans of an untreated control surface cleaved from the same substrate before immersion in the | |

respective patterning solution, (c, g) AFM height scans of the gold surfaces of figures (a) and (e) and (d, h) AFM height scans of the silicon surfaces of (a) and (e) 58

Figure 3.5: AFM height scans of the interface between gold and silicon of chips patterned in a 1:3 developer/buffer mixture (a) and acetone (c). Figures (b) and (d) show the phase mode AFM scans for (a) and (c) respectively 59

Figure 3.6: SEM images of TMV that was first patterned in 5:1 buffer:developer mixture (a) and acetone (b) and then coated with nickel to verify post-patterning chemical functionality. Images (c) and (d) show close-up views of the textured surfaces 60

Figure 3.7: SEM images of three-dimensional microstructures covered with nickel-coated TMV, (a) SU-8 structures, (b) structures etched in silicon. Bottom pictures (c) and (d) show exploded views of the textured surfaces outlined by the dotted areas in (a) and (b)..... 63

Figure 3.8: (a) Cleaved high aspect ratio structures in silicon, examples of (b) uniformly covered sidewall and (c) poorly covered sidewall); (d) a similar structure coated with constant stirring of solutions; close-up views of top (e) and sidewall (f) surfaces of (d) 64

Figure 3.9: SEM images of patterned nickel-coated TMV structures before (a) and after (b) ALD coating of TiO_2 – The diameter of particles 1 to 3 has been measured using ImageJ software to be 151 nm, 149 nm, 144 nm in (a) and 214 nm, 206 nm, 197 nm in (b)..... 66

Figure 3.10: Side (a) and bottom (b) view TEM images of TMV particles coated with layers of nickel (electroless plating) and Al_2O_3 (ALD) – EDS line scan data of the

STEM image (c) are shown on the right for the elements of interest (Al, Ni, O). It can be seen that aluminum signal is picked from the start of the line scan (d) while nickel signal is zero until ~25 nm (e); this indicates that the first coating layer is due to ALD of Al₂O₃ - oxygen (f) is due to both materials 67

Figure 3.11: SEM images showing (a) biomimetic hierarchical microstructures of the lotus plant leaf and (b) the actual lotus plant leaf [111] (Work led by Dr. Matthew McCarthy, MIT/Drexel)..... 69

Figure 4.1: (a) SEM image of the nanocomposite anode on the current collector; (b) cross-section TEM image of a single viral nanorod showing the TMV (18nm), Ni (~20nm) and TiO₂ (~20nm) 76

Figure 4.2: STEM image and EDS spectra of a viral nanorod electrode..... 77

Figure 4.3: XRD data for three samples: Ni-coated TMV only, Ni/TiO₂-coated TMV (as prepared), and Ni/TiO₂-coated TMV (annealed at 450°C) 77

Figure 4.4: CV scans for electrodes with (green) and without (red) TMV at a rate of 0.5 mVs⁻¹; the inset is an exploded view of the planar sample..... 79

Figure 4.5: Charge/discharge curves for the virus-structured anode at a rate of 147 mAg⁻¹ for the 1st, 2nd and 650th cycle..... 80

Figure 4.6: Graph showing the 1st and 2nd charge/discharge curves for the TMV/Ni/TiO₂ electrodes as well as the 1st cycle for a control sample without the TiO₂ layer (TMV/Ni) 82

Figure 4.7: CV scans for the first (a) and second (b) cycles for the synthesized TMV/Ni/TiO₂ nanocomposite anode (green) and a control sample without the TiO₂ layer (TMV/Ni, red) obtained in the range of 1-2.6 V at a rate of 0.5 mVs⁻¹ 83

| | |
|--|----|
| Figure 4.8: Capacity vs. cycle number for electrodes with and without TMV..... | 84 |
| Figure 4.9: : SEM image of the nanostructured anode that was cycled at the 500 mA g^{-1} rate after completion of approximately 850 cycles | 84 |
| Figure 4.10: Rate capability for electrodes with and without TMV | 85 |
| Figure 4.11: EIS data for electrodes with and without TMV cycled at 150 mA g^{-1} . The data were collected at open circuit potential before cycling and after the 12th discharge | 86 |
| Figure 4.12: XRD patterns for flat and TMV-templated V ₂ O ₅ electrodes on stainless steel disks | 88 |
| Figure 4.13: Cross-section TEM and EDS signals showing the uniform coverage of the V ₂ O ₅ on the nickel-coated TMV template; the thickness is ~ 30 nm [124]..... | 89 |
| Figure 4.14: Capacity vs. cycle number for TMV/Ni/V ₂ O ₅ electrodes with and without TMV [124]..... | 90 |
| Figure 4.15: (a) TEM image of a vertically aligned TMV/Ni/Si nanoparticle after 45 min of silicon sputtering, including EDS profiles of the different films, (b) high resolution TEM image of the circled area in (a), (c) FFT signal of the circled area in (b), (d) TEM image of non-vertically aligned TMV nanorod [113]..... | 91 |
| Figure 4.16: Capacity vs. cycle number and coulombic efficiency vs. cycle number for a TMV templated Si anode at 2A/g [113] | 92 |
| Figure 5.1: General 3-D electrode fabrication process;(a) mold patterning, (b) electroplating, (c) mold dissolution, (d) TMV self-assembly, metallization, and ALD of active material..... | 97 |

| | |
|--|-----|
| Figure 5.2: SEM image showing the impact of non-uniform KMPR spin on the hole development..... | 100 |
| Figure 5.3: Characteristic SEM of attempt in KMPR mold removal after 1 hour treatment in Remover PG and O ₂ plasma showing residues remaining across the wafer | 101 |
| Figure 5.4: Cross section SEM image showing the photoresist mold fabricated with the AZ 9260 process | 103 |
| Figure 5.5: Optical image of the electroplating set up showing the tank on the hot plate and with the wafer and counter electrode marked | 104 |
| Figure 5.6: (a) optical image showing the top of electroplated micropillars through the photoresist mold, (b) SEM image of the gold micropillars after photoresist removal | 105 |
| Figure 5.7: (a) Orthogonal view of a hierarchical electrode, (b) close up view of four micropillars shown in (a), (c) image showing the bottom of a micropillar, (d) close up view of the top of a micropillar..... | 106 |
| Figure 5.8: TEM image taken from the sidewall of a micropillar showing the uniform V ₂ O ₅ coating across the entire geometry, regardless of the particle orientation | 107 |
| Figure 5.9: SEM images of nickel-coated TMV substrates at different concentrations: (a) - (c) at 0.1 g/L, (d) - (f) at 0.2 g/L, and (g) through (i) at 0.2 g/L and 0.1 g/L. The particle count in 1 μm ² cross sections for each of these samples was 46 to 47, showing no significant variation..... | 108 |
| Figure 5.10: Characteristic top and side view SEM images used to determine the pillar dimensions..... | 111 |

Figure 5.11: Bar graph plotting the average V_2O_5 mass deposited after 1000 ALD cycles on four types of samples including flat substrates, substrates with micropillars only, nanostructures only, and hierarchical electrodes 113

Figure 5.12: Bar graph plotting the average TiO_2 mass deposited after 400 ALD cycles on four types of samples including flat substrates, substrates with micropillars only, nanostructures only, and hierarchical electrodes 114

Figure 5.13: Optical image showing the custom-designed electrochemical cell used for the first generation of testing; the numbers I, II, III, indicate the three different components involved in the cell assembly..... 116

Figure 5.14: Assembled package under test showing the electrical connections to the electrodes. In this image, the electrical sealing tape as well as the epoxy used to glue the brass pins are also visible..... 118

Figure 5.15: Discharge/charge for a hierarchical electrode cycled at constant current density of $26.5 \mu Ah/cm^2$ 119

Figure 5.16: Discharge capacity vs. cycle number for hierarchical and nanostructured only electrodes cycled at a constant current density of $13 \mu Ah/cm^2$ 120

Figure 5.17: Optical image showing the silicon chip inside the coin cell components along with a packaged coin cell in the battery holder used for testing 123

Figure 5.18: XRD data for V_2O_5 material deposited on three different substrates... 124

Figure 5.19: CV scans for hierarchical and nanostructured only electrodes with V_2O_5 active material taken in the 2.6 V to 3.6 V range with a 0.5 mV/s sweep rate..... 125

| | |
|---|-----|
| Figure 5.20: Characteristic discharge/charge curves during the 2nd cycle for hierarchical and nanostructured only electrodes with 30 nm of V ₂ O ₅ (1000 ALD cycles)..... | 126 |
| Figure 5.21: Capacity vs. cycle number for the first 35 cycles of operation for the electrodes shown in Figure 5.20 | 126 |
| Figure 5.22: Galvanostatic discharge/charge curves for hierarchical electrodes at a current of 12 μA; V ₂ O ₅ was deposited for 1000, 2000, and 4000 ALD cycles, aiming at thicknesses of 30 nm, 60 nm, and 120 nm, respectively..... | 128 |
| Figure 5.23: Added mass measurements for hierarchical electrodes containing V ₂ O ₅ with different thicknesses; 1000, 2000, and 4000 ALD cycles correspond to thicknesses of 30 nm, 60 nm, and 120 nm, respectively..... | 128 |
| Figure 5.24: SEM images showing the top of micropillars for, a, 1000 ALD cycles of V ₂ O ₅ , b, 2000 ALD cycles of V ₂ O ₅ , c, 4000 ALD cycles of V ₂ O ₅ | 129 |
| Figure 5.25: Cross-section TEM images of hierarchical electrodes with (a) 2000 ALD cycles and (b) 4000 ALD cycles of V ₂ O ₅ | 130 |
| Figure 5.26: Average capacities for hierarchical and nanostructured only electrodes with 30 nm of V ₂ O ₅ (1000 ALD cycles) at different current values (reminder: footprint is 1.1 cm ²) | 131 |
| Figure 5.27: (a) Capacity vs. cycle number for electrodes with and without micropillars at different C-rates, (b) rate capability for the electrodes shown in (a) (V ₂ O ₅ thickness is 30 nm - 1000 ALD cycles) | 132 |
| Figure 6.1: Conceptual schematic of envisioned battery architecture on a single virus nanoparticle..... | 143 |

Chapter 1 : Introduction

MicroElectroMechanical Systems (MEMS) is a relatively new engineering field that is aiming towards the miniaturization of sensors, actuators and systems, following a trend similar to the one that sparked the electronic industry revolution after the 1950s. While the acronym in the early days was used to refer to devices with electrical and movable components, continuous research has led to the development of various new applications that span from life sciences and bioengineering (BioMEMS and micro-total analysis systems) to small-scale power generation and energy conversion (PowerMEMS). Consequently, the term MEMS has been expanded to describe the integration of sensing and actuating mechanisms with electronic components on the same chip for the realization of small, compact and intelligent systems. The advantage of MEMS technology lies in the scaling properties of the different transduction mechanisms (e.g. electrical, magnetic, thermal etc) and structural materials [1] that allow MEMS devices to be faster, more energy-efficient and more sensitive than their macroscopic counterparts. Given the versatility of MEMS technology, the MEMS industry has been experiencing a continuous increase with a variety of commercial products readily available, including pressure sensors, displays, as well as inertial devices and motion sensors for automobiles, portable electronics and game consoles. While significant focus is currently being placed on the commercialization of more MEMS devices, new technologies have to be developed for further miniaturization, automation, and self-sustaining operation of microsystems.

1.1 Motivation

The development of next-generation adaptive, self-sustaining microsystems is directly linked with the development of efficient power sources and energy storage devices at the micro-scale that will enable reliable, long-term operation. Prime examples of such systems include medical implants, smart pills, as well as wireless sensor networks, or “smart-dust” [2]. A conceptual schematic of a smart dust mote is shown in Figure 1a; it contains sensors, electronics for control and data transmission/reception, energy harvesting mechanisms as well as energy storage devices. Dimensions of “smart-dust” are intended to be on the order of a few cubic millimeters so that they can be deployed in large quantities in various environments. As a result, they require power devices to be fabricated with sub-millimeter range footprint. As it is illustrated in Figure 1b, while miniaturization of electronic and MEMS components can be successfully accomplished, still the power levels required have to be met by macro-scale devices. Consequently, the development of energy storage and power devices with high performance for small areal footprints would mark a significant advancement in the microsystem miniaturization.

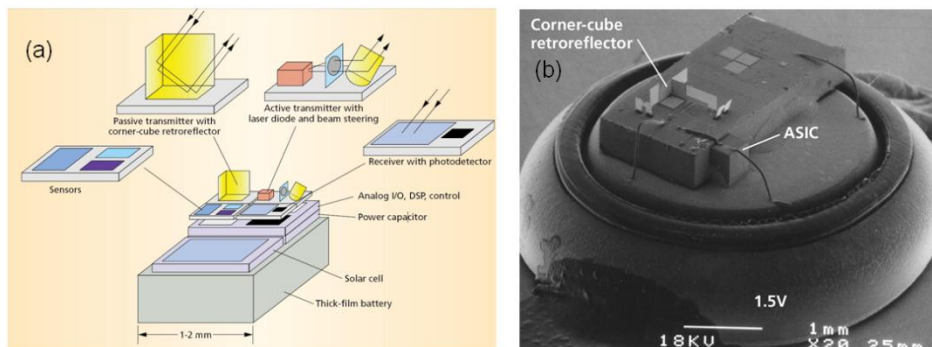


Figure 1.1: a. Conceptual schematic of a smart-dust mote; b. SEM image showing a microsystem [2]

Several investigations have been conducted in order to understand the power requirements for such microsystems and outline a set of criteria that need to be met by the energy storage and power supplies. Long *et al* has reported that for a smart-dust mote with 1 mm^3 volumetric footprint, the power consumption should not exceed $10 \text{ }\mu\text{W}$, resulting in an energy requirement of 1 J for daily operation [3] . Similarly, based on the analysis of a multi-element microsystem for measuring temperature, pressure, relative humidity and vibration, Harb *et al* identified a 5 mW peak power for ms communication pulses and a standby power of again $10 \text{ }\mu\text{W}$ [4]. Thin-film batteries have accomplished energy density on the order of 2 J/mm^3 , as reported in the above citations. However, since thin-film batteries are limited by the thickness of the active material, several cm of active area would be required to meet this requirement, which is prohibiting for miniaturized microsystems. Even when combined with solar cells to form hybrid power supplies as suggested by Harb in [4] and shown in Figure 1.2, the batteries still need to maintain a small footprint; thus, new avenues have to be explored for the development of microbatteries with higher areal energy densities.

| | |
|--|-----|
| Peak power requirement (mW) | 5 |
| Width of peak power pulse (ms) | 10 |
| Standby power requirement (μW) | 10 |
| Duration of standby time (min) | 10 |
| Operation of solar cell (h on per 24 h period) | 12 |
| Reserve storage requirement (h) | 12 |
| Specific energy of battery (J/cm^2) | 2.5 |
| Specific power of battery (mW/cm^2) | 50 |

Figure 1.2: Parameters for the power requirements of a microsystem powered by a hybrid power supply [4]

Two major research pathways have been pursued for the improvement of battery performance at the micro/nano scale. The first one employs MEMS technology and is based on the fabrication of three-dimensional electrode structures. This approach results in increased available surface area and active material loading for the same device footprint [3]. Increased surface area enhances the energy and power density compared to 2D batteries [5]. A characteristic schematic illustrating this benefit is shown in Figure 1.3 [5]. Several electrode designs as well as prototype devices have been proposed in the literature and will be presented in more detail in the following sections.

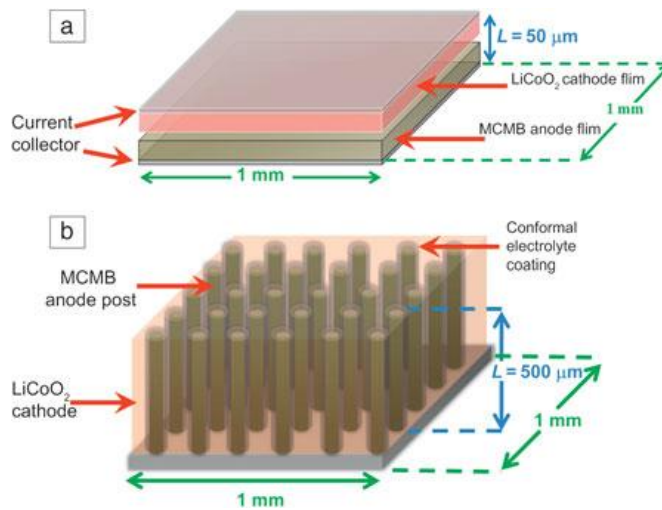


Figure 1.3: Schematic of a (a) 2D parallel plate and a (b) tubular 3D battery showing the dimensions for the typical components [5]

While for these approaches superior energy densities compared to 2D devices have been reported, key challenges still remain. In addition to inherent problems in 3D designs (for example, non-uniform current density distribution [6]), the thickness of the 3D electrode has also been identified as a potential limitation. Since the diffusion path way remains in the micro scale, full lithiation (or generally, redox

reaction) may not be achieved [7]. This can potentially limit microbattery performance at very high current densities.

A second approach has leveraged advances in nanotechnology to enhance battery performance based on the use of nanostructured materials. Indeed, nanomaterials have shown significant potential for improving battery performance due to advantageous properties such as larger electrode/electrolyte contact areas, improved mechanical stability that can accommodate structural changes, as well as shorter distances for electron transport and ion diffusion, as has been documented in several reviews [8], [9]. There are two main critical bottlenecks however in their practical use in micro power sources. The first is related to the total electrode mass that can be assembled in a given area, when nanostructures are used directly on current collectors. This is due to the high porosity and the small dimensions of the nanomaterials. As a result, for a given area, they occupy a smaller volume which in turns limits the available mass. Given that energy density depends on the mass loading (as will be explained in Chapter 2), nanostructured-based approaches are energy density limited. While this problem has been addressed using nanostructures in powder form and electrodes based on ink-casting where the mass can be easily adjusted [5], patterning such architectures in micro/nano geometries is a significant challenge. Based on this discussion, it becomes clear that while each of these general approaches offers notable benefits for the improvement of battery performance, further developments are necessary for next-generation microscale architectures.

1.2 Thesis Contributions

As described in the previous section, micro and nanostructured electrodes present both advantages and shortcomings. 3D microstructures enhance the energy density, but are limited in power density, while nanostructures enable very fast kinetics and rate performance, but are limited in energy density. This Dissertation presents a novel technology that aims to address the aforementioned limitations and combines the benefits of both length scales. This technology is based on the fabrication of hierarchical electrodes that consist of both micro and nano components and can maintain all the benefits of nanostructured materials while yielding higher energy densities due to the surface area enhancement enabled by 3D microfabrication. In addition to standard MEMS techniques, the key enabling tool for this work is the use of the *Tobacco mosaic virus* (TMV) as a nanoscale scaffold for the synthesis of self-assembled, nanostructured energy materials. The TMV is a rod-like plant virus which can be genetically modified to include functional groups with enhanced metal binding properties. As a result, it can be used as a self-assembling template for the device level patterning of nanostructures. The specific contributions of this research are outlined below:

1. Patterned assembly and synthesis of virus-templated nanostructures. As mentioned previously, a key limitation in the practical use of nanostructures in functional devices is their selective assembly and patterning. In this work, leveraging on the self-assembly and robustness of the TMV molecule, a series of fabrication processes have been developed that allow patterning of TMV templates in a variety of

geometries and architectures as well as the synthesis of energy-related nanostructures with desired properties. More specifically, photolithographic patterning of metal-coated TMV as well as uncoated TMV with chemical functionality retention is demonstrated. In addition, these particles can self-assemble onto three-dimensional microstructures fabricated on various substrates, creating new opportunities for the device-level integration. Finally, the metal-coated TMV is used as a scaffold for the deposition of active battery materials in thin-film form using conformal techniques, which results in novel, core/shell nanocomposite electrodes. This toolbox of biofabrication processes constitutes a very facile demonstration of combining bottom-up biological self-assembly with top-down microfabrication processes for the development of device-oriented architectures.

2. Nanocomposite electrodes with improved electrochemical performance.

While metal-coated TMV cannot be used directly in high energy and power density microbattery devices, its robustness and vertical self-assembly allow it to be used as scaffold for the deposition of active battery materials. In this work, the TMV three-dimensional nanonetwork was combined with Atomic Layer Deposition (ALD), a highly uniform and conformal deposition technique with excellent control over thickness, for the synthesis of nanocomposite electrodes with core/shell geometries. Specifically, model systems consisting of Ni/TiO₂ and Ni/V₂O₅ anodes and cathodes respectively were developed. These electrodes showed excellent cyclic stability, an up to eight-fold increase in areal energy density, and improved gravimetric capacity and rate capability compared to electrodes with planar thin films.

3. Hierarchical electrodes with micro and nano components. The developed processes and nanocomposite electrode geometries were combined for the fabrication and electrochemical characterization of hierarchical electrodes that consist of both micro and nanostructures. Specifically, the electrodes are made of electroplated gold micropillars with aspect ratios on the order of 3:1, where the TMV molecules can self-assemble. ALD was then used to deposit the active battery material across the entire micro/nano textured surface. A 3-fold increase in energy density for the hierarchical electrodes compared to nanostructures alone for both the TiO_2 and V_2O_5 materials has been obtained, in excellent agreement with the increase in surface area and added mass offered by the microstructures.

1.3 Literature Review

The following section will review some of the most characteristic prior work in the field of MEMS batteries. For completion purposes, the section will begin with a very brief overview of other MEMS-based competing technologies for small-scale power and energy storage, including supercapacitors, fuel cells, and energy conversion devices. Following this short discussion, the fundamental approaches for 2D, 3D and nanostructured batteries will be presented.

1.3.1 Other approaches for micro-power applications

In addition to batteries, other electrochemical cells have also been considered as potential energy storage and power devices at the microscale. Supercapacitors are based on a principle of operation that is very similar to that involved in batteries.

There are two main mechanisms of operation: the first is based on reversible adsorption of ions upon charging and discharging on high surface area electrodes, creating double layer capacitance across the anode and cathode, respectively. The second mechanism has been coined with the term “pseudocapacitance” and is used to describe reversible surface or near surface redox reactions occurring on transition metal oxide materials. While both batteries and supercapacitors require high surface area electrodes for efficient micro-scale operation, the key difference is that in supercapacitors the reactions do not occur through the bulk of the material but only on the surface; as a result, supercapacitors can be charged and discharged really fast, delivering high power density at the expense of lower energy density. Several examples of supercapacitors for MEMS applications have been reported in literature and are summarized in Figure 1.4. Beidaghi *et al* reported pyrolyzed SU-8 micropillars as high surface area carbon electrodes [10], while a similar approach by Jiang *et al* utilized CVD grown carbon nanotube forests [11]. A monolithic integration of microsupercapacitors was presented by Chmiola *et al*, where carbon films were produced by patterning and etching of carbide derived films [12]. These techniques present the benefits of using high surface area electrodes for supercapacitors; however the main practical limitation is the low energy density which mandates their combination with microbatteries for long-term, reliable operation in microsystems applications.

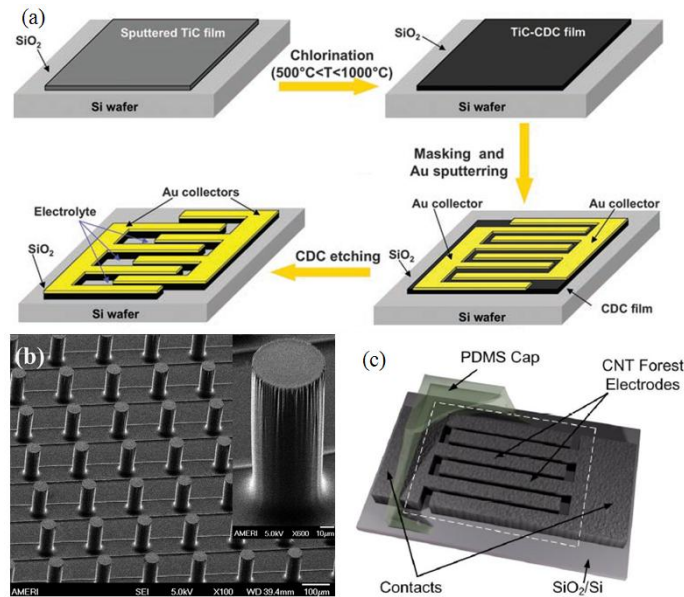


Figure 1.4: (a) Process flow for the fabrication of carbide-derived carbon electrodes [12], (b) SEM of carbonized SU-8 pillars [10], (c) schematic of CNT-forest supercapacitor [11]

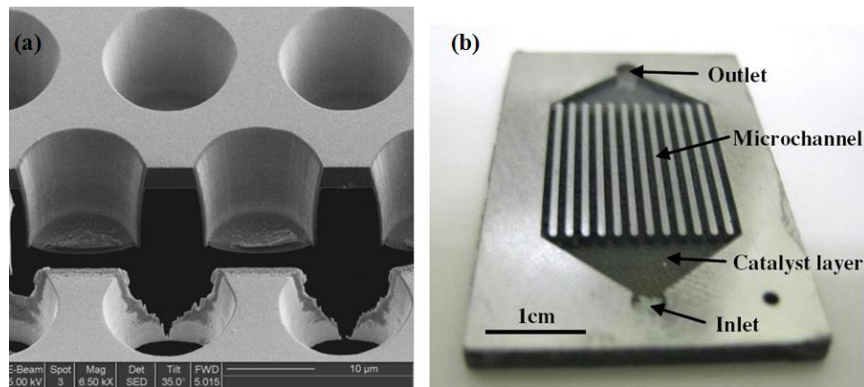


Figure 1.5: (a) High surface catalytic surface for SOFC using etching and ALD deposition [13], (b) optical image of a fuel cell microreactor [14]

A fuel cell is an electrochemical conversion device that constantly uses fuel (hydrogen) and oxidants to produce electricity based on redox reactions at the surface of the electrodes. Fuel cells require the presence of a high surface area catalyst where the conversion of the fuel or oxidant is performed, as well as the existence of an ionic conducting layer that serves a similar role to the one electrolytes have in batteries (ion

conductors, electron insulators). The major benefit of this approach is the constant supply of power for constant supply of fuel, making it very appealing for small scale applications. Polymer exchange membrane (PEM) fuel cells have been reported [15], while other types of cells such as micro-direct methanol fuel cells [16] and solid oxide fuel cells (Figure 1.5a, [13]) have also been studied. In addition to the electrode, catalyst and membrane structure development, research is also being conducted to miniaturize components such as fuel reformers and reactors (Figure 1.5b) for decomposition of fuel to hydrogen [14, 17], which are very important building –blocks for the system-on-a-chip level integration of fuel cells for portable power applications. However, the requirement for on-chip hydrogen storage as well as all the interface components makes fuel cells a less attractive approach compared to batteries for systems that have small areal footprints.

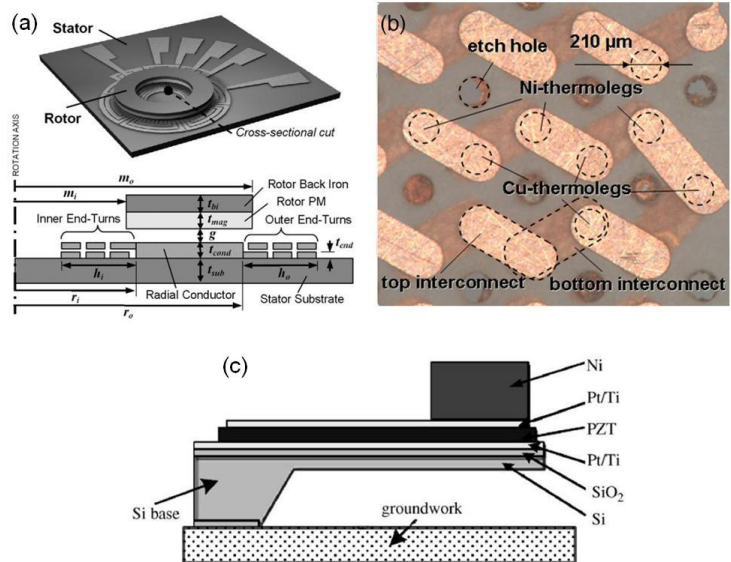


Figure 1.6: (a) Schematic of the electromagnetic generator described in [19], (b) image of the thermoelectric generator structure of [22] and (c) cross-sectional view of a cantilever for piezoelectric energy harvesting [20]

Besides electrochemical cells, several other approaches have been examined for micro-scale energy conversion, most of which are based on four transduction mechanisms: electrostatic, electromagnetic, piezoelectric and thermoelectric. Electret-based generators have been fabricated using micromachining techniques [18], resulting in power generation in the mW range, with the long-term reliability being the major concern. Electromagnetic rotary microgenerators have been successfully developed by Arnold *et al* [19], with a notably higher maximum output power (on the order of W). The major disadvantage in these devices is the extremely complex fabrication process and the auxiliary components required for proper operation, which makes their use prohibitive in small areal footprints. Piezoelectric generators based on harvesting of ambient vibrations using diaphragms and suspended microstructures have been demonstrated and produced power densities comparable to those of lithium ion batteries [20], [21]. A thermoelectric generator with Cu-Ni electroplated thermopiles in an SU-8 mold has been presented by Glatz *et al* [22] and produced power on the order of several hundreds of $\mu\text{W}/\text{cm}^2$. Figure 1.6 shows schematic representations and images of such micromachines.

1.3.2 2D Microbatteries

In the next few sections, some concepts related to battery fundamentals will be used to evaluate the performance of MEMS and nanostructured batteries. The main figures of merit are the energy density or storage capacity given in Wh/g or Ah/g. This is the amount of charge that can be stored in the battery electrodes. Due to the nature of the electrochemical reactions involved in battery operation, this quantity depends on the amount of the active material. However, in micro and nano batteries,

where the footprint of the device is the limiting factor, capacities are normalized per unit area, and will commonly be presented in $\mu\text{Ah}/\text{cm}^2$ throughout the following sections. Detailed explanation of these concepts will be presented in Chapter 2.

Initial work in the field of MEMS fabricated batteries was focused on the development of planar (thin film) electrode designs using traditional micromachining processes. The devices that have been presented in the literature utilize both liquid and solid electrolytes and are both primary (non-rechargeable) and secondary (rechargeable) in nature. Lee *et al* [23] presented a primary battery based on an Au/Zn chemistry which was fabricated in a parallel plate configuration using surface micromachining and adhesive bonding and delivered a maximum energy of $1.38 \text{ mWh}/\text{cm}^2$ at a maximum voltage of 1.5 V (Figure 1.7a). Work from the same group was focused on a different version of this parallel-plate, MEMS fabricated geometry with a Mg/CuCl and Mg/AgCl chemistry that used water as the electrolyte and achieved up to $1.29 \text{ mWh}/\text{cm}^2$ at 1.65 V (Figure 1.7b, [24]). Similarly, Lee also demonstrated bio-fluid activated batteries on flexible substrates. Jimbo and co-workers expanded on the concept of using alternative electrolytes for batteries by developing a gastric fluid micro device based on Pt/Zn electrodes, which was intended for implantable applications [25]. Humble *et al* developed a Ni/Zn microbattery with footprint on the order of 0.02 cm^2 using a side-by-side configuration with electroplated active materials and a basic electrolyte (Figure 1.7c, [26]). The device delivered up to $0.555 \text{ mWh}/\text{cm}^2$ at 1.7 V and was used by Singh *et al* in a proof-of-concept, PCB-level implementation of a hybrid power supply which was consisted of the microbattery and a commercial solar cell array [27]. Driven by a

similar, integrated system application, Albano *et al* presented a planar Ag/Zn microbattery intended for an intraocular pressure sensor (Figure 1.7d, [28]). The device operated at 1.6 V achieved capacities on the order of 83-100 $\mu\text{Ah}/\text{cm}^2$, and was integrated with a microcontroller to investigate potential limitations for a practical application.

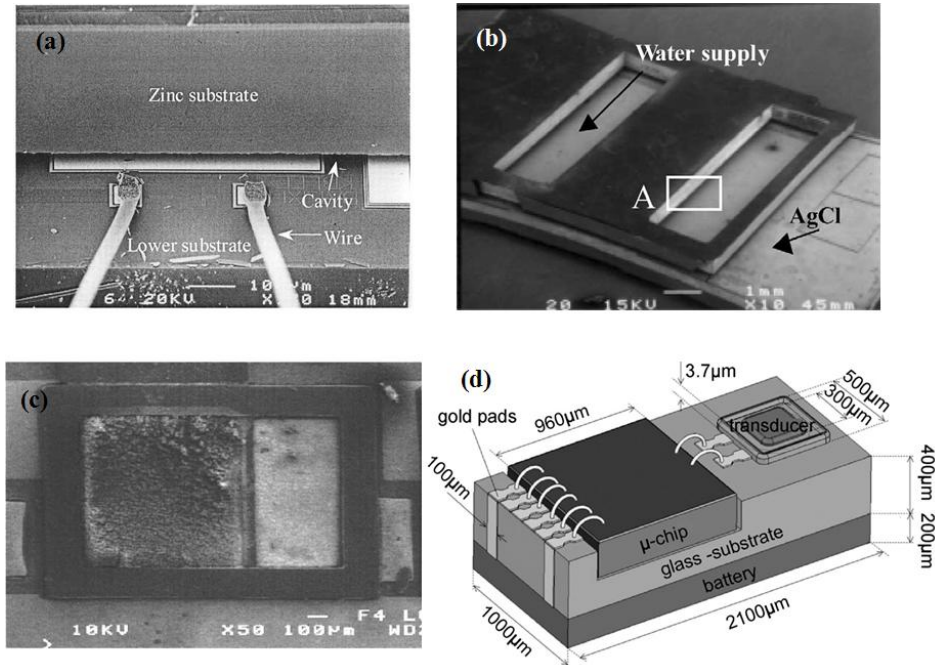


Figure 1.7: (a) SEM image of the primary battery described in [23], (b) SEM image of the Mg/AgCl battery with water as the electrolyte [24], (c) SEM image of the side-by-side Ni/Zn microbattery of [26], and (d) schematic of the integrated intraocular pressure sensor system [28]

In addition to 2D microbatteries with liquid electrolytes, significant work has been done on devices with polymer or solid electrolytes. In general, solid electrolytes suffer from lower ionic conductivity compared to liquids, however they enable simpler fabrication and packaging as well as reliable operation under a wide range of environmental conditions. Seminal work in the field was conducted at the Oak Ridge National Lab, where an all-solid-state microbattery was first developed [29], [30]. It

was fabricated by sputtering of current collectors and blocking electrodes as well as lithium cobalt oxide (LiCoO_2) cathodes and a lithium phosphorous oxynitride (LiPON) electrolyte and delivered a capacity of $\sim 120 \mu\text{Ah}/\text{cm}^2$ (Figure 1.8a). Several other groups developed designs based on this work [31]. For example, Fleutot *et al* presented a similar version of this design with different cathodes and boron-doped LiPON electrolyte, achieving comparable storage capacities [32]. Microbatteries with polymer or gel electrolytes have also been fabricated. Dokko *et al* fabricated an ink-jet printed interdigitated electrode microbattery with sol-gel-based electrodes ($\text{Li}_{4/3}\text{Ti}_{5/3}\text{O}_4$ and LiMn_2O_4) and electrolyte (PMMA sheet with LiClO_4) that achieved a capacity of $4.4 \mu\text{Ah}/\text{cm}^2$ [33] (Figure 1.8b). In a similar approach, Ho *et al* developed a direct-write dispenser printing technique to deposit thick porous films of Zn and MnO_2 sandwiching an ionic liquid-based polymer electrolyte (Figure 1.8c). This primary battery achieved capacities up to $0.98 \text{mAh}/\text{cm}^2$ [34].

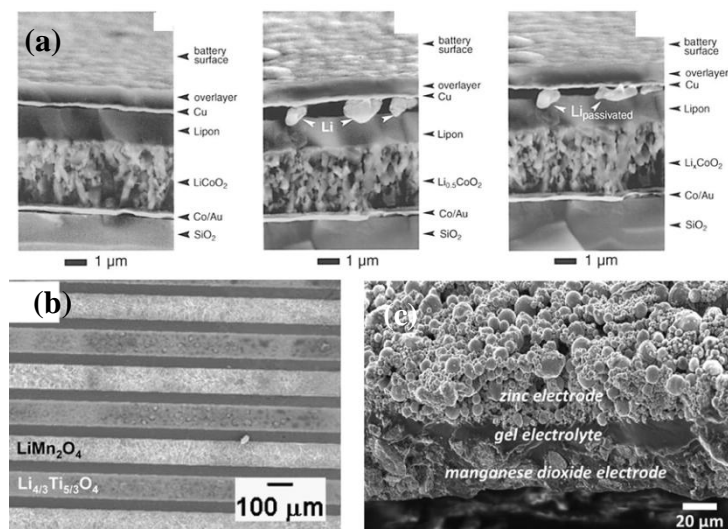


Figure 1.8: 2D Microbatteries with solid and polymer electrolytes; (a) in-situ cell image of the Oak Ridge 2D battery before testing, after first charge, and after first discharge, [30], (b) interdigitated sol-gel microbattery[33], (c) ink-jet printed microbattery[34]

The properties of the most important planar, 2D microbatteries are summarized in Table 1. It can be seen that while some designs are capable of very high capacities, they are non-rechargeable which would limit their practicality in most microsystem-related applications.

TABLE 1: SUMMARY OF 2D MICROBATTERIES

| Group | Chemistry | Cell Type | Capacity ($\mu\text{Ah}/\text{cm}^2$) | Comments |
|-----------------------------|---|-----------------------|---|---|
| Lee <i>et al</i> [23] | Zn-H ₂ O ₂ | Primary – Full Cell | 920 | Parallel Plate - Surface Micromachined |
| Sammoura <i>et al</i> [24] | Mg-AgCl | Primary – Full Cell | 781 | Parallel Plate - Surface Micromachined |
| Humble <i>et al</i> [26] | Ni-Zn | Secondary – Full Cell | 320 | Side by side- Electroplated |
| Albano <i>et al</i> [28] | Ag-Zn | Primary – Full Cell | 83-100 | Sandwiched structure - sputtered |
| Neudecker <i>et al</i> [30] | Li-LiCoO ₂ | Secondary – Full Cell | 120 | Sandwiched structure – sputtered/e-beam |
| Fleutot <i>et al</i> [32] | Li-TiOS | Secondary – Full Cell | 90 | Sandwiched structure – sputtered/e-beam |
| Dokko <i>et al</i> [33] | Li ₄ Ti ₅ O ₄ - LiMn ₂ O ₄ | Secondary – Full Cell | 4.4 | Sol – gel – ink jet printed |
| Ho <i>et al</i> [34] | Zn-MgO ₂ | Primary – Full Cell | 980 | Direct write - ink jet printed – sandwiched |

1.3.3 3D Microbatteries

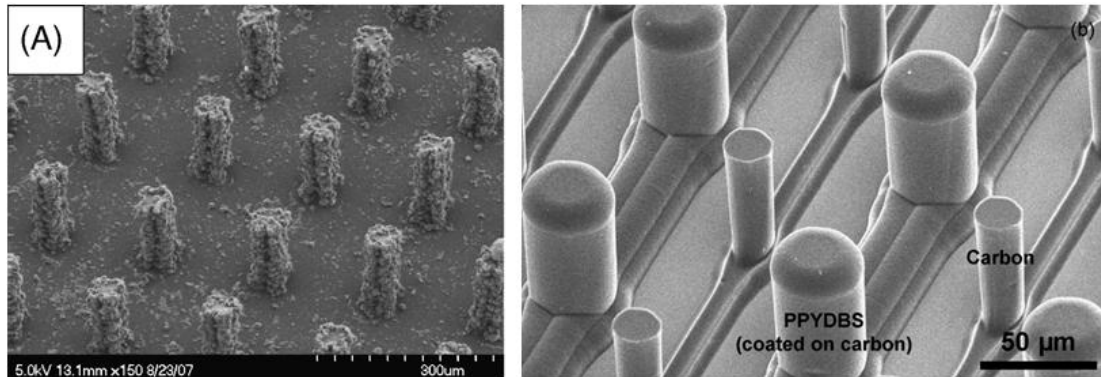


Figure 1.9: C-MEMS carbon electrodes for 3-D microbatteries; (a) meso-carbon micro-beads on carbonized SU-8 posts [7], (b) SEM image showing full cell carbon-polypyrrole microbattery [35]

The characteristic SEM images in Figure 1.8 outline the significant challenge with 2D microbatteries, as the thickness of the electrodes cannot be arbitrarily increased while maintaining high conductivities and rate capabilities. Three-dimensional architectures promise to improve upon this issue by increasing surface area and material mass loading in the out-of-plane dimension. The merits as well as the limitations of this approach have been analyzed in several reviews [6], [3] and have been mentioned in the previous section. Several electrode geometries as well as prototype devices have since been presented in literature. In early work, 3D carbon electrodes made by pyrolysis of SU-8 microposts have been developed by Madou's group in UC Irvine with a process named "C-MEMS" (carbon MEMS) that are shown in Figure 1.9. Individual anode electrodes demonstrated capacities up to $125 \mu\text{Ah}/\text{cm}^2$, notably higher compared to 2D films [36]. The performance of these electrodes was improved by means of meso-carbon micro-beads that were deposited on the carbon structures and further increased the reactive surface area [7]. Using the C-MEMS microposts as the building block structure, a full microbattery prototype

was developed using electrochemical deposition of polypyrrole on alternating arrays of electrodes. The capacity of this device was limited to just $10.6 \mu\text{Ah}/\text{cm}^2$, primarily due to the mismatching between the electrode masses [35].

Significant work in the field of 3D microbatteries was performed at Kim's group in UCLA. The basis of this technology is the development of high aspect ratio silicon molds using dry and vapor etching and subsequent filling of the molds with electroplating and pressure infiltration. Chamran *et al* utilized this method to separately demonstrate carbon anodes and V_2O_5 cathodes using filling of the molds with a paste of the material [37]; the paste was synthesized in a way similar to conventional, commercial battery electrodes. After application of a back-side Ag paste current collector and dissolution of the molds, free-standing electrodes were produced (Figure 1.10a). These half-cell configurations showed capacities of $4.5 \text{mAh}/\text{cm}^2$ and $1.15 \text{mAh}/\text{cm}^2$, respectively. These values mark a significant improvement compared to prior work, however the technology is not highly suitable for batch manufacturing. In the same paper, a full-cell Ni-Zn microbattery was developed in the silicon mold using alternating electrodeposition of Ni and Zn electrodes. These prototypes exhibited capacities up to $2.5 \mu\text{Ah}/\text{cm}^2$, due to dissolution of the Zn electrode in the alkaline electrolyte. In a later demonstration, a primary Zn-air microbattery was developed based on the same approach, achieving a remarkable capacity of $8.93 \text{mAh}/\text{cm}^2$ (Figure 1.10b[38]). A microbattery using the Zn-air chemistry was fabricated by Armutlulu et al with multilayer electroplating and sacrificial etching to form porous zinc structures [39]. The capacity was on the order $2.5 \text{mAh}/\text{cm}^2$. While the energy density of these two devices is adequate to meet

microsystem requirements, the primary nature of the chemistry is not ideal for applications requiring long-term uninterrupted operation.

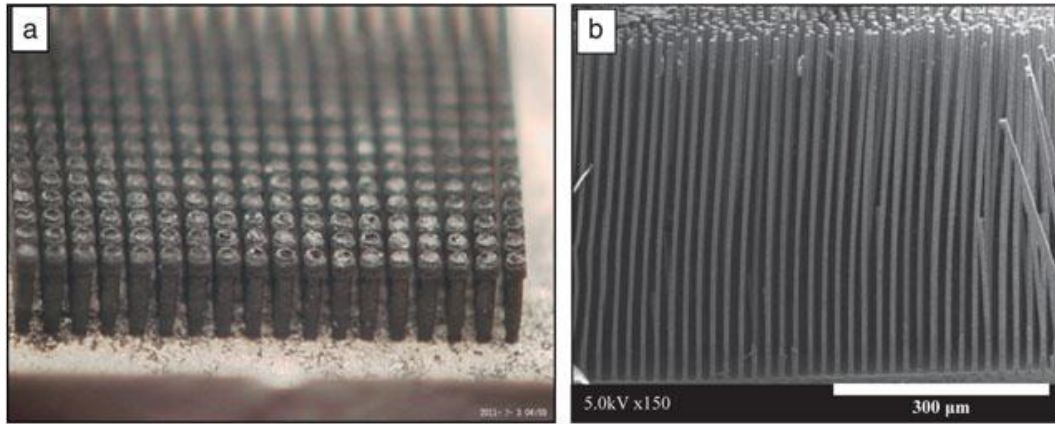


Figure 1.10: (a) image of meso-carbon micro-bead paste electrodes formed into pillars inside a silicon mold, (b) electroplated zinc microposts for a zinc-air microbattery [5]

As in the case of 2D microbatteries, work has also been directed towards the development of devices with solid or polymer electrolytes. A very high energy density device was developed by Nathan *et al* and Golodnitsky *et al*, who used perforated glass substrates (Figure 1.11a-b) as a template for the deposition of current collectors, active materials and a gel electrolyte using vacuum filtration, chemical/electrochemical deposition and spin-casting [40], [41]. The highest reported capacity in these investigations was 2 mAh/cm². Kotobuki *et al* used a honeycomb ceramic electrolyte 3D structure and deposited the anode and cathode on both sides using sol-gel processing (Figure 1.11c), achieving capacities on the order of 8 μAh/cm² [42]. Recently, a concept for an all-solid-state microbattery has been proposed that is based on conformal deposition of thin films on high aspect ratio silicon pores [43, 44]. Initial work was focused on identifying the appropriate candidate materials [45], while the first demonstration of such a 3D architecture was focused on a silicon anode only (Figure 1.11d), which showed a capacity of 255

$\mu\text{Ah}/\text{cm}^2$ [46]. While the integration capabilities of this approach in microsystems are more direct than the previously described work, the technology is limited in terms of the energy density by the thickness of the active materials; in addition, the lack of a suitable Li-containing cathode and electrolyte prevent the development of a full cell. Table 2 summarizes the characteristics and performance metrics of the state-of-the-art 3D microbatteries.

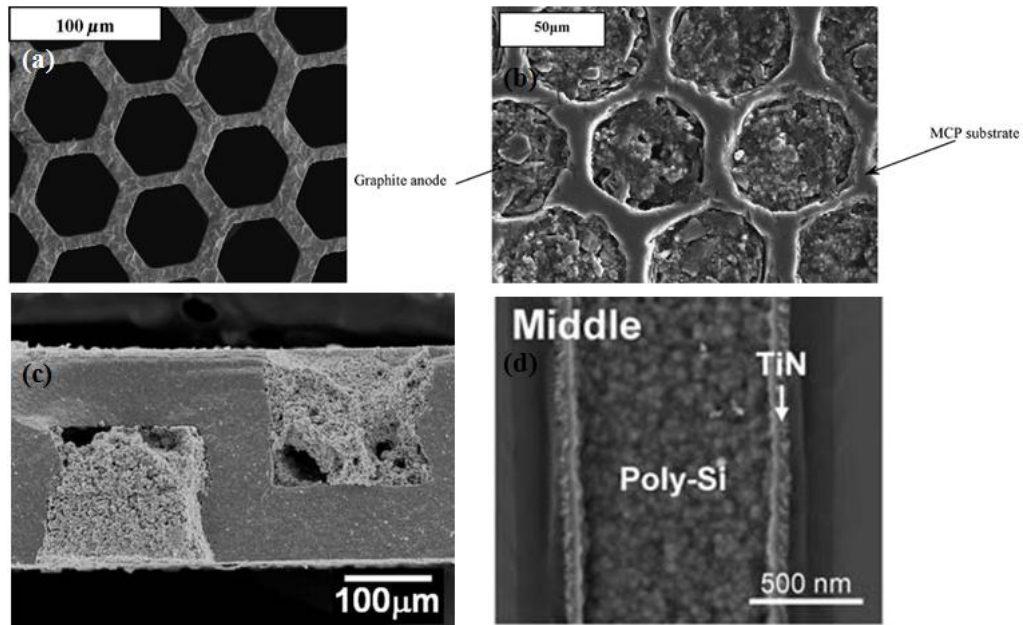


Figure 1.11: (a) SEM image showing a perforated glass substrate mold [40], (b) SEM image showing the mold of (a) filled with the active materials, (c) SEM image showing LiCoO_2 (left) and $\text{Li}_4\text{Mn}_5\text{O}_{12}$ (right) sols inside a ceramic electrolyte [42], (d) cross section SEM image inside a silicon pore showing the current collector (TiN) and anode material (poly-Si) [46]

TABLE 2: SUMMARY OF 3D MICROBATTERIES

| Group | Chemistry | Cell Type | Capacity ($\mu\text{Ah}/\text{cm}^2$) | Comments |
|-----------------------------|-----------------------------|----------------------|---|---|
| Wang <i>et al</i> [36] | Carbon | Secondary– Anode | 125 | Carbonized SU-8 microposts |
| Teixidor <i>et al</i> [7] | Carbon | Secondary– Anode | 350 | Carbonized SU-8 microposts with MCMB |
| Min <i>et al</i> [35] | Carbon - PPy | Secondary– Full Cell | 10.6 | Carbonized SU-8 microposts/plated PPy |
| Chamran <i>et al</i> [37] | Carbon | Secondary– Anode | 4500 | MCMB paste inside silicon mold |
| Chamran <i>et al</i> [37] | V_2O_5 | Secondary– Cathode | 1150 | V_2O_5 nanoroll paste inside silicon mold |
| Chamran <i>et al</i> [37] | Ni-Zn | Secondary– Full Cell | 2.5 | Electroplated Ni and Zn posts in a silicon mold |
| Chamran <i>et al</i> [38] | Zn-air | Primary– Full Cell | 8900 | Electroplated Zn posts in a silicon mold |
| Armutlulu <i>et al</i> [39] | Zn-air | Primary– Full Cell | 2500 | Electroplated layers of Zn on top of sacrificial Cu/Ni |
| Nathan <i>et al</i> [40] | Graphite– MoS_4 | Secondary– Full Cell | 2000 | Impregnated materials in perforated glass |
| Kotobuki <i>et al</i> [42] | Ni-Zn | Secondary– Full Cell | 7.6 | Sol-gel filling inside a ceramic honeycomb |
| Baggetto <i>et al</i> [46] | Silicon | Secondary– Anode | 255 | Thin film deposition inside high aspect ratio silicon |

1.3.4 Nanostructured Micro/nano Batteries

The continued advances in nanomaterials synthesis methodologies combined with the advantages they offer for electrochemical energy storage applications has generated significant interest in potential paradigm shifting technologies for next-generation small scale power and energy devices. The majority of published work in the literature is focused on nanomaterials replacing micro-sized particles in conventional ink-casted, slurry-based electrodes. Generally, integrating these electrodes in microbatteries is very complex, as discussed in the previous section with the work presented by Chamran *et al* on filling silicon molds with composite pastes [37]. As a result, the overview presented in this Dissertation will be limited to

processes where nanostructures are grown or deposited directly on current collectors, since this route holds more promise for use in microbattery applications.

A very facile method to form nanorods, nanotubes, and nanowires on current collectors is based on the use of high aspect ratio nanotemplates. Similar to the silicon molds discussed previously, these templates form nano-sized pores which can be filled with the active material. The most commonly used templates in literature have been Anodic Aluminum Oxide (AAO) and poly carbonate (PC) membranes, which are fabricated through controlled oxidization of high purity aluminum (resulting in high ordered pores) and radiation-track etching of polycarbonate sheets (resulting in randomly distributed pores). Martin's group at the University of Florida has pioneered the use of this approach for nanostructured synthesis. Work from their team presented the fabrication of SnO₂ nanorod anodes with a capacity of 37 $\mu\text{Ah}/\text{cm}^2$ and excellent rate capability up to very high current densities [47]. Zhang *et al* used AAO templates to demonstrate a micro/nano battery formed in the pores, where graphite micro particles were deposited on one side of the membrane while the other was filled with a mixture of CNTs and V₂O₅ [48]. These devices achieved capacities up to 80 $\mu\text{Ah}/\text{cm}^2$. Core/shell nanorods have also been demonstrated using the AAO templating approach. Cheah *et al* electrodeposited Al nanorods inside AAO pores to form a 3D current collector, followed by deposition of TiO₂ as an active anode material with ALD. The maximum capacity achieved in these half-cells was on the order of 10 $\mu\text{Ah}/\text{cm}^2$ [49]. Using a very similar technique, nanorod-shaped cathodes were also presented by Shaijumon *et al* [50]. In this work, electroplated Al nanorods served again as current collectors, while sol-gel deposition of LiCoO₂ was employed

to create a uniform coating of the active material, resulting in electrodes with a capacity of $110 \mu\text{Ah}/\text{cm}^2$.

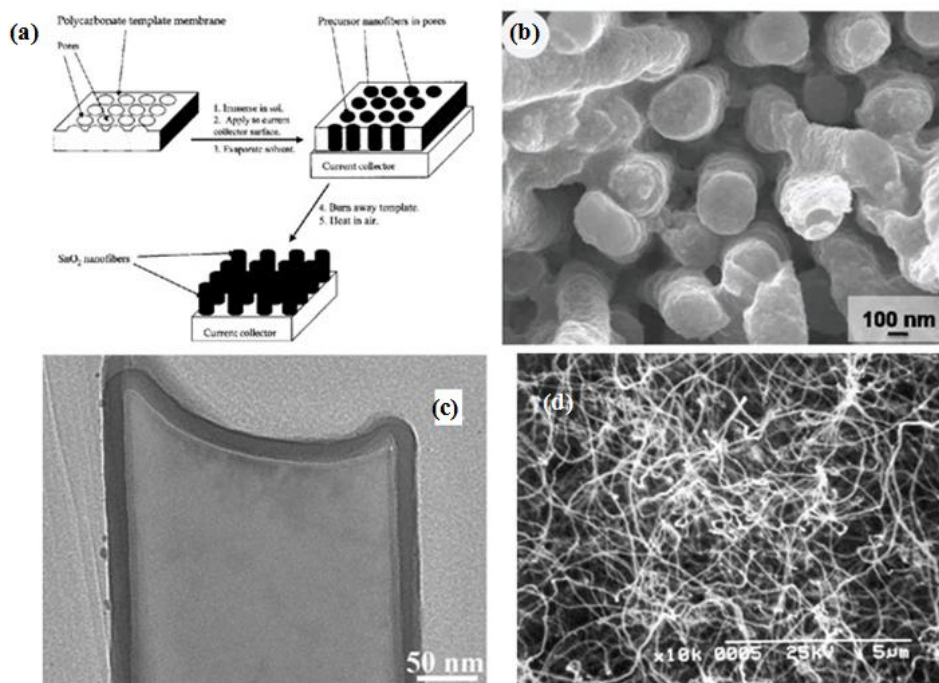


Figure 1.12: (a) Concept of nanorod fabrication in PC membrane template as presented in [47], (b) SEM image of Al/LiCoO₂ nanorods [50], (c) TEM image of Al/TiO₂ nanorods [51], (d) CNTs grown on AAO templates [48]

The major disadvantage of this templated synthesis method is that there exists a limit in the amount of active material that can be deposited within a template, which limits the energy density that can be obtained. Template-free methods can be a potential solution to this problem. Ortiz *et al* presented TiO₂ anodes based on anodization of Ti metal both directly on the foil as well as on films grown on Si substrates [52, 53]. They developed very high aspect ratio titania nanotubes, capable of achieving capacities up to $\sim 90 \mu\text{Ah}/\text{cm}^2$, which marks an almost 9-fold increase compared to the templated-based techniques. Cui's group at Stanford has also done considerable research in current collector-grown nanostructures, with the emphasis on

silicon anodes. In their work, crystalline silicon nanowires are grown using the VLS method on stainless steel substrates [54]. When combined with CVD deposition of amorphous silicon, a core/shell nanoarchitecture with a mass loading on the order of $200 \mu\text{g}/\text{cm}^2$ and higher mechanical stability can be created [55]. In order to increase the available surface area for active material deposition, they have also used carbon nanofibers to form a highly porous scaffold for silicon deposition. The nanofibers were drop-casted on the steel disc and silicon was deposited with CVD, resulting in electrodes with a very high loading of $2 \text{ mg}/\text{cm}^2$ and areal capacities of $4 \text{ mAh}/\text{cm}^2$ [56]. A similar approach was adopted by Lee et al who deposited Sn using electrochemical reduction on commercially purchased CNT nanonetworks (loading on the order of $4 \text{ mg}/\text{cm}^2$). CNT forests have also been grown directly on metallic electrodes and served as a highly textured surface for Si deposition with loadings up to $1 \text{ mg}/\text{cm}^2$ [57].

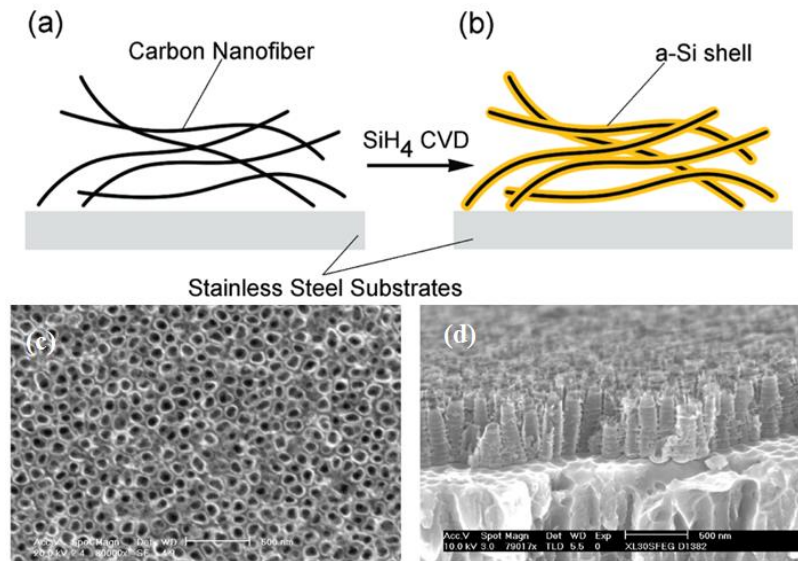


Figure 1.13: Schematic demonstration of a composite anode showing carbon nanofiber (a) and Si deposition (b) on a stainless steel substrate [56], (c) top-view and (d) cross-section SEM images of titania nanotubes [53]

Even though these methods are capable of growing very high aspect ratio nanostructures directly on current collectors with large amounts of active materials, the integration with standard microfabrication still remains challenging. For example, drop casting methods of nanofibers require selective patterning on a MEMS device, while CNT growth is highly dependent on the catalyst and substrate used. Table 3 summarizes the properties of nanostructured batteries with electrodes formed directly on current collectors.

TABLE 3: SUMMARY OF NANOSTRUCTURED MICROBATTERIES

| Group | Chemistry | Cell Type | Capacity ($\mu\text{Ah}/\text{cm}^2$) | Comments |
|-----------------------------|----------------------------|----------------------|---|--|
| Li <i>et al</i> [47] | SnO_2 | Secondary– Anode | 37 | Sol-gel deposition in PC membrane |
| Shaijumon <i>et al</i> [50] | LiCoO_2 | Secondary– Cathode | 110 | Electroplating of Al and sol-gel of LiCoO_2 in AAO |
| Ortiz <i>et al</i> [52] | TiO_2 | Secondary– Anode | 43 | Anodization of Ti foil |
| Ortiz <i>et al</i> [53] | TiO_2 | Secondary– Anode | 56 | Anodization of Ti film deposited on Si wafer |
| Zhang <i>et al</i> [48] | $\text{CNT-V}_2\text{O}_5$ | Secondary– Full Cell | 80 | Growth of CNTs on AAO and sol deposition of V_2O_5 |
| Cui <i>et al</i> [55] | Si | Secondary– Anode | 4000 | CVD of Si on carbon nanofiber network |
| Cheah <i>et al</i> [51] | TiO_2 | Secondary– Anode | 11 | Electroplating of Al and ALD of TiO_2 in AAO |

1.4 Thesis Objective and Structure

The objective of this research is the development of a novel, paradigm-shifting technology for the fabrication of microbattery electrodes that combines the advantages of both the MEMS – based and nanotechnology – enabled approaches. Figure 1.14 shows a high level description of this objective. Virus-templated nanostructures and three-dimensional MEMS fabricated microstructures are the two building block technologies that are integrated to create hierarchical electrodes (with both micro and nano components). The nanostructured nature of the active materials results in high rate performance electrodes while the microstructures can controllably increase the available energy density of the electrodes, addressing this key limitation involved in nanostructured microbatteries.

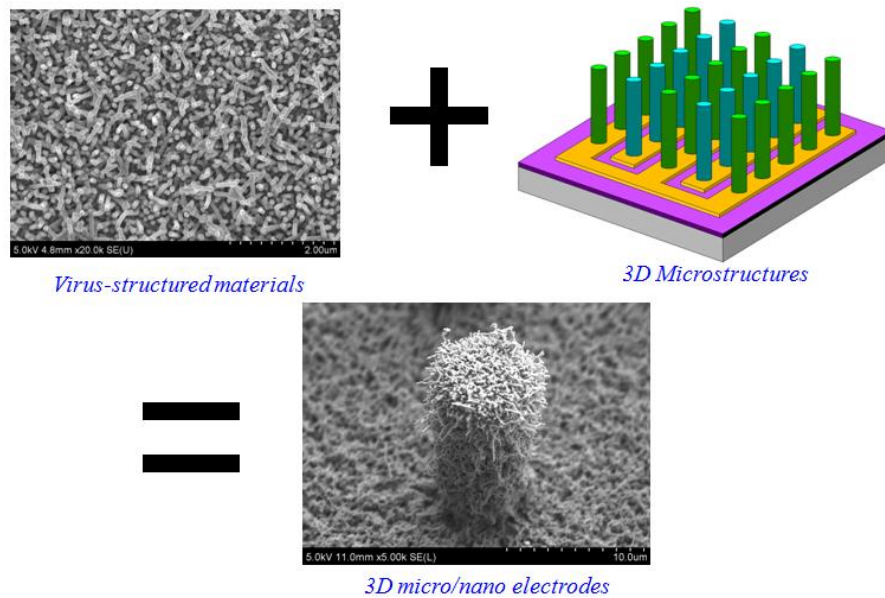


Figure 1.14: Conceptual high - level approach describing the dissertation objective

The dissertation is divided in 6 chapters. Chapter 1 introduced the general motivation and objective of this work and covered the prior art in the field of microbatteries. Chapter 2 presents some background information on processes and

concepts related to this work. Specifically, fundamentals of battery operation, key fabrication processes, biotemplating approaches with an emphasis on the TMV as well as previous work by our group and others in this area will be covered. Chapter 3 describes the biofabrication processes that have been developed for the patterned assembly of the TMV in defined architectures as well as its use for the synthesis of novel nanostructures. Chapter 4 is focused on the electrochemical characterization of nanocomposite core/shell electrodes synthesized on the TMV template with an emphasis on Ni/TiO₂ and Ni/V₂O₅ anodes and cathodes respectively. Chapter 5 is dedicated to the design, fabrication and characterization of the hierarchical electrodes that consist of gold micropillars and the nanocomposites developed in Chapter 4. Finally, Chapter 6 contains a summary of this work as well as an outlook on the future designs and challenges.

Chapter 2 : Review of Related Concepts and Processes

In this chapter, a review of fundamental concepts and processes upon which this work has been based will be presented. Particularly, the fundamentals of battery operation will be discussed initially; then, the focus will be shifting on biotemplating, the process used to synthesize materials using biological scaffolds. Some general discussion on previous work with various particles will be followed by a detailed review on the use of the TMV as a template, its applications, as well as the benefits it presents in MEMS device applications.

2.1 Fundamentals of Battery Operation

The electrochemical cell is the building block component of batteries which are in practice comprised of arrays of such cells in series or in parallel. An electrochemical cell is a device that converts the chemical energy stored in its active materials to electricity by means of oxidation and reduction reactions (redox reactions). An oxidation reaction involves the release of electrons by an atom, molecule or ion while a reduction reaction described the gain of electrons. This type of cell consists of three components:

- 1) *The anode or negative electrode.* This is the electrode that is oxidized during discharge operation and releases electrons to an external circuit.
- 2) *The cathode or positive electrode,* which accepts these electrons allowing reduction to occur.
- 3) *The electrolyte,* which is the medium for transfer of electrons in the form of ions within the cell from the anode to the cathode. It can be a liquid such as a

metal salt or acid; however, as discussed in the previous chapter, batteries with solid or polymer electrolytes have also been devised.

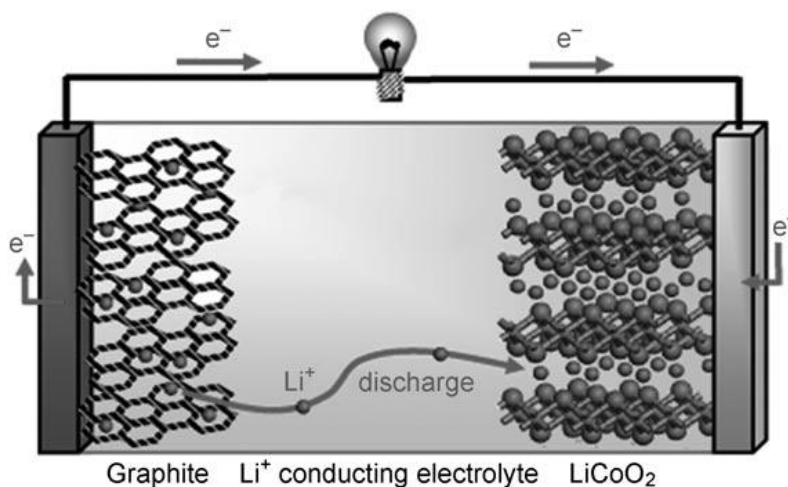


Figure 2.1: Schematic showing operation of a commercial Li-ion battery [9]

Figure 2.1 demonstrates the operation of a Li-ion battery under discharge. Li-ion batteries have become the prominent power source for commercial electronics due to their light weight and high energy density. A commercial Li-ion cell most commonly consists of a graphite anode and a LiCoO₂ cathode (although other Li-containing compounds have been explored). During charge, Li ions are extracted from the LiCoO₂ structure and inserted in between the layers of the graphite, a process that is called intercalation and is used to describe insertion of ions in a crystal structure. During discharge, as indicated previously, oxidation occurs at the anode, resulting in electrons flowing through the external circuit along with the de-intercalation (extraction) of the Li-ions; the ions flow through the Li-conducting electrolyte and are intercalated back to the LiCoO₂.

The theoretical voltage of a battery is controlled by the standard electrode potentials of the active materials. The standard electrode potential is a measure of the reactivity of the material and it corresponds to the electrical potential measured at

standard conditions, where all solutions are at concentrations of 1mol/kg and gases are at a pressure of 1 bar. While the electrical potential between two electrodes can be measured effectively, accurate measurement of one electrode potential is not an easy task. On that note, the electrode potentials are measured with regards to a reference electrode. This is the Standard Hydrogen Electrode (SHE) whose potential has been set upon convention to be 0.0 V. Since for a redox reaction the oxidation potential is the negative of the reduction potential, it is sufficient to measure one of these two voltages. In the case of the standard electrode potential, the reduction potential is the one commonly used. For a Li-ion battery system, these potentials are expressed with respect to the Li/Li^+ redox pair, which in turn is measured according to the same technique.

Based on these definitions, the theoretical voltage of an electrochemical cell is taken as the sum of the anode and cathode potentials, where the oxidation potential is the negative of the reduction value. In the case of a Li-ion battery specifically, if the reduction potentials vs Li/Li^+ for the anode and cathode, respectively, are known, the battery voltage is:

$$E_{cell} = E_{cathode} - E_{anode} \quad (1)$$

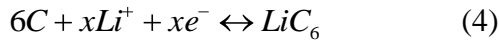
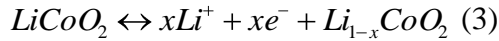
For example, for the commercial Li-ion battery of figure 2.1, the LiCoO_2 oxidation potential vs Li/Li^+ is on average around 3.7 V [50], while the intercalation potential for graphite is between 0.2 V and 0.1 V [36]. Based on equation (1), this gives a nominal voltage on the order of 3.6 V, typical of commercial cells.

The capacity of a battery, as defined by Linden, is the total quantity of electricity involved in the electrochemical reaction. It corresponds to the amount of charge

released from the active materials during the discharge operation (in the case of Li-ion batteries, Li ion intercalation) and it is expressed in Coulombs, or more commonly in Ampere-hours. Theoretically, 1 gram-equivalent weight of material will deliver 96,587 C or 26.8 Ah (per mol). This quantity is represented by F and is called “one Faraday”. The 1 gram-equivalent weight is the molecular weight divided by the number of moles of electrons involved in the reactions. The capacity can be therefore calculated using the equation:

$$Capacity = \frac{xF}{M_{electrode}} \quad (2)$$

where x is the number of moles electrons released in the reaction, F is Faraday’s number, and $M_{electrode}$ is the molecular weight of the electrode. For example, for the C-LiCoO₂ that has been examined in this section, the half reactions are given below:



In reaction (3), the maximum value for the x coefficient is 0.5 to avoid collapse of the structure. In reaction (4), x can be up to 1[58]. Taking into account the molecular weight of the reactants, the capacities for the cathode and anode are 137 mAh/g and 372 mAh/g, respectively.

It is interesting to see the relationship between the energy storage capacity and the energy density of a battery. The energy density, in Wh/kg most commonly, is estimated by multiplying equations (1) and (2). Consequently, the energy density can be increased if the capacity and/or the operating voltage are increased. The gravimetric rating is typically a characteristic of the material and not a performance

metric; it is used to evaluate how close the capacity of an electrode is to actual capacity of a material system. In a practical battery application, the amount of material in grams is what determines the energy density. More specifically in MEMS devices, since the limiting factor is the areal footprint of a device, energy density is normalized per square footprint rather than the gravimetrically.

2.2 Biotemplating Processes

There is a wide variety of methodologies that have been employed for the synthesis of nanostructured materials such as nanotubes and nanowires, nanoparticles and quantum dots. Some of the most common processes used for the bulk fabrication of zero and one-dimensional nanomaterials involve vapor-liquid-solid reactions through the combination of catalytic particles on a substrate and chemical vapor deposition or epitaxial methods. Other less expensive techniques such as hydrothermal synthesis, thermal evaporation, sol-gel processes and electrodeposition have also been used widely in the literature. In addition to bulk synthesis, creation of hierarchical structures has been achieved through the use of porous templates as described in the previous chapter. While all of these techniques demonstrate the significant progress in the field, they often have to balance the trade-off between good control over structural properties, variability of available materials, and aspect ratios on one hand and low cost, external equipment and process compatibility with remaining fabrication steps (e.g. substrates and temperature) on the other.

Biotemplating refers to synthetic routes that utilize biological building blocks to guide the assembly of inorganic materials. Some of the characteristic attributes of this approach compared to traditional methods include the structural versatility of

biological molecules, their self-assembly properties, the existence of various functional groups that catalyze particle growth and the ability to tune their structure through genetic modifications, all combined with the low cost involved in the manufacturing process [59, 60].

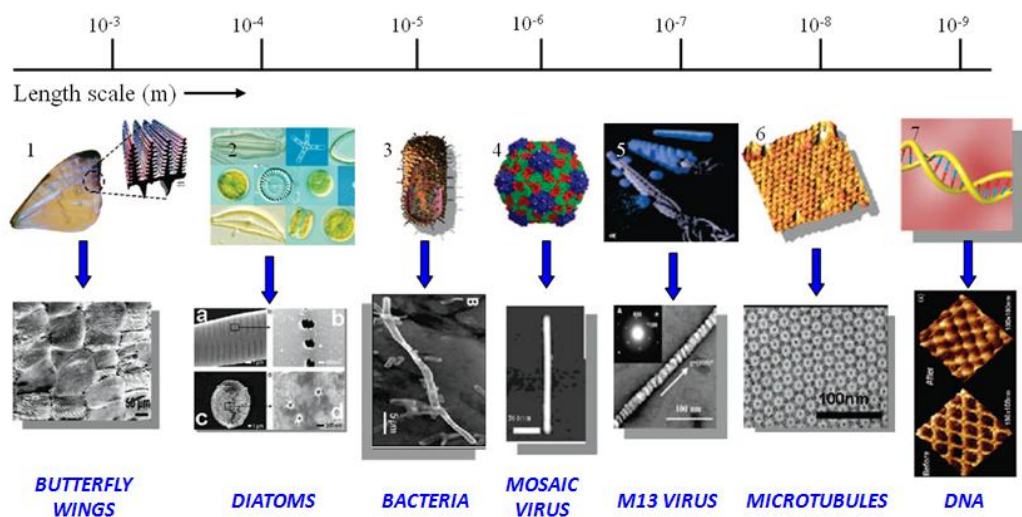


Figure 2.2: Schematic showing the different length scales, shapes, and particles involved in biotemplating processes [61]

Figure 2.2 is a characteristic diagram that illustrates the various length scales and shapes in which biological molecules can be used as templates. For example, the unique light shimmering properties of butterfly wings have been replicated by Huang *et al* to produce photonic devices [62] while diatoms have been used for the formation of metallic micro shells [63]. DNA has been one of the most investigated templates due its controllable length and aspect ratio as well as its phosphate backbone and aromatic bases which create sites for nucleation through electroless plating reactions [64]. Several kinds of metal and polymer nanowires based on DNA strands have been produced [65-69] while more sophisticated approaches for selective mineralization of parts of the chain demonstrate the feasibility of using such particles for molecular-

type lithography [70](Figure 2.3a). Other biological molecules including peptides [71], bacteria [72-74] and proteins [75] have also been used to fabricate fibers, nanoparticles and quantum dots. These synthetic pathways show diversity and great promise to replace semiconductor approaches for nanoscale devices; however, they often tend to suffer from the lack of coating uniformity, reproducibility and the need for special surface treatment prior to metallization and assembly.

Another category of biological nanostructures that offers unique opportunities for biotemplated fabrication are plant and bacteria virus particles consisting of macromolecular assemblies of nucleic acid packaged by many copies of coat proteins. In addition to their surface-exposed functional groups, self-assembly and tunability, these molecules display some unique advantages as they show exceptional stability in a wide range of temperatures and pH values; they can even withstand treatment in organic solvent-water mixtures [76]. Representative examples of biotemplated viral engineering have been achieved with the M-13 bacteriophage virus (Figure 2.3b) which has been genetically modified through phage-display techniques to include specific peptides for inorganic material binding and nanoparticle fabrication [77-79].

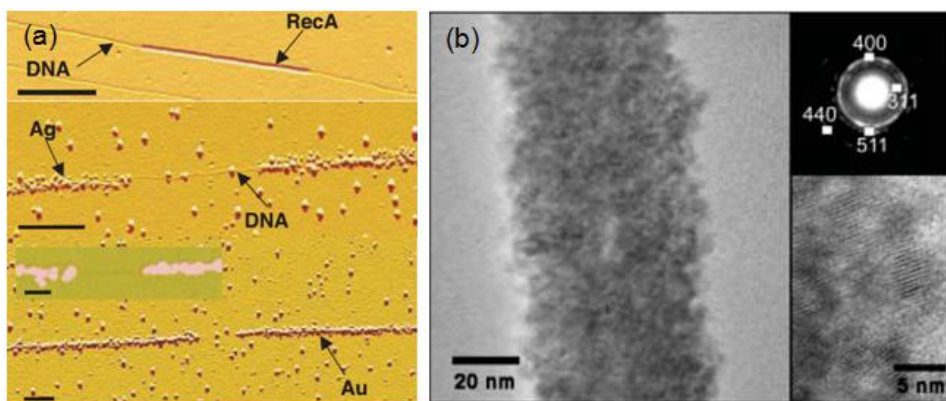


Figure 2.3: (a) AFM image of selective DNA metallization through the use of the blocking RecA protein [80], (b) Co_3O_4 nanowire formed on the M13 bacteria virus [81]

2.3 The Tobacco mosaic virus

2.3.1 General Background

The TMV is a plant virus with worldwide distribution that has been studied since the end of the 19th century and has been found to infect approximately 200 plant species, including tobacco, tomato, and other crop plants[82]. It is one of the simplest and readily available viruses, and this attributes have been used in the understanding of several other virus systems. The TMV is a high aspect ratio cylindrical nanostructure, measuring 300 nm in length with an outer diameter of 18 nm and an inner diameter of 4 nm. Each TMV structure consists of approximately 2,130 coat protein subunits wrapped around a single-stranded positive-sense RNA in a helical structure. A positive-sense RNA can act as a viral messenger RNA that can be directly translated by the host cell. Figure 2.4a shows a TEM image of wild-type viruses while Figure 2.4b is a simplified model of the TMV structure.

The viral structure has been described clearly in [83]. The self-assembly of the virus results from finely balanced, orthogonal weak interactions between the protein molecules and the RNA. These interactions occur along the lateral as well as the longitudinal directions of the helix. The self-assembly proceeds in two stages: nucleation and elongation. During the nucleation stage, the protein molecules assemble by hydrogen bonds and electrostatic and hydrophobic interactions into small disks (nuclei). During the elongation stage, these disks bind electrostatically, one at a time, to a hairpin loop in the RNA strand and they finally anneal into a single helical aggregate.

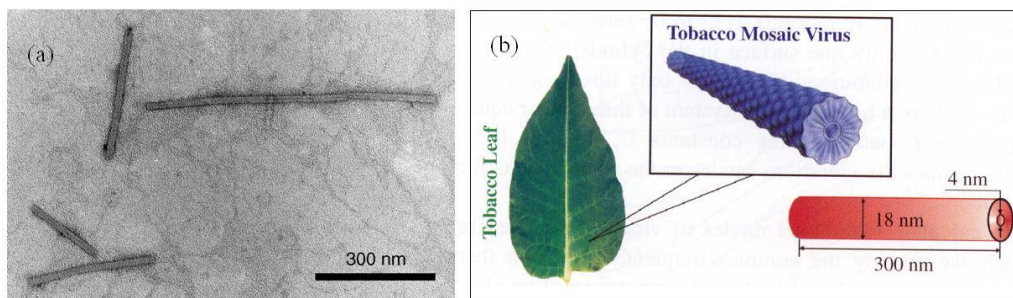


Figure 2.4: : (a) TEM images of wild type viruses, (b) simplified schematic of the TMV structure [84]

Wild-type TMV virions contain numerous electrostatic interactions demonstrated through repeatedly exposed amino acids around their surface, which include arginine, lysine, aspartic and glutamic acids [85]. Amino acids can be hydrophobic or hydrophilic, polar or unpolar, or charged. Figure 2.5 shows a model of the amino acids around the TMV disk (*vulgare* strain) [86]. Hydrophilic amino acids are colored white, water molecules are colored blue, polar hydrophilic amino acids have a green color and the charged hydrophilic ones are red. These properties can influence the chemical behavior of the molecule. In the case of TMV, the accessible outer molecular surface of the virus is dominated by hydrophilic amino acids, of which a large part is charged. Hydrophobic amino acids can also be accessed; however, they are predominantly buried in a hydrophilic environment. These interactions have been previously used to coat wild-type viruses with various materials, such as oxides, sulfides and metal particles [87-89]. In addition to these well-defined assembly features, the TMV can be genetically programmable and renewable in large quantities. The virus is also a robust biological platform, showing stability for pH values from 2-10 for several hours and temperatures up to 60°C without destruction of its integral shape.

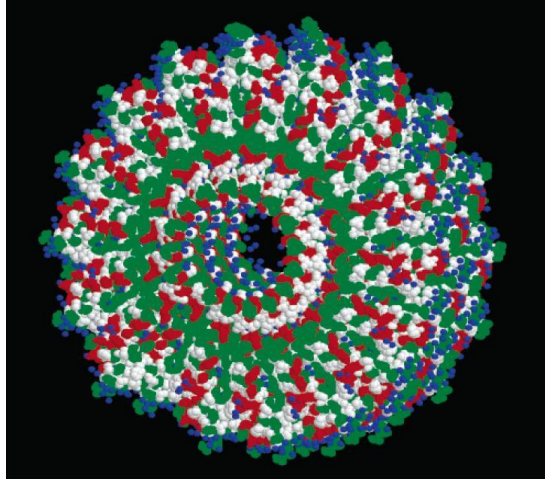


Figure 2.5: Model of the TMV disk showing the various amino acids. Hydrophilic amino acids are colored white, water molecules are colored blue, polar hydrophilic amino acids have a green color and the charged hydrophilic ones are red [86]

While the electrostatic interactions discussed previously are important in associating metal precursor ions onto the wild-type virus template, the strength of this bond is rather weak and therefore limits the use of the wild-type TMV in the realization of nanostructured materials. To address this issue, engineered modifications of the virus coat proteins have been the focus of research ever since the first complementary DNA cloning of the TMV was demonstrated by Dawson *et al* in 1986 [82]. Two of the first mutations were produced to investigate the amino acid interactions. These were point mutations of the glutamic acid to glutamine and of the aspartic acid to asparagine, resulting in the mutants E50Q and D77N respectively [90]. These modifications were found to contain only 25% of RNA to protein ratio as compared to the wild-type particle and they demonstrated an elongation in the virion from 300 nm to 940 nm.

Engineered modifications have also been created to improve the functionality of the TMV as a nanoscale template by the addition of reactive functional groups to the

inner and outer surface protein structure. The introduction of one or two cysteine residues in the coat protein open reading frame have been previously reported and were found to significantly enhance metal deposition as compared to the wild-type virus [85, 91]. Cysteines are amino acids that contain thiol groups, and the sulfur molecules of these thiols are hypothesized to take part in strong, covalent-like bonds with various metal ions and atoms. The strength of these bonds as well as the mild conditions needed for the interactions make the thiol group coupling an effective method for coating the TMV with biological and inorganic materials.

In this work, we use the TMV1cys, an engineered mutant of the wild-type virus containing one cysteine residue in each of its coat proteins. This modification is achieved through a process known as *PCR-based site-directed mutagenesis*, which has been extensively described elsewhere [82]. A complementary DNA clone is produced from the wild-type RNA and then used for the introduction of the cysteine. The specific codon (TGT in the case of cysteines) is introduced in the third position of the coat protein open reading frame. Following this process, RNA transcripts of this modified clone are used to infect the host plant, *Nicotiana tabacum cv Xanthi*, which acts as the factory for mass production of the virus. The infected leaves are harvested 20 days post inoculation and the virus is purified using a typical purification process [92]. Briefly, the plant leaves are frozen and then mixed in a blender with sodium phosphate buffer at the appropriate pH and chloroform, which is used to remove all unwanted cellular debris. Finally, the virus solution is extracted after the virus pellets undergo several centrifugation steps.

A schematic representation of the virus coat protein arrangement with the introduced cysteine residue is shown in Figure 2.6. Figure 2.6a shows a top view of the virion with the cysteines around the outer surface, while Figure 2.6b is an edge view showing the exposed functional groups on the 3' end.

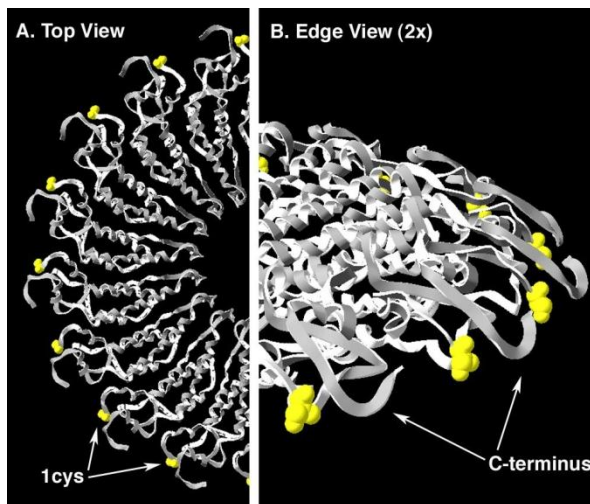


Figure 2.6: Structural location of the TMV1cys mutation: (a) Top view showing half of a coat protein layer within the TMV rod and (b) 2X magnification of an edge view for the same coat protein layer

2.3.2 TMV Applications

The Tobacco *mosaic virus* has been used as a structural nanomaterial both in its wild-type and mutated form. Knez *et al* reported the fabrication of nickel and cobalt TMV nanowires using electroless metal deposition [87]. The authors used the functionality of the protein chemical groups to act as linkers for metal ions as previously discussed in this chapter. The TMV virions were first activated with palladium and platinum catalysts in the presence of the appropriate reducing agents and a second electroless plating step was used to coat the virus surface with the nickel and cobalt particles (Figure 2.7a-b), resulting in wires 3 nm wide. In addition to this

electroless plating approach, Knez *et al* have also presented coating of the TMV with metal oxide nanoparticles (titanium oxide and aluminum oxide) using a room-temperature atomic layer deposition process [86]. Gorzny *et al* studied electron transport properties through Pt-coated TMV nanowires, demonstrating the feasibility of using this approach for next generation nano-devices [93].

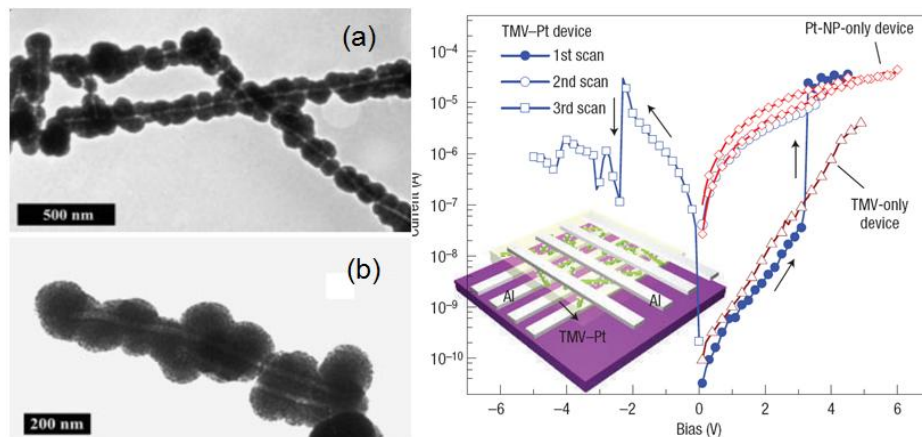


Figure 2.7: Synthesis of (a) nickel and (b) cobalt nanowires on the TMV [87]; (c) digital memory device using TMV templates [94]

A very interesting application of metal-coated wild-type viruses was presented by Tseng *et al* [94], where an electronic device was fabricated from these biomolecules coated with platinum nanoparticles (NP). The device demonstrated a digital memory behavior based on conductance switching between the ON and OFF states. Figure 2.7c shows the concept of this device, which consists of dispersed TMV-Pt nanowires in an insulating polyvinyl alcohol (PVA) matrix, sandwiched between two aluminum electrodes. The graph in Figure 2.7c shows an abrupt increase by three orders of magnitude in the measured current as the voltage is scanned above 3.1 V. The authors attribute this conductance switching effect to charge transfer from the RNA to the

platinum nanoparticles under the high electric field, which in turns changes the conductivity of the material system.

Collaborators at the University of Maryland (Dr. Jim Culver's group, Department of Plant Science and Landscape Architecture) have contributed significant advances in the field of TMV biomineralization, particularly with an emphasis on substrate attachment. [95]. Efficient templates for metallic coatings have been achieved through the introduction of one (TMV1cys) or two (TMV2cys) cysteine residues within the coat protein open reading frame. Cysteines are amino acids with thiol groups that show enhanced metal binding properties based on strong, covalent-like interactions. One and two-step electroless plating methods have been used for the fabrication of TMV2cys-based wires coated with gold, silver and palladium clusters that show more uniform coating compared to the wild-type virus [85, 91, 96]. Additionally, the rod-shaped viruses can be directionally attached to various surfaces and continuously coated to create high aspect ratio nickel, cobalt and platinum materials (TMV1cys). Near-vertical assembly of the TMV is feasible due to the exposed cysteines on the 3' (bottom) end of the virus, while the remaining engineered cysteine residues are recessed inside the viral structure that includes pits and grooves and are thus protected from making direct surface contact (see Figure 2.6). Figure 2.8 shows characteristic examples of this prior work.

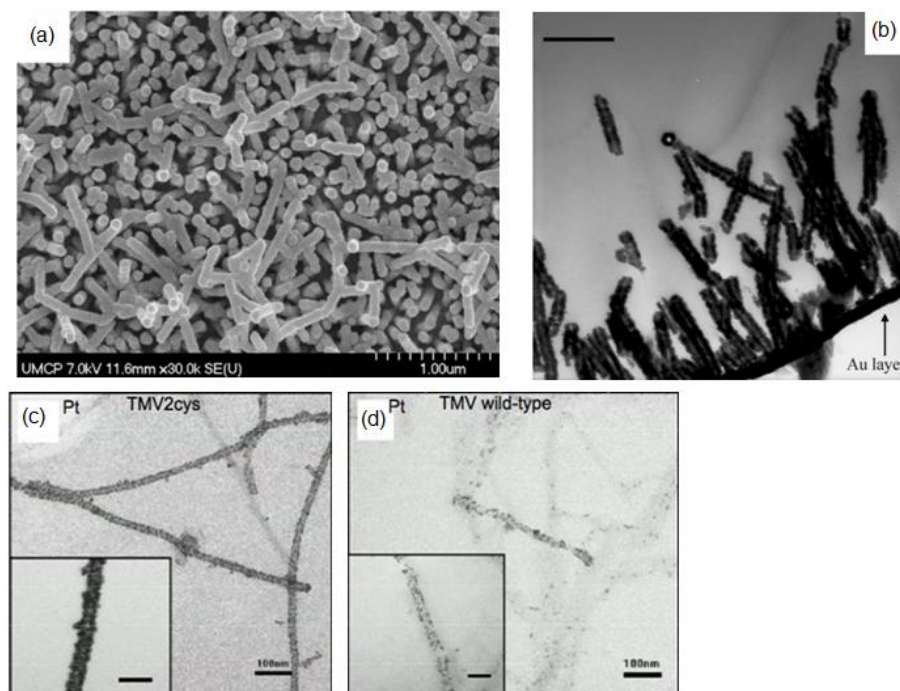


Figure 2.8: (a) SEM image of Ni-coated TMV attached on a Au surface, (b) cross-section TEM of the Ni-coated TMV [91], (c) improved Pt cluster deposition on TMV2cys compared to wild type TMV [85]

This technology is a significant advancement compared to the state-of-the-art in biotemplating processes since it allows fabrication of nano-textured surfaces directly on a substrate of interest and has served as the building block technology for this Dissertation as well as previous work in our groups. Metal-coated TMV1cys surfaces are highly stable and have been shown to maintain their conformation under repeated charge-discharge cycles within an alkaline electrode system [91]. In addition, this robust templating process inspired the fabrication of a 1st generation microbattery device that was developed in Master's research [97]. Continued work by the Culver group was focused on further increasing the stability of the TMV particles under varying process conditions, particularly for materials that cannot be directly deposited on the TMV. In this research, the focus was on the creation of a thick-shell silica

template, which was then used to show very stable alternating structures of silica-metal-silica templates [98].

2.4 Patterning of Biological Materials

While biotemplated nanostructures and biological molecules offer several attractive features for use in novel devices, a major bottleneck in their practical implementation is patterning in defined architectures. Due to stringent processing limitations, conventional top-down patterning techniques cannot be used; consequently, other avenues have been followed.

Scanning probe [99] and dip-pen [100] nanolithography (Figure 2.9b) techniques utilize AFM tips operated under different modes to transfer molecules of interest to a substrate through capillary and other interactions. Selective placement of DNA nanowires onto patterned electrodes can be achieved through self-assembly and functionalization with specific chemicals [101], while nucleic-acid hybridization has been shown to create intricate patterns of DNA in a robust, “one-pot” reaction [102]. Viruses and proteins can also be arranged on substrates through micro-contact printing (Figure 2.9a) [103, 104]. This technique uses an elastomeric structure fabricated through soft-lithography which is then wetted with the functional material and stamped on the target substrate. Notwithstanding individual advantages of these methods, they cannot always be scaled up (or down) at the wafer level or show compatibility with batch fabrication, attributes very important in high-throughput manufacturing.

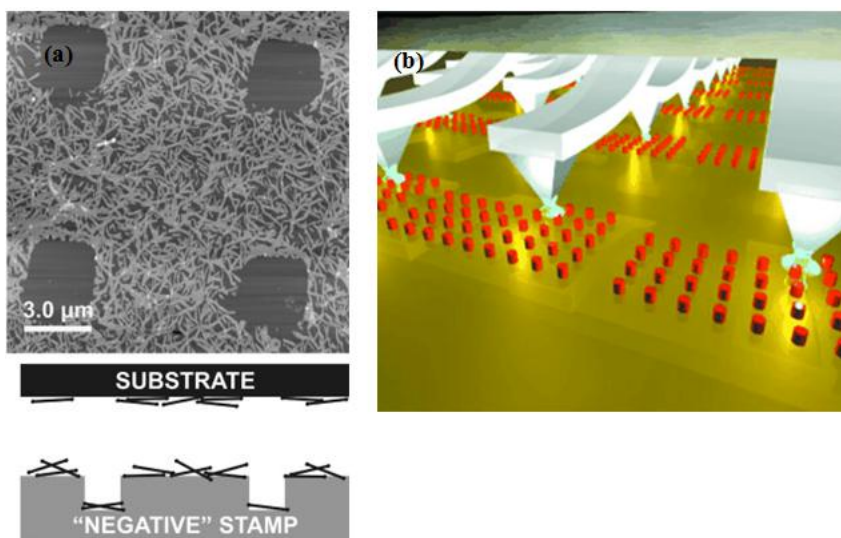


Figure 2.9: (a) Patterning of TMV using micro-contact printing [101], (b) assembly of biomolecules using dip-pen nanolithography [99]

In addition to developing structural TMV-templated materials, our TMV team has explored alternative pathways for patterning the viral molecules in microfabricated electrodes as well as controlled environments, utilizing nucleic acid hybridization. Our groups have worked closely to selectively assemble fluorescently-tagged TMV onto a chitosan-functionalized gold electrode (Figure 2.10) [105]. Chitosan, an amine-rich biopolymer which has been used extensively for the functionalization of sensor surfaces, is electrodeposited on the gold electrode and acts as an immobilization site for probe DNA; this is then linked with a complementary DNA chain attached to the viral RNA. In a more recent study, differentially labeled TMV nanotemplates were simultaneously addressed to defined substrate positions [106]. To accomplish this, the templates were programmed with linker DNAs containing sequence-specific addresses and then hybridized directly to the capture DNA. In short, modified virus particles were partially disassembled via pH 8.0 treatment, exposing the 5' end of the virus genome. Linker DNAs containing sequence

homology to the virus 5' end along with a unique address sequence were hybridized to exposed virus genome sequences. DNA oligomers with selectivity for the linker DNA address sequences were attached to glutaraldehyde-activated surfaces. These findings demonstrate that selective assembly of the TMV onto patterned surfaces is possible through nucleic acid hybridization.

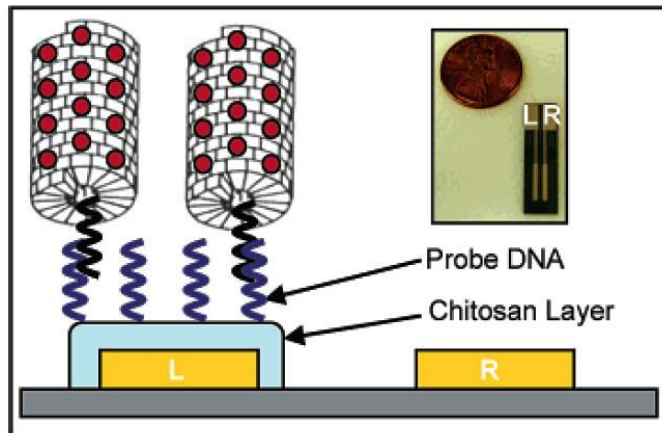


Figure 2.10: Conceptual schematic of TMV assembly using DNA hybridization on chitosan functionalized sites [107]

2.5 1st Generation TMV Microbattery

The Master's Thesis work that preceded this Dissertation was focused on the integration of the metalized TMV templates described in section 2.3 in microfabricated batteries, demonstrating the feasibility of creating functional devices with biotemplated nanostructures. The first generation microbattery device was based on the nickel-zinc chemistry, due to the availability of a nickel-coated TMV nanostructure. A schematic of this first device is shown in Figure 2.11a. The microbattery consisted of a nickel-coated TMV cathode assembled on a gold current collector on a silicon wafer. An electrolyte cavity was defined using photolithography with SU-8, which allowed the fabrication of different heights, ranging from 50 μm to

100 μm . After SU-8 fabrication, the devices were coated with TMV template, which was assembled uniformly throughout the substrate. The anode was a machined zinc plate with holes which allowed in-situ electrolyte circulation through a microfluidic package specifically designed for this cause (Figure 2.11b). This electrode was bonded to the counter electrode using adhesive bonding with SU-8 through a stamp-and-stick method described in detail in a previous publication [97].

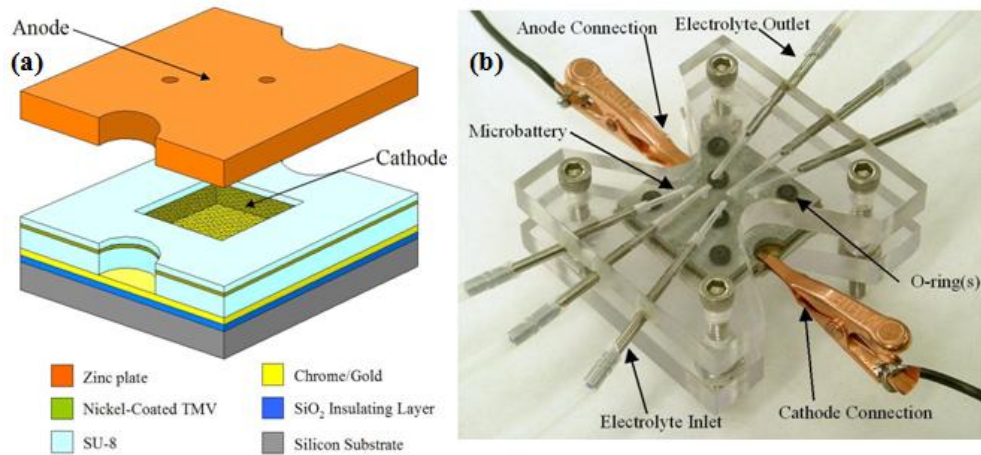
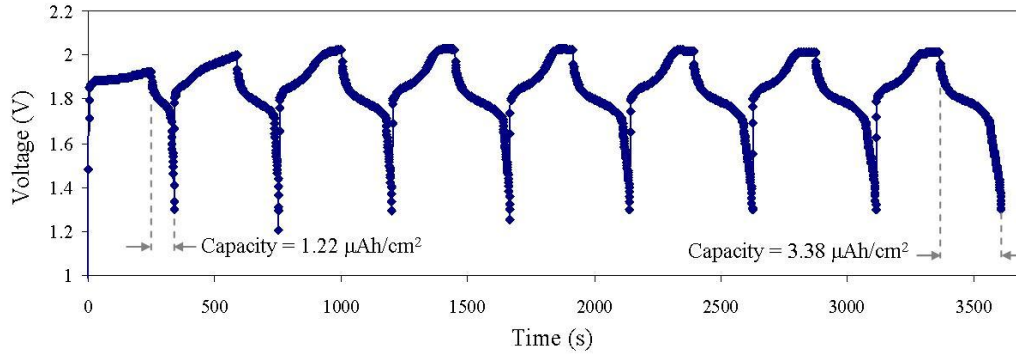


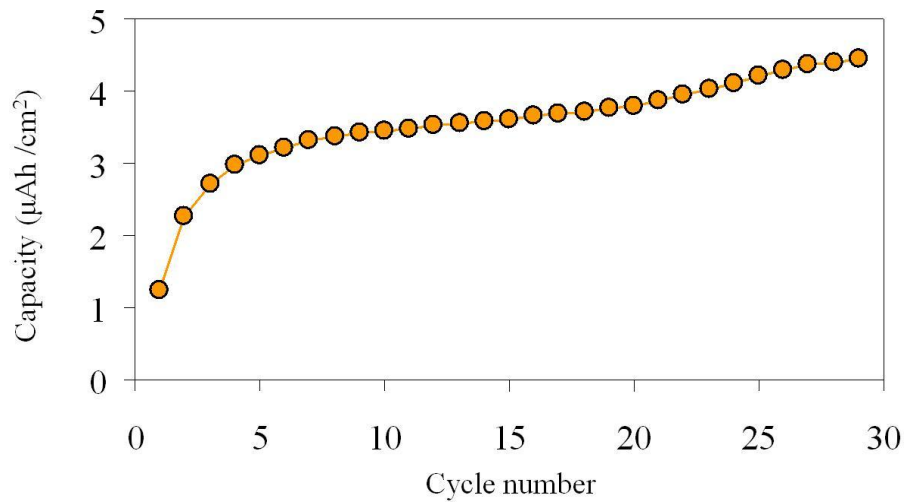
Figure 2.11: (a) Three-dimensional schematic of the 1st generation microbattery, (b) optical image of the microfluidic package developed for electrolyte circulation showing the microbattery with the fluidic and electrical connections

The devices were tested galvanostatically (at constant current) using a liquid electrolyte of 4 M KOH. For comparison, microbatteries with planar nickel cathodes (i.e. electrodes without TMV) were also tested. Figure 2.12 shows the cyclic behavior of a TMV-structured microbattery for the first 8 cycles of operation at a discharge current of 100 $\mu\text{A}/\text{cm}^2$. This microbattery had an active area of 0.64 cm^2 and a spacing of 65 μm between the anode and cathode. The discharge/charge curves show the appropriate plateaus and shape for the nickel zinc chemistry. In this device, the capacity increases gradually from 1.22 $\mu\text{Ah}/\text{cm}^2$ to 3.38 $\mu\text{Ah}/\text{cm}^2$. This is attributed to

the progressive conversion of more nickel oxide to nickel oxyhydroxide. Figure 2.13 shows a plot of the capacity vs. cycle number for this device, which achieved a maximum capacity of $4.45 \mu\text{Ah}/\text{cm}^2$. The microbatteries operated properly for up to 25 discharge/charge cycles after which dissolution and re-deposition of the Zn on the anode resulted in gradual dendrite formation and shorting with the TMV covered sidewalls of the electrolyte cavity. These two observations were used to guide future research directions as they dictated a shift towards more stable chemistries as well as the necessity of patterning the TMV-templated electrodes.



2.12: Charge/discharge curves for a TMV-structured Ni-Zn microbattery showing the first eight cycles of operation



2.13: Capacity vs. cycle number for the device of 2.12

Figure 2.14 shows a plot of the voltage vs. capacity for several samples with and without viral nanotemplates. It can be observed that an approximately six-fold increase in capacity was achieved for the TMV-templated electrodes. This is a direct result of the increase in surface area added by the TMV and demonstrates the significant benefit of using this technology for nanostructured battery devices.

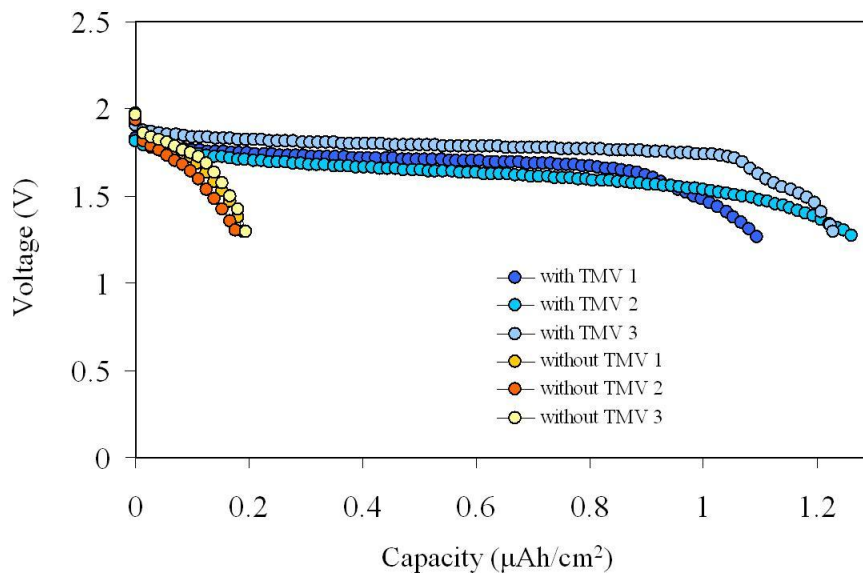


Figure 2.14: Voltage vs. capacity for microbatteries containing electrodes with and without TMV

2.6 Summary

This Chapter discussed some fundamental concepts and processes that are the base for the work conducted in this Dissertation. More specifically, the basics of battery operation were presented and the concepts of capacity and energy density were introduced and related to microbattery devices. The focus was then shifted to biotemplating processes to present the benefits of this approach, with an emphasis on the TMV and how previously developed genetic modifications can result in self-assembled viral nanostructures. Finally, previous work on using these templates for a

1st generation of devices was presented, identifying both merits and limitations of this technology that will be further addressed in this work.

Chapter 3 : Biofabrication Processes for the Patterned Assembly and Synthesis of Viral Nanotemplates

The processes presented in this chapter were inspired by the previous Master's work which identified some limitations in the integration of the TMV templates in high performance devices. The first limitation that is addressed is related to the patterning capabilities of the TMV. While in the initial work combining the TMV biofabrication with MEMS technology resulted in a working prototype, more facile and batch-processing compatible devices can be produced if the TMV can be patterned at the wafer level using processes similar to those used in standard MEMS fabrication. More specifically in this chapter, photolithographic patterning of both metal coated as well as uncoated TMV will be presented. This process is a significant advancement in the patterning of biotemplated nanostructures and creates new opportunities for virus-structured devices that are not limited to the energy field only. In addition, the TMV self-assembly properties can be leveraged to create intricate three-dimensional hierarchical structures that combine top-down microfabricated architectures with the metal-coated viral scaffolds. These structures are the basis for the novel microbattery electrodes that will be described in Chapter 5. Finally, since metallization of the TMV is efficient only for a limited number of materials, new synthesis techniques had to be identified to enable the TMV template utilization in next-generation high performance energy devices that are not limited to alkaline chemistries only. To accomplish this, the metal-coated TMV nanonetwork was used as a template itself and combined with highly uniform and conformal thin-film

deposition processes that enable the formation of core/shell nanostructures where a nickel-coated TMV core is covered by the active material of interest. Overall, the processes presented in this chapter constitute the first demonstration of combining bottom-up biological self-assembly with top-down fabrication for the development of a bionanomanufacturing process toolbox which can be used in a variety of applications. The results from this work have been archived in a journal article published in *Nanotechnology* in 2010 [108].

3.1 Photolithographic Patterning of TMV

The basic concept of the TMV photolithographic patterning is derived from the conventional lift-off process that is used in the MEMS and semiconductor industry to pattern metallization lines. Photoresist is used to transfer the desired features from an optical mask onto the wafer which is then immersed into a pH 7 phosphate buffer (PBS) solution containing the virus. After TMV self-assembly on the substrate, the photoresist is removed in a solvent or developer solution, leaving TMV only on the patterned surfaces. Depending on the type of TMV nanostructure that has to be patterned (uncoated TMV1cys or nickel-coated TMV1cys), this general approach is modified accordingly to facilitate processing as well as characterization of the samples using high resolution microscopy techniques. Both methodologies are shown schematically in Figure 3.1 and described in detail in the following subsections.

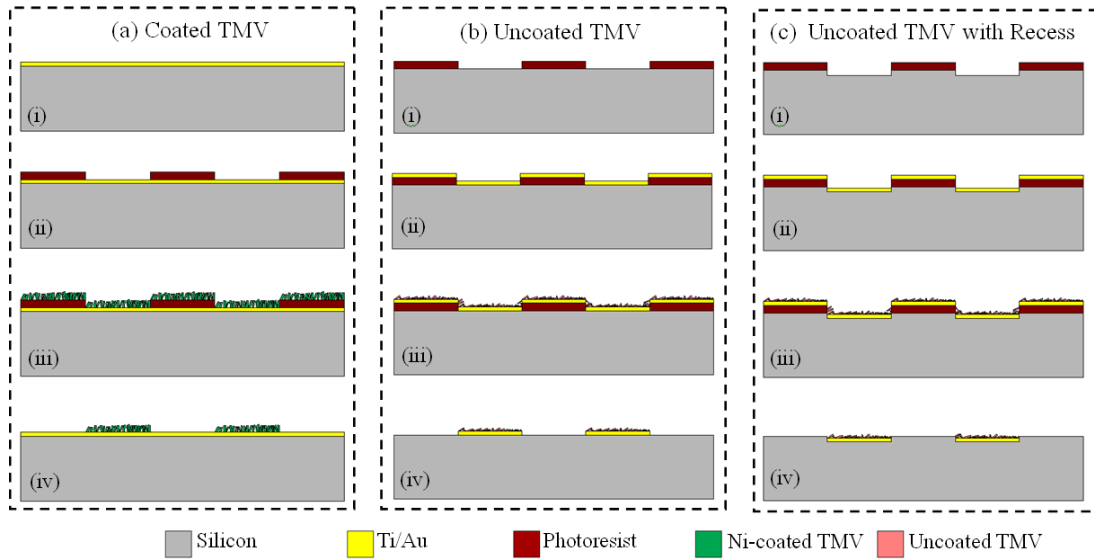


Figure 3.1: Schematic representation of the lift-off patterning processes for nickel-coated TMV (a), uncoated TMV (b) and uncoated TMV with an etched recess – (a) Coated TMV: e-beam evaporation of Ti/Au (i), photolithography with positive or negative photoresist (ii), TMV assembly and Ni coating (iii) and removal of photoresist in acetone (iv). (b) Uncoated TMV: photolithography with positive photoresist (i), Ti/Au evaporation (ii), TMV assembly (iii), lift-off of Au and TMV in a developer mixture or acetone (iv). (c) Uncoated TMV. After photolithography, a shallow recess (1 μm) is etched using DRIE (i), steps (ii), (iii) and (iv) are identical

3.1.1 Nickel-coated TMV Patterning

The fabrication begins with evaporation of titanium and gold metal layers on a p-type 4-inch silicon wafer to thicknesses of 10 nm and 50 nm respectively. This step is followed by photolithography using an optical mask that contains various features (lines, squares and circles) with size and spacing ranging from 100 μm down to 2 μm ; this is the minimum feature size that can be obtained from the mask manufacturer for contact alignment. Both positive and negative photoresists (Shipley 1813 and image-reversed AZ5214 respectively) with varying thicknesses were employed. For Shipley

1813, the wafer was exposed in a contact aligner (Quintel Q-4000) with a dose of 180 mJ/cm² and developed for 30 s in Microposit 352. When AZ514 was used, the wafer was exposed with the mask at 40 mJ/cm², post-exposure baked at 125°C for 45 s and then flood-exposed (no-mask) at 2000 mJ/cm² to invert the polarity. Development was performed in a mixture of AZ400K developer and water in a 1:6 ratio for 2 minutes.

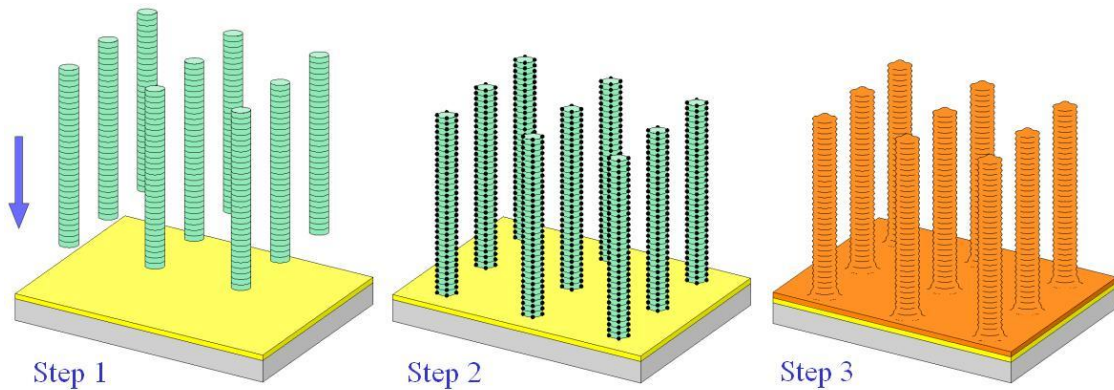


Figure 3.2: Generalized schematic of the TMV self-assembly and nickel-coating process

After development, the three-step viral self-assembly and nickel coating process is performed on cleaved chips as previously described [97]. Briefly, the process consists of three-steps and is illustrated in Figure 3.2. The chips are placed in a sodium phosphate buffer solution containing the virus at a concentration of 0.1 g/L and allowed to incubate overnight. After TMV self-assembly, the die are immersed for a few hours in a palladium catalyst solution prepared by mixing a palladium salt (sodium tetrachloropalladate, NaPdCl₄, 98%) with phosphate buffer (ratio of 1:10 to 1:15) and finally they are coated with nickel in an electroless plating solution in which they are immersed for 3-5 minutes. The electroless nickel plating solution consists of nickel (II) chloride hexahydrate (NiCl₂, 99%), sodium tetraborate

($\text{Na}_2\text{Ba}_4\text{O}_7$, 99%), dimethylamine boarane (DMAB, 97%). Finally, the metallization step is followed by treatment of the samples in an acetone bath using ultrasonication.

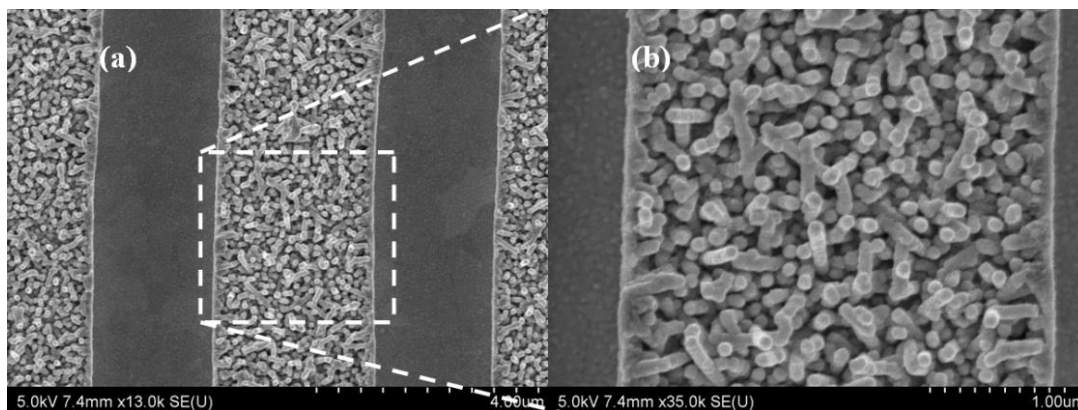


Figure 3.3: SEM images of patterned nickel-coated TMV features; (a) microfabricated virus-coated lines with size and spacing of 2 μm and (b) close up view of the textured surface

The patterning approach for the TMV-templated metallic nanostructures is simple and straightforward due to the remarkable robustness of coated viruses in solvents as well as the ability to characterize the samples directly using Scanning Electron Microscopy (SEM). Immersion of the photoresist-patterned nickel-coated chips in an acetone bath followed by ultrasonication results in lift-off of the underlying photoresist layer leaving the nickel-coated viruses onto the patterned surfaces. Figure 3.3 shows SEM images of the minimum patterned feature size including a close up view of the textured surface. The SEM images demonstrate that nickel-coated TMV-structured lines with size and spacing as small as 2 μm can be clearly resolved. It is also observed that the metal coating enables nanoscale three-dimensional assembly of the otherwise flat-laying virus resulting in very high surface area patterns. This near-vertical assembly has been explained in detail in previous publications [91, 97] and it is very important in applications such as battery electrodes and fuel cell catalysts where maximum surface area is desirable. The patterning methodology investigated

using this lift-off technique is independent of the photoresist polarity or thickness and it is limited only by the minimum mask feature size. While the concept has been demonstrated using nickel coating, the process has also been successfully combined with other similar solution-based coating recipes that were developed by our group. This versatility and simplicity make it a very promising candidate for large-scale manufacturing of nanostructured templates.

3.1.2 Uncoated TMV Patterning

Two important considerations had to be taken into account when developing the fabrication process for the uncoated TMV. First of all, extensive treatment of the virus in solvents (commonly used solutions for photoresist removal) can result in structural destabilization of the TMV or other peptides that could be potentially attached on the virion surface; this led to the investigation of alternative methods to remove the polymer masking layer based on less reactive solutions. The second requirement is pertinent to the sample characterization which is conducted with both SEM and Atomic Force Microscopy (AFM) in this experiment so that nanoscale structural effects can be analyzed. Uncoated TMV cannot be viewed with an optical microscope and this necessitates the use of “alignment marks” to achieve correct placement of the AFM tip on patterned and unpatterned areas. The first concern is addressed by employing positive photoresist during photolithography, since this type can be treated with UV light after fabrication and removed with both solvent and developer mixtures. To facilitate imaging, the base gold layer for TMV assembly is deposited after photoresist patterning (as in standard lift-off) so that discrimination between patterned structures can be made easily.

The process begins with the photolithography step using Shipley 1813 as the positive resist on a 4 inch silicon wafer with the same optical mask. The photoresist is exposed for 15 seconds under UV light and then developed with Microposit 352. After development, the wafer is flood-exposed for 30 to 40 seconds to allow lift-off in the developer solution. Before metallization, some of the wafers are shallow-etched with Deep Reactive Ion Etching (DRIE) to a depth of approximately 1 μm (Figure 3.1c); this small fabricated recess was expected to accelerate the lift-off process and was investigated for comparison with the standard method. E-beam evaporation is then used to deposit thin films of titanium (10 nm) and gold (50 nm) on the wafer. Finally, the wafer is cleaved and the individual chips are immersed in the TMV-containing solution (concentration of ~ 0.1 mg/mL) and allowed to incubate overnight.

Two lift-off methodologies utilizing photoresist developer and an acetone solution were investigated. The developer is a highly basic solution (pH 13-14) consisting of sodium hydroxide, sodium tetraborate, boric acid and water; for this application, it was mixed with sodium phosphate buffer (0.1M, pH 7) at ratios of 1:3 and 1:5 which resulted in a decrease in the pH of the mixture to values of ~ 9 and ~ 8 respectively. These milder conditions were necessary to avoid destabilization of the virus structure. The chips were immersed in the solution and placed on a hotplate heated at 55°C to accelerate the photoresist removal process. This temperature was selected again based on literature findings regarding the virus stability in certain temperature ranges. Lift-off in acetone was more straightforward and involved immersion of the die in the solvent at room temperature.

In both cases, slight manual agitation was applied periodically to assist the process. The developer-based process was, as expected, slower and required 5 to 7 hours for patterning of features down to 10 μm . Smaller features required treatment up to 30 hours to be completely resolved and partial structural destabilization was observed for such long process times. In all cases, continuous agitation accelerated the lift-off rate. On the other hand, gold/virus lift-off in acetone proceeded at a faster pace (1-2 hours for similar feature sizes). It was also observed that in the wafers without the shallow-etched trenches photoresist removal was even slower. After completion of the process, the samples were rinsed in DI water and dried on a hotplate at 40°C.

Figures 3.4a and 3.4e show optical images of chips patterned in the developer mixture (1:5) and acetone, respectively. It can be clearly seen that gold features have been lifted off from the silicon substrate. The nanostructure of the patterned surfaces was investigated using an Atomic Force Microscope. Figures 3.4b and 3.4f show height scans of untreated TMV surfaces on gold substrates which were used as control while Figures 3.4c, 3.4g, 3.4d and 3.4h are scans of gold and silicon areas from the samples of Figures 3.4a and 3.4e respectively. In all images it is seen that, unlike the case of the metal-coated TMV, the viruses lay flat on the substrate as a result of the drying process since there is no coating layer to provide the three-dimensional support.

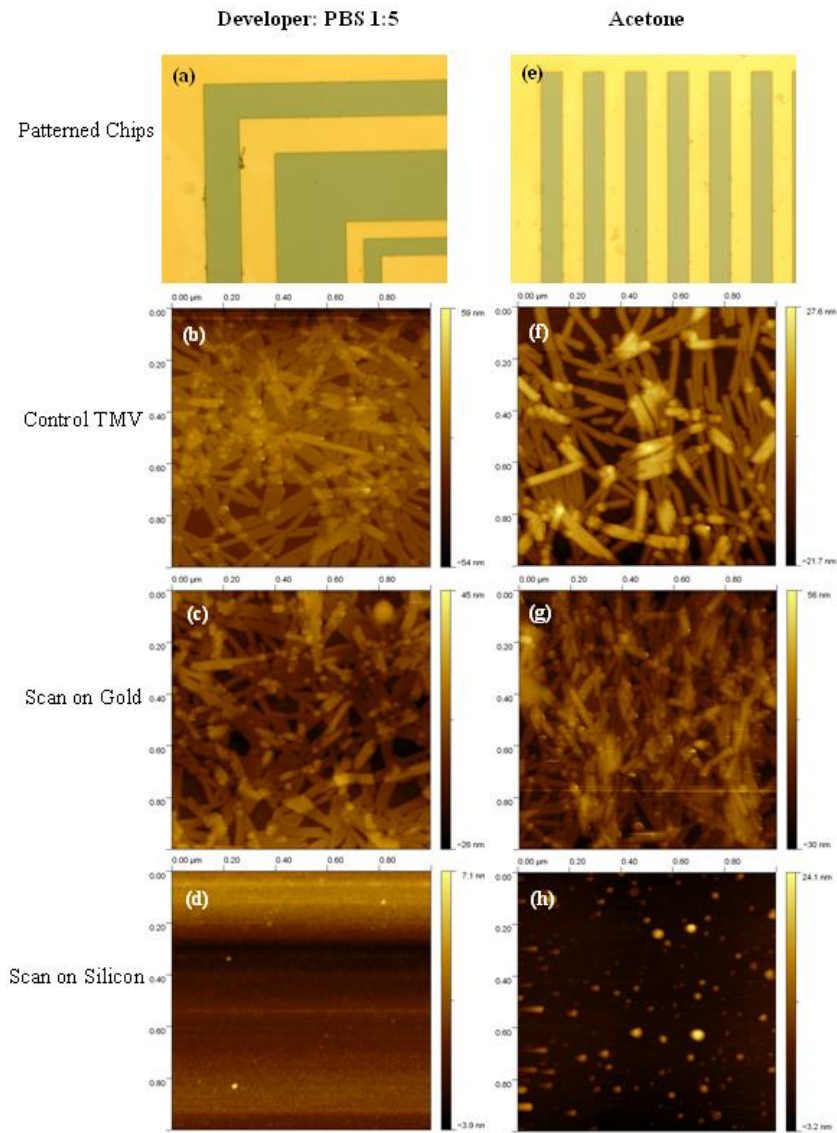


Figure 3.4: Images of TMV coated chips patterned in developer:buffer 1:5 mixture (left column) and acetone (right column) (a, e) optical images of chip surface showing that coated gold has been removed selectively, (b, f) AFM height scans of an untreated control surface cleaved from the same substrate before immersion in the respective patterning solution, (c, g) AFM height scans of the gold surfaces of figures (a) and (e) and (d, h) AFM height scans of the silicon surfaces of (a) and (e)

The interface between the gold and silicon surfaces on chips patterned using developer mixed with PBS in a 1:3 ratio and acetone are shown in Figure 3.5 where the selectivity in TMV patterning is clearly demonstrated. By comparing the

untreated and developer-patterned surfaces it can be observed that the mild-pH lift-off process does not affect the virus structure when the dilution is performed in the range of 1:3 to 1:5. On the other hand, samples treated in the solvent solution show a different morphology compared to the untreated TMV as evident from the height scan in both the gold and silicon areas as well as the height and phase images of Figure 4 that show additional virus fragments on the surface. This is attributed to precipitation of the coat proteins in acetone which results in unfolding as well as fracturing of the virus particles and successive irregular assembly across the chip area.

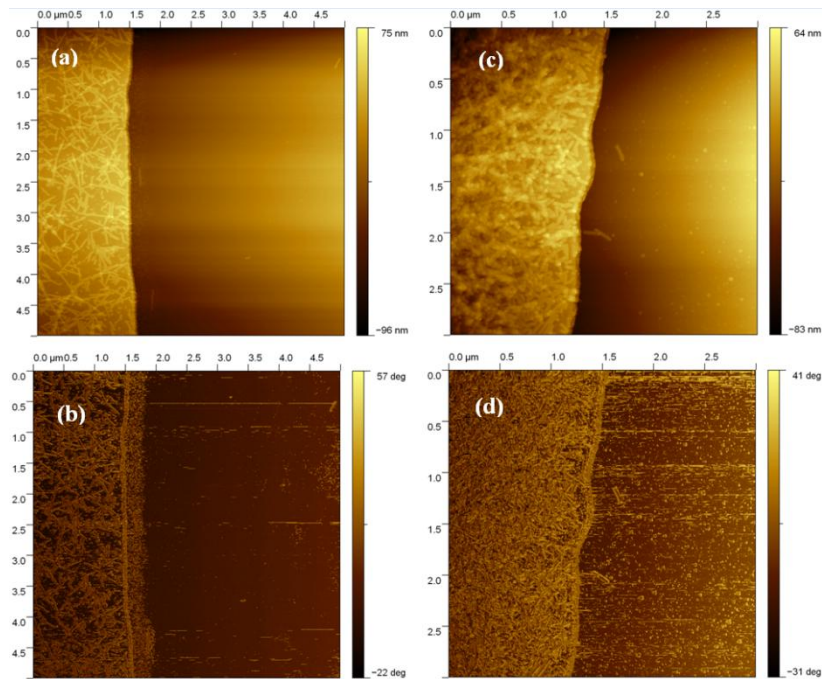


Figure 3.5: AFM height scans of the interface between gold and silicon of chips patterned in a 1:3 developer/buffer mixture (a) and acetone (c). Figures (b) and (d) show the phase mode AFM scans for (a) and (c) respectively

The post-patterning chemical functionality of the uncoated TMV was investigated for both techniques by attempting metallization of the structures. Optical microscope inspection was employed to determine that the gold areas were removed from the

silicon substrate. Once successful photoresist removal was verified, the samples were gently rinsed in a PBS solution without prior drying and then metalized with nickel using the two-step process described earlier. Figures 3.6a and 3.6b show characteristic SEM images of chips patterned in developer (5:1) and acetone respectively. It is observed in both cases that the TMV is successfully metalized. In the developer-processed specimens a small number of fragments were found in the silicon areas, which could be due to re-deposition of solution-excess viruses during the lengthy process. This effect is more pronounced however when TMV is immersed in acetone as was indicated in the AFM analysis as well. In addition to cases of TMV fragments, poor coverage of the substrates was occasionally observed in acetone.

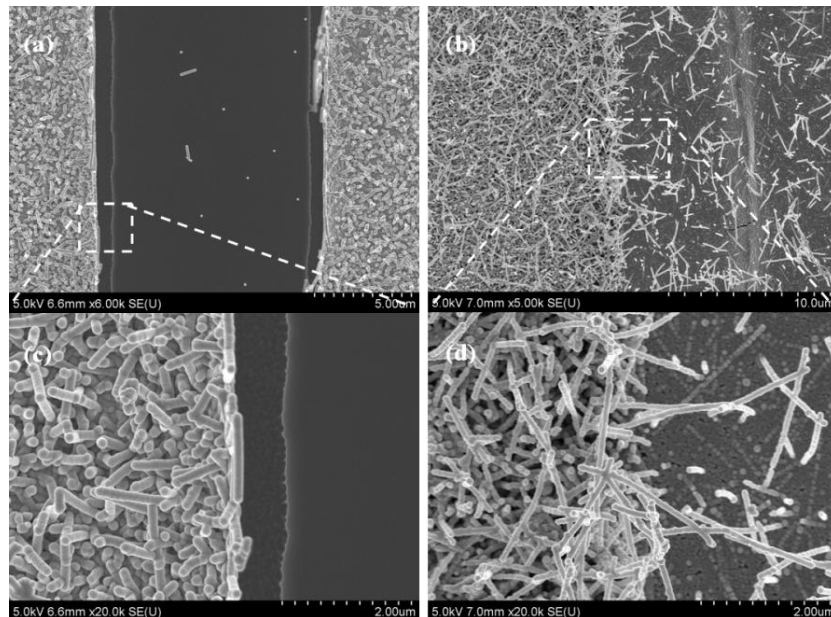


Figure 3.6: SEM images of TMV that was first patterned in 5:1 buffer:developer mixture (a) and acetone (b) and then coated with nickel to verify post-patterning chemical functionality. Images (c) and (d) show close-up views of the textured surfaces

In conclusion, two lift-off methodologies for the patterning of uncoated TMV on microfabricated structures have been successfully developed. The developer-based

process is lengthy as several hours are required to resolve virus-coated structures as small as 10 μm however no structural degradation or difference in morphology compared to untreated surfaces has been observed during these times. When the process is performed in acetone, features are lifted off faster but negative effects on the virus structure have been noticed with variability even on the same substrate. Since post-patterning chemical functionality is maintained, depending on the requirements of a specific process, the most suitable of the two techniques can be adopted.

3.2 Assembly on Three-dimensional Geometries

Assembly of high aspect ratio nanostructures on three-dimensional microstructures is a very attractive approach in applications where increased surface area in the out-of-plane dimension is particularly beneficial, such as microfluidic wicking structures and active battery electrodes. The self-assembly properties of the virus in simple solution-based reactions and the functional groups on its surface enable the integration of the TMV-templated materials into such complex architectures. Two methods were investigated to demonstrate the feasibility of this three-dimensional assembly; the first method is a direct extension of the in-plane biofabrication and utilizes silicon substrates etched using DRIE and sputtered with metal layers. The second process was inspired by findings of our previous work, where it was observed that TMV adheres to polymers as well [97]. Here, SU-8 is employed for the fabrication of microstructured surfaces on which assembly of the nickel-coated viruses is achieved. In addition to their relevance to the current research, both processes are very commonly used in MEMS fabrication in general.

Silicon structures were etched in an STS DRIE with a rate of 3 $\mu\text{m}/\text{min}$ to a depth of 240 μm . The etching mask was a 5.5 μm thick AZ9245 photoresist. The resist was spun at speeds of 1750 rpm for 5 s and 3000 rpm for 40 s and soft-baked at 110°C for 90 s. The wafer was exposed at a dose of 300 mJ/cm^2 and developed in a mixture of AZ400K and DI water in a 1:3 ratio. After etching, photoresist was removed in acetone and layers of chrome (50 nm) and gold (250 nm) were sputtered on the substrate in an AJA sputtering unit. The polymer structures were fabricated on silicon wafers which were cleaned in acetone, methanol, isopropyl alcohol and DI water in ultrasonics and dehydrated at 200°C for 20 minutes. SU-8 50 was spun at speeds of 600 rpm and 2500 rpm and soft-baked at 75°C with a ramp of 300°C/hr for 50 minutes. Exposure was performed in the aligner for 80 s and post-exposure bake followed under the same conditions as the soft-bake. The wafer was finally developed in SU-8 developer for 10 minutes with agitation.

Following the microfabrication processes, individual chips from both wafers were coated with TMV and nickel as described in the previous section. SEM images of the coated substrates as well as close-up views of the textured surfaces are shown in Figure 3.7. The mechanism that enables TMV attachment onto SU-8 has not been clearly defined. The effect of the cysteine mutation was investigated by the addition of diethyl-triethol (DTT) to the virus solution, a chemical that can impede the functionality of the cysteine amino acid. Little or no difference was observed however in the density of the coated TMV on SU-8 after this treatment, indicating that the engineered cysteine residues do not play a direct role in SU-8 attachment.

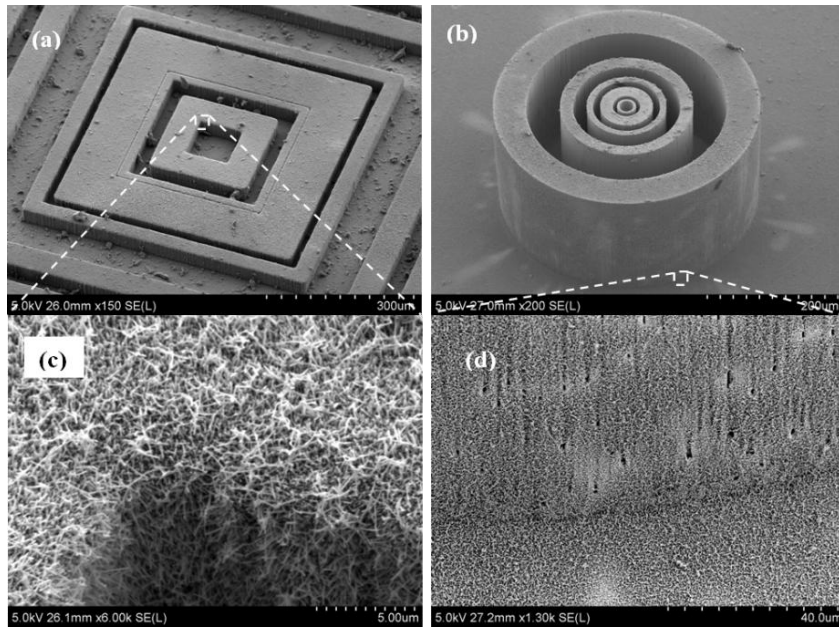


Figure 3.7: SEM images of three-dimensional microstructures covered with nickel-coated TMV, (a) SU-8 structures, (b) structures etched in silicon. Bottom pictures (c) and (d) show exploded views of the textured surfaces outlined by the dotted areas in (a) and (b)

Comparison of these two processes indicates that, while silicon etching allows the realization of higher aspect ratio structures than SU-8 and can be used in applications where a conductive substrate is required, sidewall coverage was not as consistent as in the polymer case. More specifically, cases were identified in the silicon structures where both interior sidewalls and bottom surfaces (in between features) were not as densely coated as other similar features even on the same chip (Figure 3.8, a-c). Similar variability was not seen in SU-8. These observations indicate that diffusion of the liquid through the high-aspect ratio structures as well as insufficient gold coverage and difference in wettability of the gold-sputtered silicon and SU-8 surfaces must be among the causes for this inconsistency.

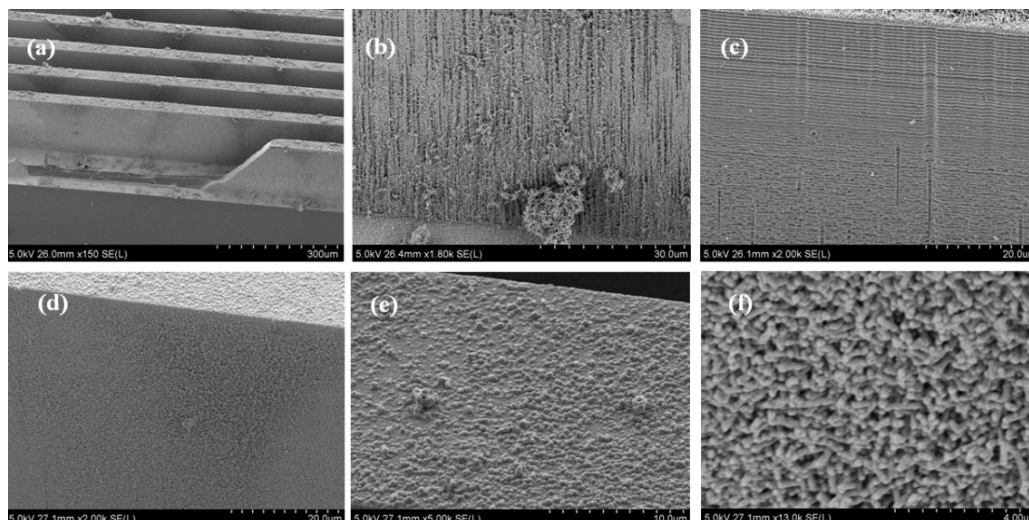


Figure 3.8: (a) Cleaved high aspect ratio structures in silicon, examples of (b) uniformly covered sidewall and (c) poorly covered sidewall); (d) a similar structure coated with constant stirring of solutions; close-up views of top (e) and sidewall (f) surfaces of (d)

The effect of liquid diffusion and surface wettability was investigated by stirring the TMV and electroless plating solutions. This was achieved by placing the chips vertically inside a 10 ml beaker with the aid of a three degree of a freedom stage and placing the assembly on a hotplate to provide magnetic actuation. It was observed that stirring results in consistently denser sidewall coverage; however, fragmentation of the TMV especially on the exposed top surfaces was a negative side effect (Figure 3.8, d-f). Based on these results, better utilization of the silicon structures can be achieved by using coatings that can decrease surface tension, adopting alternative geometries (e.g. cylindrical posts) or by adjusting the lateral distance between structures such that liquid can easily access all features of interest.

3.3 Synthesis of Core/Shell Nanostructures Using the TMV

The diverse nature of nanomaterial applications requires the existence of templates that can be versatile and allow synthesis of a broader range of functional

surfaces. The previously developed templating methodologies have been limited to the use of electroless plating reactions for the decoration of TMV with inorganic particles. Utilizing these metallic templates other micro/nanofabrication approaches can be integrated into TMV-based materials synthesis. ALD is a unique deposition method that is ideally suited for uniform coating of high aspect ratio surfaces. In this work, the feasibility of conformal deposition of materials onto the nickel-coated TMV surface was investigated. Two established recipes for aluminum oxide (Al_2O_3) and titanium oxide (TiO_2) were used as a proof-of-concept demonstration; however, this method can be expanded to include any material that can be deposited using ALD.

Samples for ALD deposition were prepared using the photolithographic patterning technique described in section 2.1.1. The utilization of patterned chips was preferred over plain nickel-coated surfaces because it provides consistent locations for SEM characterization before and after deposition. In this experiment, a lower concentration of TMV1cys was selected, typically 0.05 or 0.075 mg/mL. At lower concentrations, the packing density of the nanostructured materials is decreased and this facilitates easier imaging of individual virus particles.

For the fabrication of the samples, the nickel-coated patterned chips were placed in a TFS 500 BENEQ™ ALD reactor. The deposition of Al_2O_3 was performed using alternate pulse sequences of Trimethyl Aluminum (TMA) and H_2O at 220°C while the deposition of TiO_2 utilized Tetrakis-Dimethyl Amido Titanium (TDMAT) and H_2O at 150°C . The measured deposition rate for these recipes has been determined to be 0.1nm/Cycle for Al_2O_3 and 0.05nm/Cycle for TiO_2 , close to reported values in literature [109]. The target thickness for both the deposited layers was kept to be 30

nm to enable observation of a notable change with the electron microscopy imaging techniques.

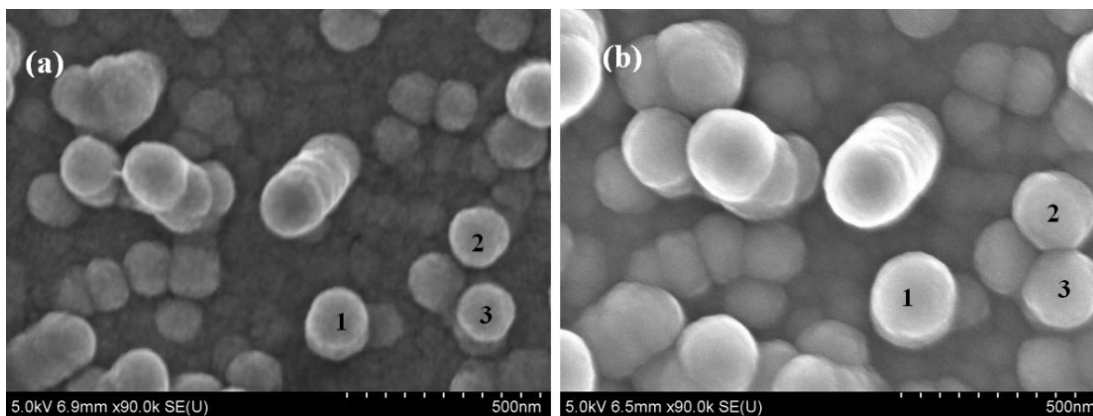


Figure 3.9: SEM images of patterned nickel-coated TMV structures before (a) and after (b) ALD coating of TiO_2 – The diameter of particles 1 to 3 has been measured using ImageJ software to be 151 nm, 149 nm, 144 nm in (a) and 214 nm, 206 nm, 197 nm in (b)

SEM images of nickel-coated TMV surfaces before and after deposition of 30 nm of TiO_2 are shown in Figure 3.9. Comparison of the rod diameters on the marked vertically-aligned particles 1 to 3 shows an increase after the ALD process. This increase has been estimated using ImageJ software to be on the order of 30 nm, which was the intended thickness based on the processing parameters.

The coating uniformity was further investigated using cross-sectional Transmission Electron Microscopy (TEM). The TEM samples were prepared as follows: chips for TEM analysis were prepared on a freshly-cleaved mica substrate where a thin layer of gold has been thermally evaporated to serve as a base for TMV assembly. The ALD-TMV-coated mica substrates were first dehydrated in 70%, 95% and 100 % (2 times) acetone for 10 minutes each time. Spurr's resin was prepared as suggested in [110] and the chips were immersed in mixtures of acetone:Spurr's at ratios of 1:1, 1:2 and 1:3 for 30 minutes each time. After immersion in 100% Spurr's

for 1 hour, the chip was embedded in Spurr's and the resin was polymerized overnight at 70°C in an oven. Thin sections (70 nm) were obtained with a diamond knife and mounted onto carbon/formvar coated TEM grids.

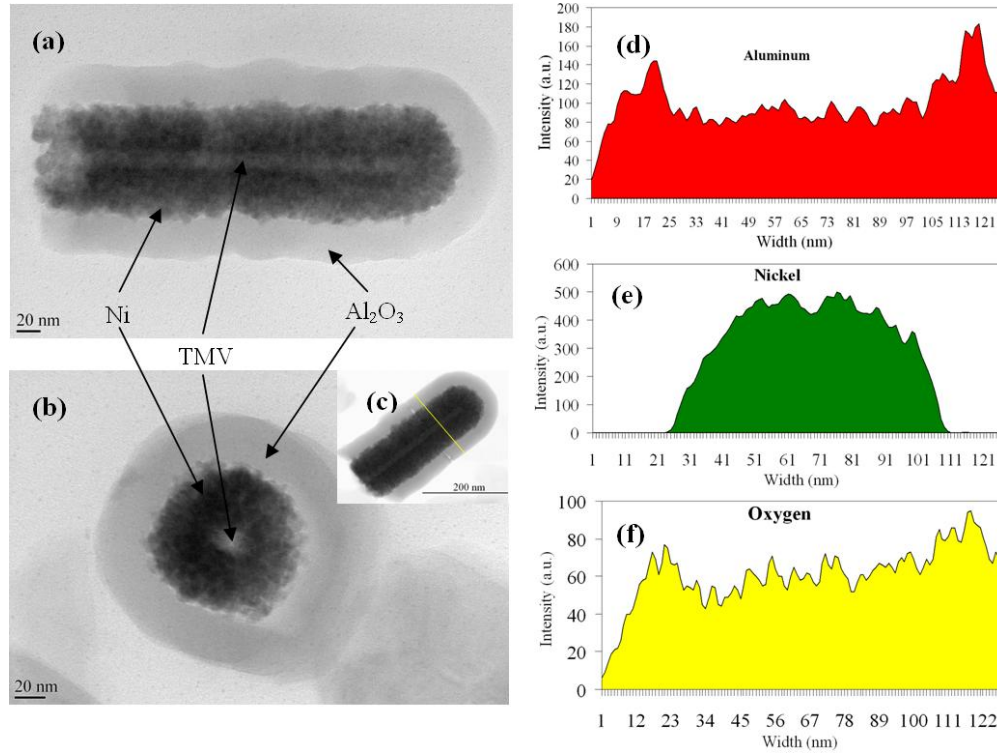


Figure 3.10: Side (a) and bottom (b) view TEM images of TMV particles coated with layers of nickel (electroless plating) and Al_2O_3 (ALD) – EDS line scan data of the STEM image (c) are shown on the right for the elements of interest (Al, Ni, O). It can be seen that aluminum signal is picked from the start of the line scan (d) while nickel signal is zero until ~25 nm (e); this indicates that the first coating layer is due to ALD of Al_2O_3 - oxygen (f) is due to both materials

Figures 3.10a and 3.10b show the side and bottom view of an individual TMV particle while Figures 3.10d-3.10f contain the corresponding Energy-Dispersive X-ray Spectroscopy (EDS) data of the particle in the inset (Figure 3.10c). Oxygen is present due to both the Al_2O_3 as well as nickel that has been oxidized. It can be seen that aluminum signal is picked from the start of the line scan (d) while nickel signal is zero until ~25 nm (e); this indicates that the first coating layer is due to ALD of

Al₂O₃ - oxygen (f) is due to both materials. The absence of any signal from nickel until approximately ~25 nm indicates the excellent coating uniformity of the Alumina layer.

ALD has been previously employed by other researchers for TMV coating, as discussed in Chapter 2. Knez *et al* demonstrated a room temperature deposition process for the decoration of TMV with layers of alumina and titania [86]. In the work presented here, two significant advancements have been achieved. Deposition of composite materials on the nickel-coated virus surface expands the toolbox of available processes since the structure of the virus is entirely protected by the thin metal coating thus allowing higher-temperature recipes to be applied without structural degradation of the virus. Tuning of the layer thicknesses is also possible by adjusting the deposition parameters for electroless plating and ALD steps. Additionally, the surface-attaching properties of the cysteine-modified TMV1cys as well as the photolithographic patterning capability enable in-situ synthesis of the desired materials without any requirement for post-integration in a device or substrate since the ALD and coated TMV lift-off processes could be combined for selective deposition of the films.

3.4 Example: TMV Biofabrication for Superhydrophobic Surfaces

An example of the TMV biofabrication process is presented in this section. This work was conducted in collaboration with colleagues at the Massachusetts Institute of Technology and Drexel University, who have been interested in fabricating hierarchical superhydrophobic surfaces for self-cleaning applications, textiles, and solar panels as well as for reducing drag or heat transfer. In this investigation, the

objective was to biomimetically recreate the structure of aquatic plant leaves, which have demonstrated natural self-cleaning properties. This study can shed light into the governing mechanism of this phenomenon and assist in engineering of similar solutions for the aforementioned novel applications. These aquatic plant leaves, such as the lotus leaf, possess an intriguing hierarchical structure with both micro and nano components (Figure 3.11b).

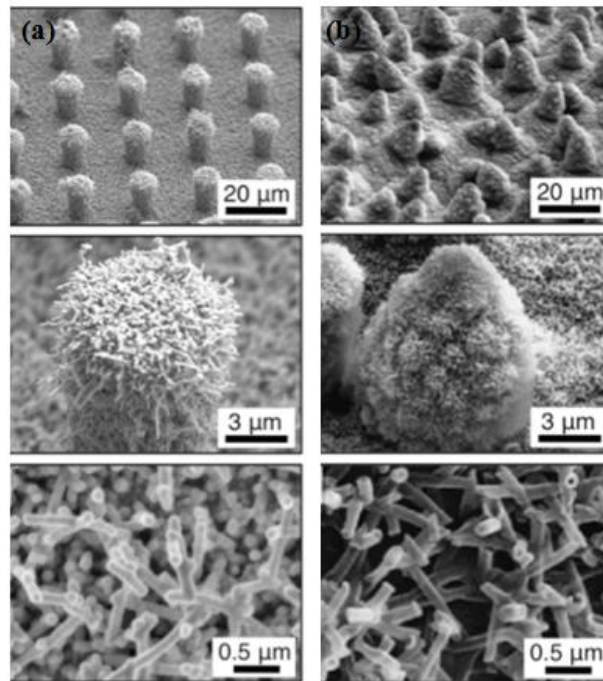


Figure 3.11: SEM images showing (a) biomimetic hierarchical microstructures of the lotus plant leaf and (b) the actual lotus plant leaf [111] (Work led by Dr. Matthew McCarthy, MIT/Drexel)

Interestingly, the TMV can be used to reproduce this structure due to the self-assembly properties of the nanotemplates on three-dimensional microstructures. For this purpose, SU-8 micropillars were fabricated using the process described previously and coated with metalized TMV template. An Al_2O_3 was deposited conformally across the substrate using ALD to facilitate subsequent deposition of a silane layer that makes the surfaces superhydrophobic. The resulting biomimetic

structures are shown in Figure 3.11a, where the resemblance to the actual lotus leaf is clearly illustrated. The significance of this biomimetic approach is that the micro and nano components can be effectively decoupled which allows independent study of the contribution of each structure to the overall superhydrophobic behavior.

3.5 Summary

The development of novel fabrication methodologies for the synthesis and patterning of nanostructured materials using the *Tobacco mosaic virus* was presented discussed in this chapter. Metal-coated as well as uncoated TMV have been lithographically patterned using a lift-off process that relies on selective photoresist and metal layer removal from a silicon substrate leaving the viruses on clearly-defined surfaces. Uncoated viruses maintain their chemical functionality after fabrication which was verified through metallization with a thin nickel layer. This fabrication approach is simple as it requires only one photolithography step and no particular surface modification. It is versatile since it can be expanded to multiple virus-templated materials while the wafer-level scalability enables integration into high-throughput manufacturing processes.

The robustness of the metal-coated TMV templates and their patterning ability has been utilized in the development of two additional processes. The assembly of the nickel coated nanostructures on three dimensional microstructures fabricated in silicon and SU-8 was demonstrated. Finally, uniform coating of patterned nickel-coated TMV structures with layers of alumina and titania using an ALD process allows the incorporation of more functional materials in this templating approach

through the formation of core/shell TMV-nickel/metal oxide heterostructures. Results from this work demonstrate an alternative route to bridging the worlds of bionanotechnology and microfabrication through the combination of top-down and bottom-up processes. These developed methods will serve as the foundation for efficient integration of templated nanostructures in the microbattery electrodes that are the main objective of this Dissertation, as well as other applications such as high sensitivity and selectivity sensor arrays, complex micro/nano structures with controlled texture surfaces as well as nanostructured catalysts for other microfabricated energy storage devices.

Chapter 4 : Nanocomposite Virus-structured Core/Shell Electrodes for Li-ion Battery Applications

The focus of this chapter is on the synthesis and electrochemical characterization of virus-structured nanocomposite electrodes for Li-ion batteries. Unlike previous work, the focus of this Dissertation has been on the Li-ion battery chemistry due to the higher energy and power density capabilities it offers compared to alkaline systems as well as the availability of several materials that can be synthesized on the viral scaffold without the problems encountered in the Master's research. The synthesis methodology that is employed is based on the process described in Chapter 4; specifically, Ni-coated TMV is assembled on a metallic current collector and the active material is deposited conformally using ALD. This method was preferred over other thin film deposition techniques due to its suitability for complex geometry coating, which will be the focus of Chapter 5. The electrode that will mainly be presented in this chapter is a Ni/TiO₂ anode, which was the first nanocomposite developed using the ALD deposition process. Key results on a Ni/V₂O₅ cathode deposited using a similar protocol with ALD will also be discussed (this work was performed in close collaboration with a post-doctoral associate in our Laboratory, Dr. Ekaterina Pomerantseva, who led the materials synthesis and characterization). In the TiO₂ anode, electrochemical results are presented on the basis of gravimetric capacity, because TiO₂ has been reported as a material that demonstrates different behavior from the bulk when in nanostructured form. The V₂O₅ cathode electrode results are presented using areal footprint normalization, indicating an increase in

energy storage capacity compared to electrodes without TMV that is in close agreement with the increase in material loading and surface area enabled by the TMV. At the end of the chapter, in order to present a complete picture on the nanostructuring capabilities on TMV, a brief mention of collaborative work performed with Professor Chunsheng Wang's group on TMV-structured Si anodes. More specifically, a brief overview of sputtering of Si on Ni-coated TMV using the conceptual approach developed in this Dissertation will be presented. This work was led by Dr. Xilin Chen (Wang group) and the author's contribution was in the sample fabrication using the sputtering technique.

The outcomes of these investigations have resulted in several archived publications. The TMV/Ni/TiO₂ results were published in *Chemical Communications* (Gerasopoulos *et al*, 2010 [112]), the TMV/Ni/Si results were published in *ACS Nano* (Chen *et al*, 2010) [113], while the TMV/Ni/V₂O₅ results are in review at the *Journal of Power Sources* (Pomerantseva *et al*, 2011).

4.1 Nanocomposite TMV/Ni/TiO₂ Anodes

As discussed in Chapter 1, nanostructured materials have emerged as very promising candidates for next generation energy storage devices. Some of the key benefits they offer compared to their bulk counterparts include reduced distances for lithium ion diffusion, structural stability, as well as larger electrode/electrolyte contact area which increases the number of reaction sites. Recently, notable research interest has been directed towards the use of biological structures as templates for the synthesis of functional surfaces for energy applications. Characteristic examples include the work by Nam *et al* and Lee *et al* who used engineered M13 bacteriophage

viruses as templates to synthesize electrodes for Li-ion batteries and the investigation by Kim *et al* who used peptides as sacrificial templates to synthesize TiO₂ nanotubes [81, 114, 115]. These biotemplated materials are then mixed in powder form with polymer binders and carbon to fabricate electrodes using traditional ink-casting techniques that are common in commercial battery devices; alternatively, they can be attached through contact-printing on current collectors [116].

In our work, an alternative methodology that combines bottom-up biological self-assembly and metallization of *Tobacco mosaic virus* (TMV) scaffolds with nanofabrication for the direct synthesis of composite core/shell Ni-coated TMV/TiO₂ anodes on current collectors is presented, following the protocol presented in Chapter 3. The unique advantage of the proposed structure lies in the self-assembly of the viral materials. Nickel-coated TMV can be directly attached onto the metal substrate, thus forming a three-dimensional current collector for the deposition of the active material and enhancing the rate performance. Consequently, the requirement for binders and other conductive additives is negated, enhancing cycling stability. This property, combined with the selective patterning capabilities of the TMV using top-down lithography which have been demonstrated in the previous chapter, create opportunities for integration of this method in large-scale manufacturing as well as microfabricated Li-ion batteries.

The anode material selected to demonstrate the concept of this approach is TiO₂. While the selection is primarily based on model system based criteria and the availability of the material using ALD at the University of Maryland, TiO₂ has attracted significant interest as a candidate anode material alternative to graphite.

Even though it has higher Li^+ insertion/deinsertion potential which reduces the energy density of the battery, lithium plating can be avoided; this results in cells with increased safety and stability [117].

4.1.1 Synthesis and Structural Characterization

The nanostructured TiO_2 electrodes were fabricated on circular stainless steel discs (15.5 mm in diameter) where a gold layer is sputtered to facilitate TMV self-assembly. Steel disks 15.5mm in diameter (Pred Materials International, USA) were coated using a table-top sputtering tool (Sputter coater 108, Ted Pella, Inc, USA) using a current of 2 mA for 50s. The nickel-coated TMV core was synthesized as described in the previous chapter. To maximize TMV assembly on the gold coated stainless steel substrate, the disks were left in the TMV-containing phosphate buffer solution for 2 days. Deposition of TiO_2 was performed in a BENEQ TFS 500 ALD reactor by alternate pulses of tetrakis-dimethyl amido titanium (TDMAT) and H_2O at 150°C following the recipe of Chapter 3. The deposition rate was slightly higher (0.055 nm/cycle) and 364 cycles ($\sim 2\text{s}/\text{cycle}$) were used to achieve the desired thickness. Finally, the electrodes were annealed in air at 450°C for 3 hours to facilitate formation of anatase phase which has been suggested as the most facile lithium ion intercalation host among the various polymorphs of TiO_2 [118]. For comparison, electrodes without TMV were also fabricated by deposition of a TiO_2 film of similar thickness directly on the steel substrate. The mass of the active materials was measured by weighing the substrates before and after ALD with a high precision microbalance and was found to be 190-260 μg for the virus-structured anodes and roughly 30 μg for the thin films.

Figure 4.1a shows an SEM image of the virus-templated nanomaterials after deposition of the TiO_2 layer on the nickel-coated TMV. The viruses attach onto the gold film from their 3' (bottom) end based on the mechanism described in detail in Chapters 2 and 3, creating a three-dimensional, high surface area nanonetwork. The non-perfect vertical alignment is due to end-to-end attachment of more than one molecule as well as fragmentation inside the solution.

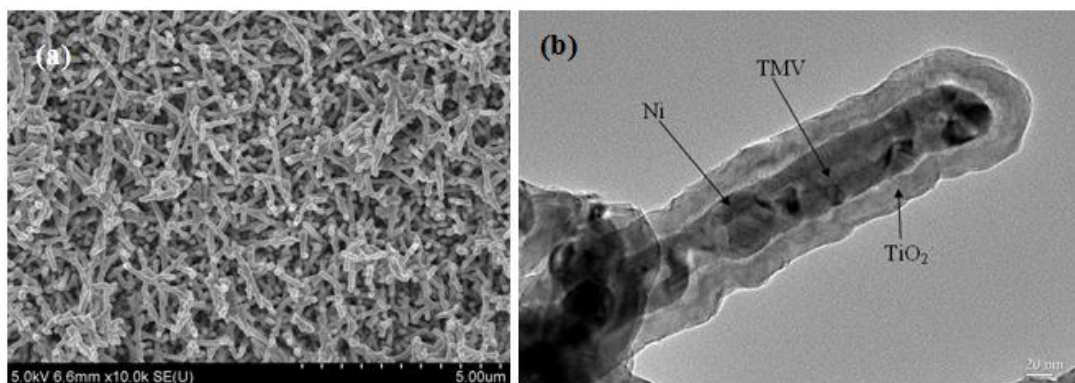


Figure 4.1: (a) SEM image of the nanocomposite anode on the current collector; (b) cross-section TEM image of a single viral nanorod showing the TMV (18nm), Ni (~20nm) and TiO_2 (~20nm)

Cross-section TEM of annealed nanowires was used to study the layer structure of the synthesized electrode. TEM samples were prepared by mechanically removing the virus nanomaterials from the steel disk and dispersing them in ethanol solution. Droplets from the suspension were pipetted onto copper TEM grids. The images shown in Figure 4.1b along with the EDS spectra in Figure 4.2 clearly illustrate the uniformity of Ni and TiO_2 coatings around the virus. It can also be observed that the thickness of the active electrode material is ~20 nm, indicating the high degree of control allowed during the ALD process.

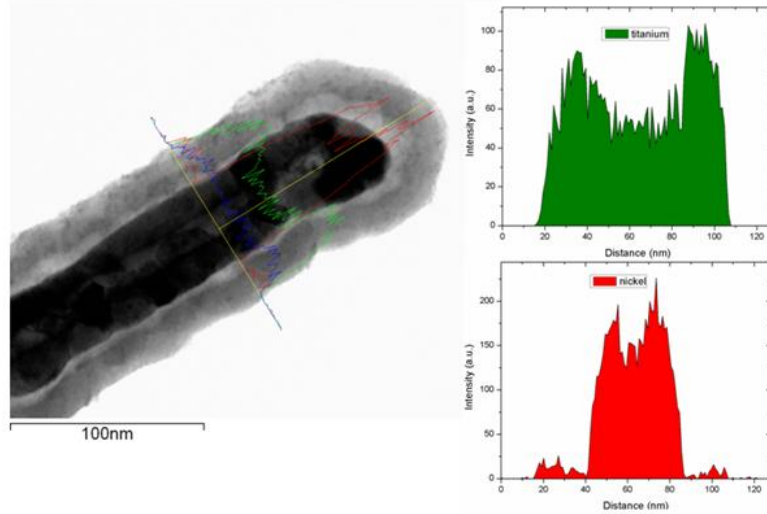


Figure 4.2: STEM image and EDS spectra of a viral nanorod electrode

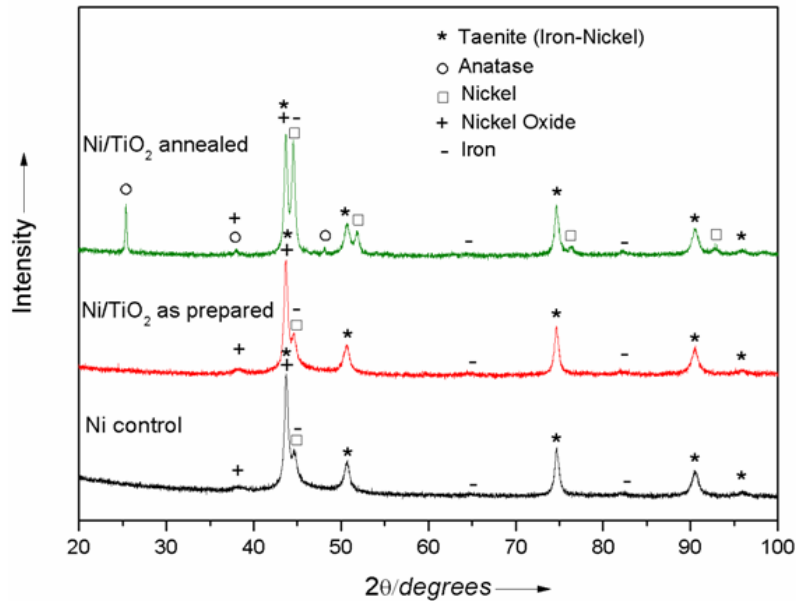


Figure 4.3: XRD data for three samples: Ni-coated TMV only, Ni/TiO₂-coated TMV (as prepared), and Ni/TiO₂-coated TMV (annealed at 450°C)

The effect of annealing the electrode was investigated using X-ray Diffraction (XRD) on as-prepared, annealed and control samples. The pattern was recorded on a Bruker D8 Advance powder diffractometer equipped with LynxEye PSD detector and Ni β-filter using CuKα radiation from sealed tube. Measurement was performed in θ/θ mode from 10 to 100° 2θ and 015777° 2θ step with total exposition of 154 sec per

point. The data obtained are shown in Figure 4.3. Peaks are identified for anatase, syn TiO_2 (JCPDS 78-2486), taenite, syn Iron-Nickel (JCPDS 47-1417), nickel, syn Ni (JCPDS 04-0850), nickel oxide, syn NiO (JCPDS 78-0643), iron, syn Fe (JCPDS 06-0696). The peaks for taenite and iron are attributed to the background signal from the stainless steel substrate, while NiO is due to partial oxidation of the TMV metallic coating layer. This data clearly shows that the anatase peaks are detected only on the annealed sample.

4.1.2 Electrochemical Characterization

The electrochemical properties of TiO_2 anodes with and without TMV coatings were studied in half-cell coin batteries. The TiO_2 anodes were used as the working electrode in the coin cells (R032) against a lithium metal foil (Sigma Aldrich, MO, USA) which was cut into a circular shape. The foil was attached to a steel surface and a Celgard separator (Celgard® 3501) was placed between the two electrodes. Five to six droplets of a 1M LiPF_6 solution in ethyl carbonate/diethylcarbonate (EC/DEC, 1:1, Novolyte Technologies, OH, USA) were used as the electrolyte. Cell assembly was performed in a glove box with oxygen concentration of less than 0.1 ppm and Argon as the carrier gas. Galvanostatic experiments were performed using a multiple channel battery test station (Arbin Instruments, TX, USA) while cyclic voltammetry and electrochemical impedance spectroscopy data were collected using a Solartron 1287A Potentiostat with frequency analyzer (Hampshire, UK). The same equipment was used to obtain the rate capability data for the electrodes without TMV, since the current required at low rates could not be accurately provided by the Arbin instrument.

Cyclic Voltammetry (CV) was used to examine the lithium intercalation/deintercalation reactions and the scans obtained at a rate of 0.5 mVs^{-1} from 2.6 V to 1 V (vs Li^+/Li). In cyclic voltammetry, the potential between the working and reference electrode is swept within a predefined voltage range, and the current that corresponds to redox reactions is measured between the working and counter electrode. The results for this test are depicted in Figure 4.4. A distinct pair of cathodic/anodic peaks centered around 1.68 V and 2.17 V respectively can be observed for both the planar TMV-modified TiO_2 electrodes, in good agreement with published literature [119]. These peaks have an approximately two orders of magnitude larger height compared to the ones for the electrode without TMV, as shown in the inset of Figure 4.4. This result may be attributed to the higher surface area of the nanostructured virus-templated anode, as well as the different electrochemical properties of bulk and nanostructured anatase [118].

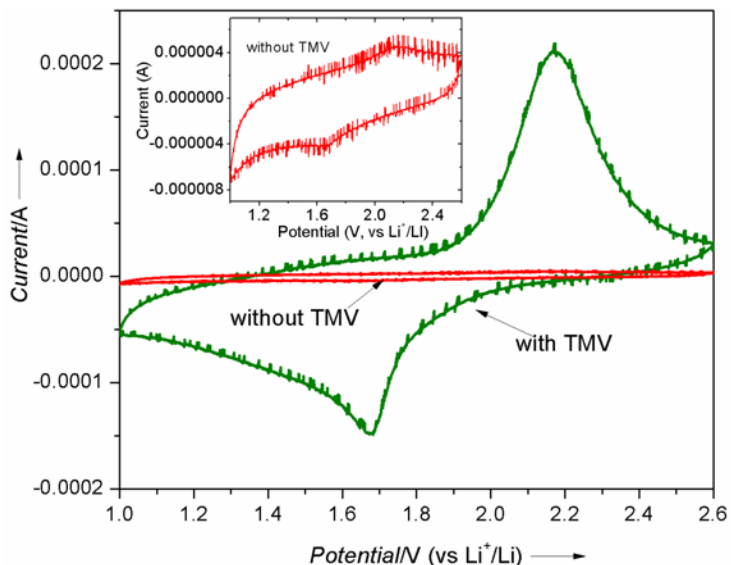


Figure 4.4: CV scans for electrodes with (green) and without (red) TMV at a rate of 0.5 mVs^{-1} ; the inset is an exploded view of the planar sample

The TiO₂ electrodes were galvanostatically cycled in the same voltage range to investigate the cycle life. In galvanostatic experiments, a constant current is applied during both the charge and discharge cycles and the voltage is measured and plotted vs. time. The cut-off limits for these tests were voltage controlled; all parameters were defined in the Arbin Instruments Battery Test Station software (MITS Pro, Schedule file). The lithium insertion in the TiO₂ can be described by the following reaction [118]: $\text{TiO}_2 + x\text{Li}^+ + e^- \leftrightarrow \text{Li}_x\text{TiO}_2$ ($x \leq 0.5$) Lithium is inserted in the titanium dioxide lattice during discharge while extraction occurs during charge. Typical charge-discharge curves for the TMV-structured anode are shown in Figure 4.5 during the 1st, 2nd and 650th cycle at a current rate of 147 mA_g⁻¹.

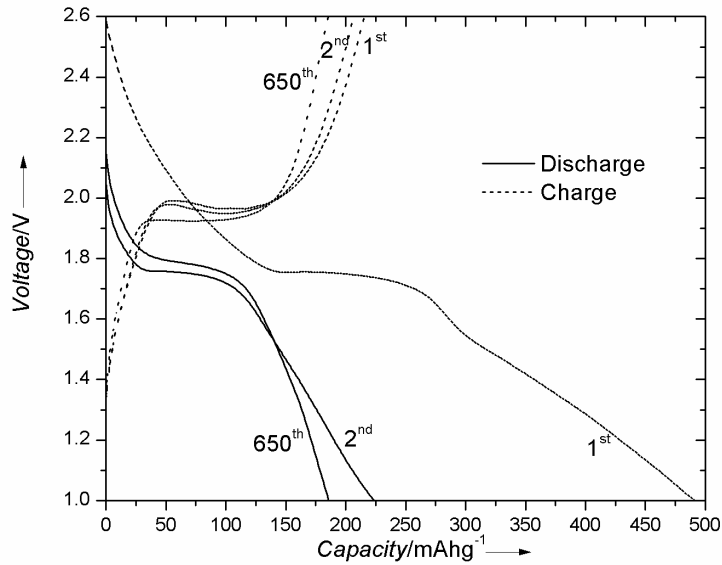


Figure 4.5: Charge/discharge curves for the virus-structured anode at a rate of 147 mA_g⁻¹ for the 1st, 2nd and 650th cycle

As expected for anatase and in accordance with the CV data of Figure 4.4, two plateaus appear during discharge and charge (around 1.75 V and 1.95 V respectively), suggesting a two-phase reaction. The discharge plateau corresponds to lithium

intercalation, while the charge plateau to lithium extraction. In this two-phase reaction, there is a transition from the tetragonal to orthorhombic phase as well as a separation into lithium rich and lithium poor domains [120]. The charge/discharge plateaus appear at lower/higher potentials compared to the CV scan due to the lower current density which results in lower overpotentials. Within the first 650 cycles of operation, the capacity drops from 223 mAhg^{-1} in the 2nd cycle to 185 mAhg^{-1} in the 650th cycle, indicating an average fading of only $\sim 0.026\%$ per cycle. In the bulk anatase structure the Li^+ insertion level x is 0.5 resulting in a theoretical capacity of $\sim 168 \text{ mAhg}^{-1}$, however higher values can be obtained when the particle size is decreased to nanometer dimensions because extra Li^+ can be stored on the film surface and in the TiO_2 grain boundary [118, 119, 121].

It should be noted that the first insertion in the TiO_2 electrodes is accompanied by a side reaction involving intercalation to the NiO that is present in the core as shown in Figure 4.6, where discharge/charge curves for a Ni-coated TMV control sample (without the TiO_2 layer) are shown along with those for the nanocomposite electrodes. The samples were cycled at the same current value and the x-axis is given in a time scale since the exact loading of the nickel-coated TMV is not known. The large irreversible capacity for the TiO_2 -containing anode in the first cycle can be attributed to this intercalation in the NiO underlying layer (see TMV/Ni curve-1st). This reaction is not fully reversible in the voltage range of 1-2.6 V [122] and results in an irreversible capacity that is observed in the first cycle for the virus-modified Ni/ TiO_2 electrodes. Since this capacity depends on the actual loading of the nickel coated TMV, it will vary from sample to sample.

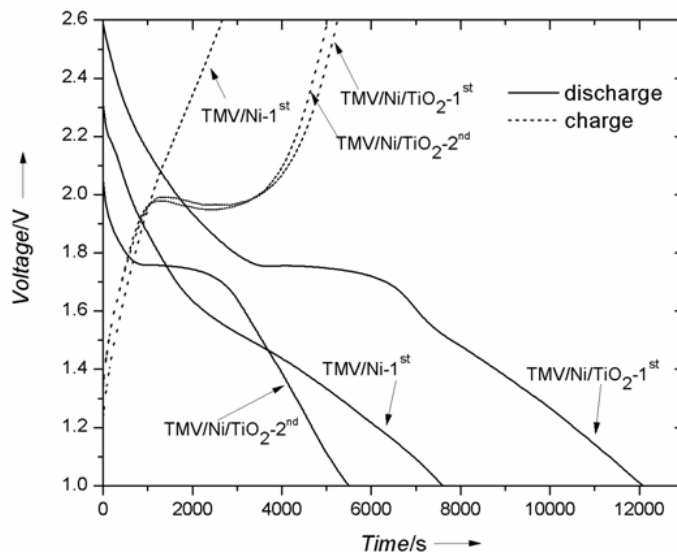


Figure 4.6: Graph showing the 1st and 2nd charge/discharge curves for the TMV/Ni/TiO₂ electrodes as well as the 1st cycle for a control sample without the TiO₂ layer (TMV/Ni)

The irreversible nature of this reaction was further verified by CV scans that were performed on the control sample and are shown in Figure 4.7. This figure indicates that there is an insertion peak for the control sample, corresponding to some NiO that is present in the core of the nanocomposite. The extraction peak is not observed for the control sample and both peaks have vanished in the second cycle.

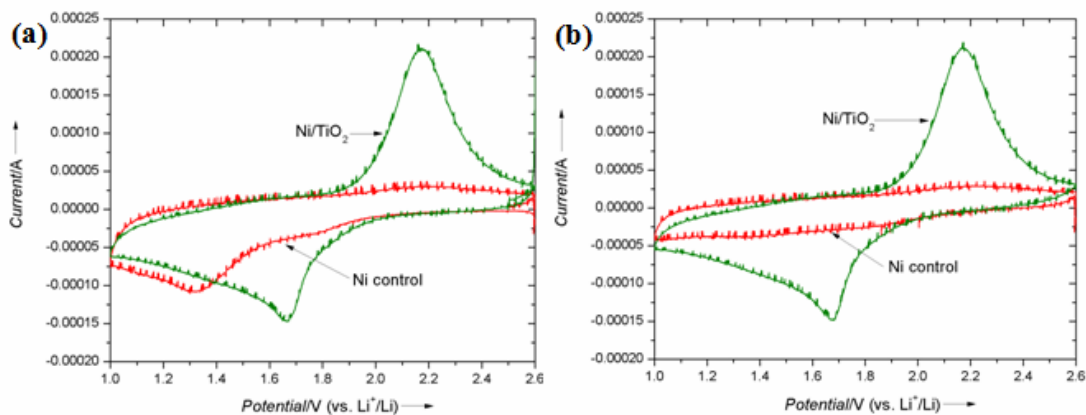


Figure 4.7: CV scans for the first (a) and second (b) cycles for the synthesized TMV/Ni/TiO₂ nanocomposite anode (green) and a control sample without the TiO₂ layer (TMV/Ni, red) obtained in the range of 1-2.6 V at a rate of 0.5 mVs⁻¹

Cycle life tests were performed at current rates of 147 mA_g⁻¹, 292 mA_g⁻¹ and 500 mA_g⁻¹ and the discharge capacity is plotted in Figure 4.8. The capacity for an anode without TMV at 147 mA_g⁻¹ is also presented for comparison. In the latter, the initial capacity is around the theoretical for a bulk film but within the first 10 cycles it quickly drops and stabilizes around 90 mA_hg⁻¹ for this rate. At the same time, the nanostructured anodes show values of 180-185 mA_hg⁻¹. As explained previously, this is attributed to the high surface area of the electrode, since extra lithium is stored at the surface and grain boundaries (further investigation of this effect involves complex electrochemical analysis which is beyond the scope of this work). As a result, the TMV-structured samples still notably outperform the planar films even at much higher currents. Due to this inferior performance, testing of the control sample was stopped after 230 cycles. In addition to the high capacity values, the stability of the electrodes is remarkable, since stable operation for several hundreds of cycles is demonstrated for all samples.

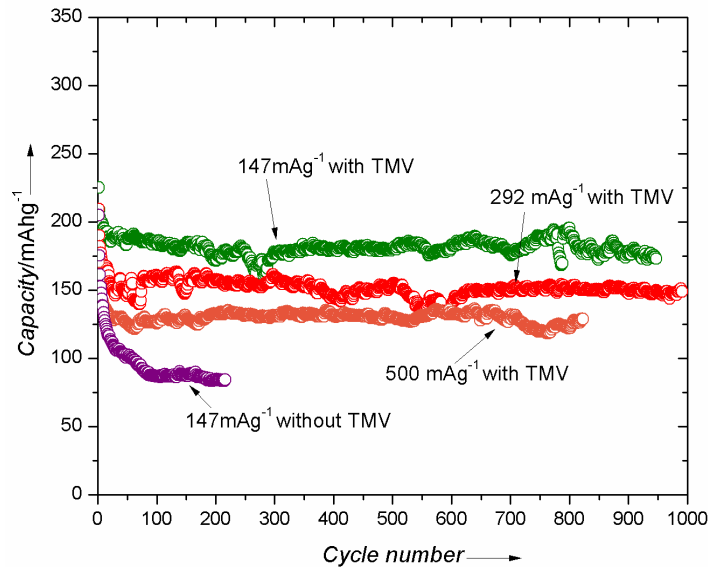


Figure 4.8: Capacity vs. cycle number for electrodes with and without TMV

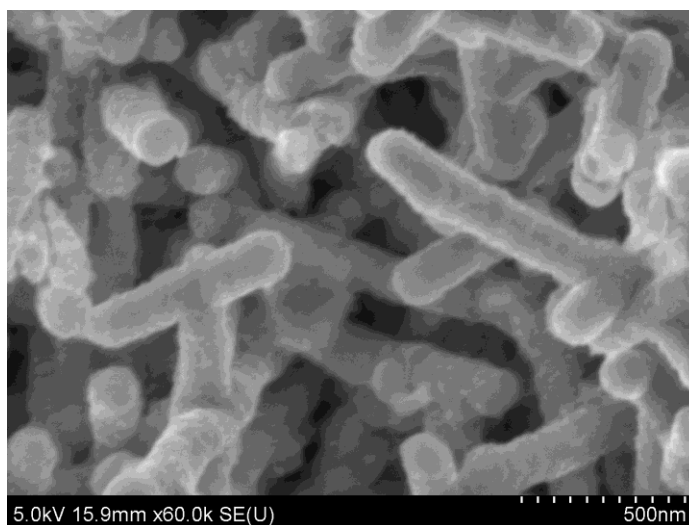


Figure 4.9: : SEM image of the nanostructured anode that was cycled at the 500 mA g^{-1} rate after completion of approximately 850 cycles

Morphology examination of the anode that was cycled at 500 mA g^{-1} after 850 cycles using SEM shows retention of the three-dimensional structure of the TMV (Figure 4.9). Before disassembly, the cell was kept at 2.6 V for 48 hours to ensure removal of all lithium from the structure and was subsequently rinsed thoroughly in propylene carbonate. It is observed that the virus nanomaterials maintain their three-

dimensional structure. These observations highlight the importance of the proposed electrode: the robust metalized TMV template, which maintains its structural integrity after rigorous cycling, and the small volume expansion of TiO_2 that enables stable and reliable cycle-life operation create a unique anode with improved electrochemical performance.

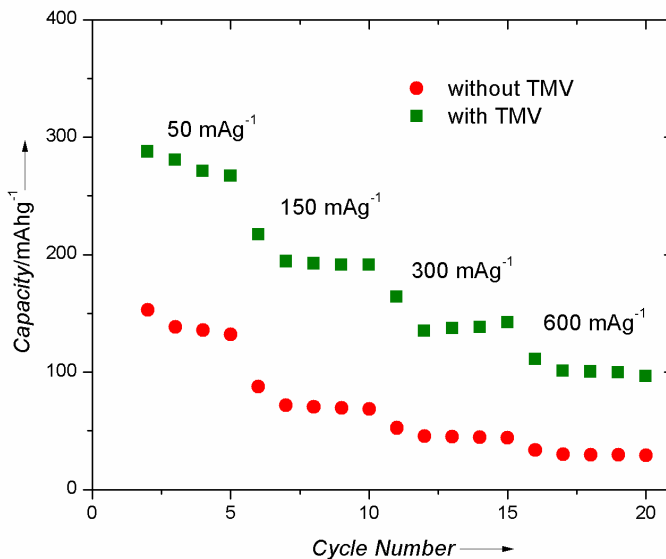


Figure 4.10: Rate capability for electrodes with and without TMV

In addition to cycling stability test, the rate performance was also investigated. In rate performance experiments, the batteries are tested at various current rates, determined from the gravimetric normalization in mA/g, to investigate the capacity retention after rapid charge discharge cycling. Specifically in this experiment, the current was varied from 50 mA g^{-1} to 600 mA g^{-1} in increments of 5 cycles. The data is plotted in Figure 4.10. The TMV-modified TiO_2 not only delivers at least two times higher capacity than regular TiO_2 film, but also provides enhanced rate capacity. At high current densities of 300 and 600 mA g^{-1} , the capacity for the virus-templated electrodes is more than three times greater compared to the thin film anode.

The high rate performance of TMV/Ni/TiO₂ is attributed to the low impedance, which was also verified in separate experiments. Specifically, the kinetics of the lithium reaction in the electrodes were investigated using Electrochemical Impedance Spectroscopy (EIS). In EIS, a small sinusoidal signal on the order 10 mV is superimposed on the DC open circuit potential of the cell. Using a frequency analyzer, the frequency of the signal is varied and the current is measured for all these values. As a result, the impedance of the cells can be estimated and the capacitive and resistive behavior of the cells can be estimated. EIS data were collected at the open circuit potential before cycling experiments at 150 mA g⁻¹ as well as after the 12th cycle when the capacity has stabilized for the TMV-coated anode. The second set of data was obtained after lithium insertion (i.e. after discharge). An AC signal of 10 mV in amplitude was applied and the frequency was swept from 1 MHz to 5 mHz.

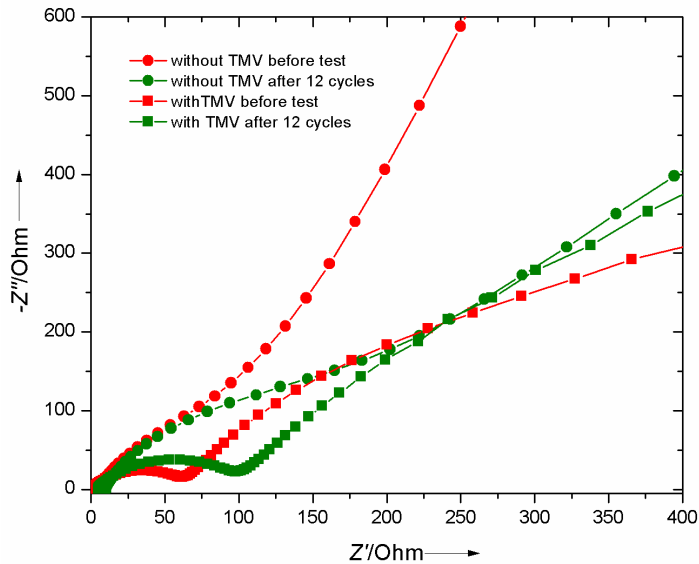


Figure 4.11: EIS data for electrodes with and without TMV cycled at 150 mA g⁻¹. The data were collected at open circuit potential before cycling and after the 12th discharge

The results of these tests are demonstrated in Figure 4.11. This Figure shows a Nyquist plot of the impedance, where the real and the negative of the imaginary parts are plotted on the x and y axes respectively. It should be noted that this method was used here to provide a qualitative analysis of the electrochemical processes rather than provide a quantitative parameter calculation. As can be seen in the figure, there is only one semicircle in the high frequency region (small Z' values) corresponding to the charge transfer resistance while the low frequency region is controlled by lithium ion diffusion. In the case of the nanostructured TiO_2 , however, the semicircle is much smaller both before testing as well as after 12 cycles, indicating a smaller charge transfer resistance in this electrode. The improved reaction kinetics enabled by the viral template provide further explanation for the superior cycling performance as well as the high rate capability.

Overall, these results show that the rigid rod structure of the TMV allows formation of self-assembled, three-dimensional nickel nanonetworks which can be attached directly onto current collectors. The viral self-assembly eliminated binders and other additives and enabled exceptional cyclic stability. Comparison with thin film electrodes demonstrated improved capabilities and reaction kinetics.

4.2 Virus-templated Ni/ V_2O_5 cathodes

Using a similar combination of electroless nickel plating and ALD on the TMV, a Ni/ V_2O_5 biotemplated cathode was developed in our Lab. In addition to its suitability as a model system for the hierarchical microbattery electrodes (unlike the case of TiO_2 , Ni is not electrochemically active in the typical V_2O_5 voltage range), V_2O_5 has great potential as a practical cathode material due to its higher capacity compared to

the typically used cathodes as well as its capability to be lithiated chemically [123]. The specifics of the V_2O_5 synthesis as well as the detailed electrochemical characterization will be given in Chapter 5, where this material is used on the three-dimensional microbattery electrodes. Here, the capacity of electrodes with and without TMV is compared and related to the increase in mass and surface area added by the viral template.

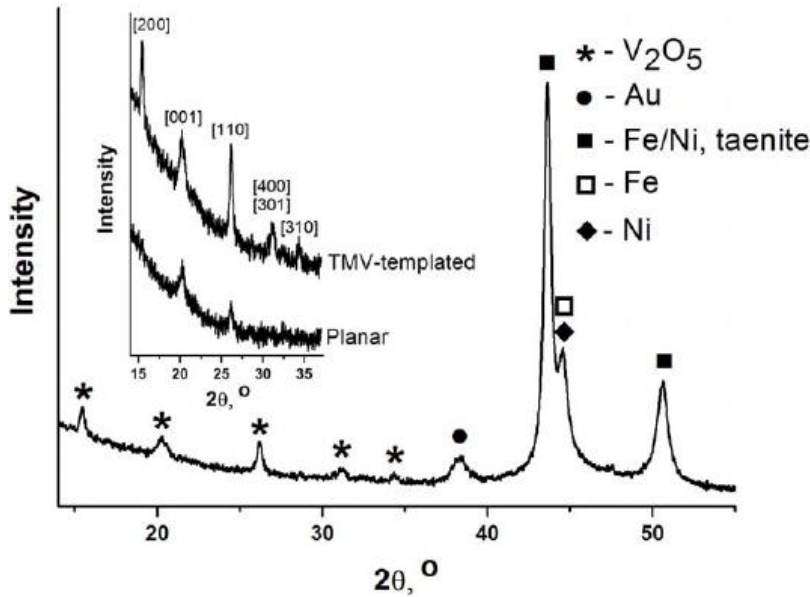


Figure 4.12: XRD patterns for flat and TMV-templated V_2O_5 electrodes on stainless steel disks

V_2O_5 was deposited using an ozone-based ALD process with vanadium triisopropoxide and ozone as the precursor and oxidizer, respectively. The target thickness for the material was 30 nm, which was achieved through 1000 ALD cycles. Using this process, crystalline V_2O_5 can be deposited, as analyzed elsewhere [49]. Figure 4.12 shows corresponding XRD patterns from the synthesized electrodes. The V_2O_5 film crystallizes in the orthorhombic cell (JSPDS N0. 41-1426) and exhibits a preferential orientation in c-axis, as evident from the intensity of the (001) peak of the planar film (inset). Interestingly additional peaks appear for the TMV templated

samples, which can be attributed to the three-dimensional morphology of the surface. As in the case of TiO_2 , background signals from the stainless steel disk and nickel are also recorded.

Figure 4.13 shows a cross-section TEM (samples prepared similarly) and the corresponding EDS signals, indicating again the conformality and thickness control enabled by ALD. Samples with and without TMV were prepared on Au-coated stainless steel disks. The electrode masses were measured before and after ALD deposition. Based on these measurements, the average V_2O_5 mass on the TMV-templated samples was $\sim 160 \mu\text{g}$ (ranging from 140 to 180 μg) while that on the planar electrodes was $\sim 27 \mu\text{g}$ (ranging from 24 to 31 μg). The variation is attributed to the difference in TMV coverage from sample to sample. This six to almost eight fold increase in mass is a result of the increase in surface area added by the TMV.

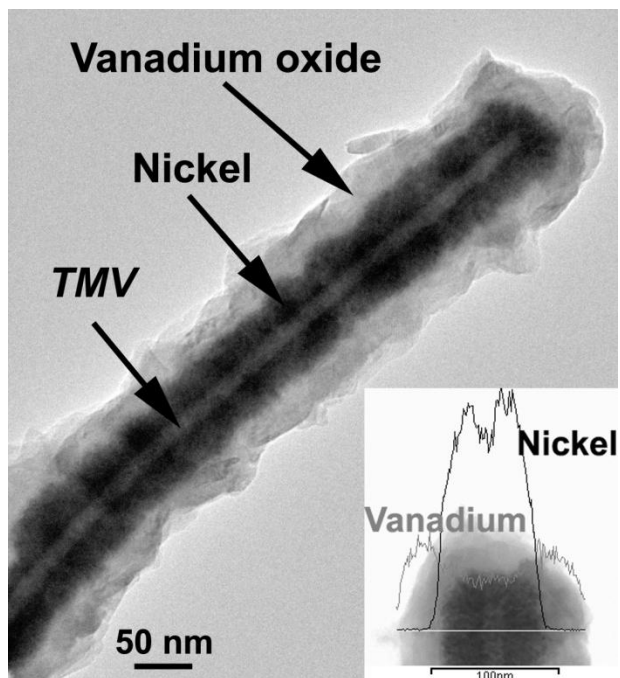


Figure 4.13: Cross-section TEM and EDS signals showing the uniform coverage of the V_2O_5 on the nickel-coated TMV template; the thickness is $\sim 30 \text{ nm}$ [124]

Since the lithiation process in bulk and nanostructured V_2O_5 is similar, gravimetrically the capacities for these two types of electrodes was expected (and experimentally verified) to be similar as well, regardless of the electrode surface area as in the case of TiO_2 . However, the importance of the TMV template is that it can increase the surface area, which in turn increases the active material mass loading and hence the energy density for the same footprint. Consequently, in these experiments, electrodes were tested at the same areal current densities and the capacities were normalized per areal footprint. A characteristic result for electrodes with and without TMV is shown in Figure 4.14. The capacity for the TMV-templated electrode is $\sim 12 \mu Ah/cm^2$ while that for the flat electrode is $\sim 1.5 \mu Ah/cm^2$ at a $5 \mu A/cm^2$ current density. This roughly 8-fold increase in capacity is consistent with the range of increase in material mass, showing the benefit of using high surface nanostructures.

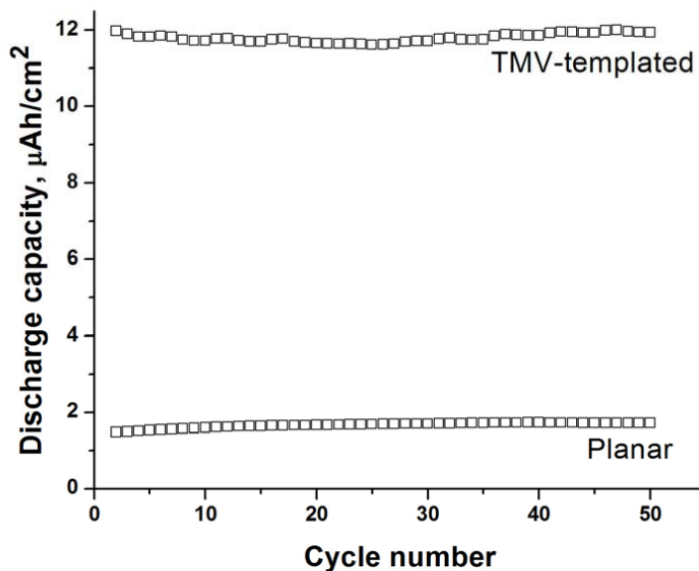


Figure 4.14: Capacity vs. cycle number for TMV/Ni/ V_2O_5 electrodes with and without TMV [124]

4.3 Virus-structured TMV/Ni/Si Anodes

For completion regarding the electrodes developed on the Ni-coated TMV biotemplate, a brief review of the TMV/Ni/Si anodes will be presented. The deposition method selected for this electrode was sputtering, due to the lack of another suitable method. Silicon was sputtered in an AJA sputtering system (AJA international, Inc.) on a Ni-coated TMV steel disk. The process was performed in RF mode with a power of 200 W, an argon gas flow of 20 sccm, and a chamber pressure of 5 mTorr. The distance between the silicon target and the virus-coated steel disk substrates was set to approximately 110 mm, and the chuck was rotated to achieve better uniformity. The deposition time was 45 min, resulting in ~ 50 nm thickness and an approximately 50 μg of mass loading on the electrode surface.

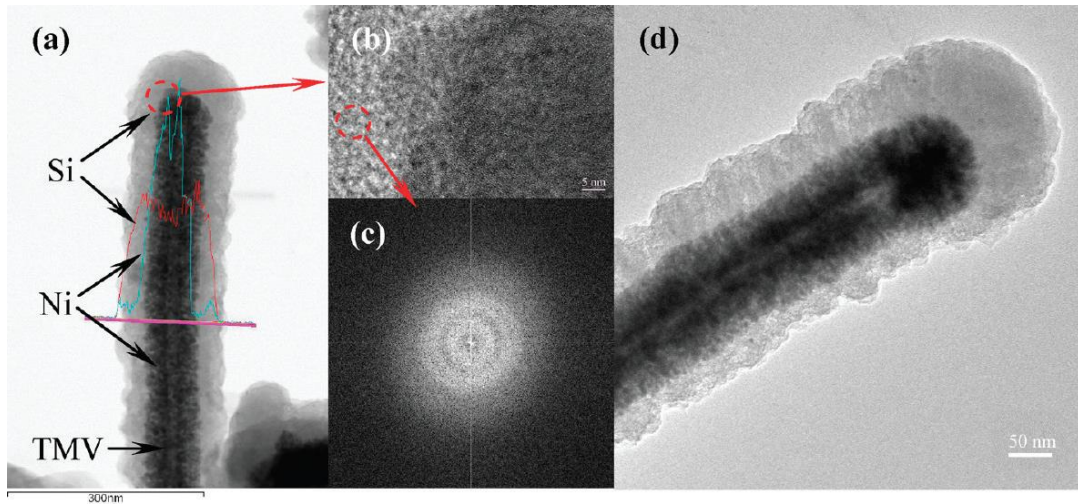


Figure 4.15: (a) TEM image of a vertically aligned TMV/Ni/Si nanoparticle after 45 min of silicon sputtering, including EDS profiles of the different films, (b) high resolution TEM image of the circled area in (a), (c) FFT signal of the circled area in (b), (d) TEM image of non-vertically aligned TMV nanorod [113]

Figure 4.15a shows a TEM image of a vertically aligned TMV/Ni/Si nanorod. The deposited layer for such particle orientation is very uniform. Figures 4.15b and 4.15c

show that the deposited layer is amorphous. Figure 4.15d shows a TEM image of a non-vertically aligned TMV particle, where the non-uniform coverage of the active material is clearly illustrated. This is a disadvantage of physical vapor deposition methods compared to ALD, which makes them non-ideal particularly for three-dimensional electrodes. Regardless of this processing limitation, the electrodes demonstrated excellent electrochemical behavior, achieving very high capacity values as well as ~100 % charge/discharge (coulombic) efficiency (Figure 4.16) with very good mechanical stability. In bulk or micron-sized silicon electrodes, this is the major problem since the silicon lattice expands up to 300% to accommodate lithium intercalation, which often results in particle pulverization and very rapid capacity loss [113]. Using the TMV templated methodology, the behavior of the silicon anodes was significantly improved.

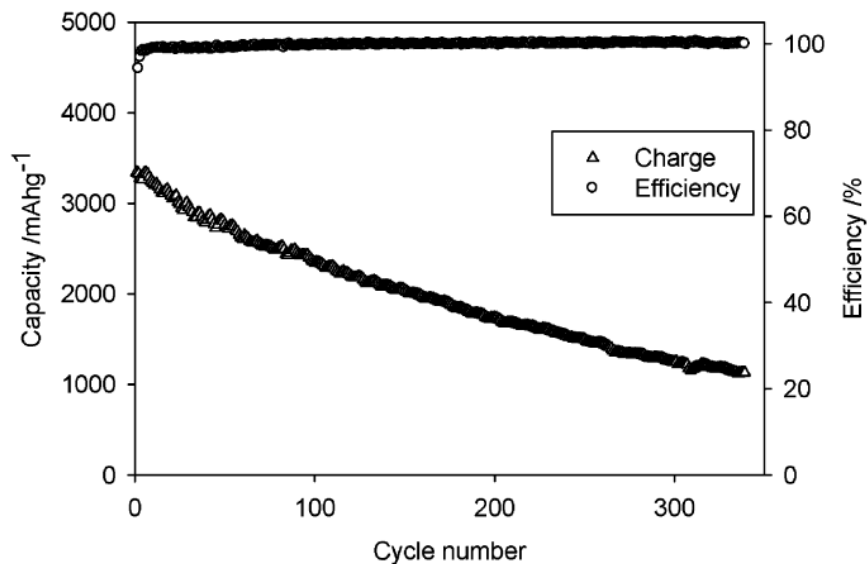


Figure 4.16: Capacity vs. cycle number and coulombic efficiency vs. cycle number for a TMV templated Si anode at 2A/g [113]

4.4 Summary

This chapter presented the different electrodes developed using the TMV biotemplating method that combines the bottom-up self assembly of the particles, electroless plating to form a conductive three-dimensional current collector and a thin-film deposition technique to deposit the active battery material. More specifically, Ni/TiO₂, and Ni/V₂O₅ anodes and cathodes were presented, both showing superior performance compared to planar thin film electrodes. Similarly, Ni/Si anodes alleviate the major problem involved in silicon cracking and capacity loss, leveraging on the three-dimensional morphology of the TMV nanonetwork. The primary benefit of this approach is that there is no requirement for binders or other conductive additives used in commercial electrodes; at the same time, when combined with the biofabrication processes demonstrated in the previous chapter, these electrodes hold great promise for next-generation microbattery electrodes.

Chapter 5 : Three-dimensional, Hierarchical Microbattery

Electrodes Using the TMV

Chapters 3 and 4 discussed the main TMV-based fabrication processes for device-level integration of the biotemplates as well as the synthesis of core/shell nanocomposite electrodes with superior electrochemical performance. This chapter presents the development of three-dimensional microbattery electrodes that combine the processes described previously. More specifically, the electrodes consist of three-dimensional gold micropillars fabricated using electroplating through thick photoresist molds. These structures serve both as current collectors as well as the base for the TMV self-assembly and metallization. Finally, ALD is used to conformally deposit the active battery material following the procedures presented in Chapter 4. The electrodes were electrochemically characterized and compared to control samples with nanostructures only. Interestingly, the energy density for the hierarchical electrodes (with both micro and nano structures) is consistently three times higher compared to that from TMV-templated only electrodes. This is in very good agreement with the increase in surface area and mass loading added by the gold micropillars, demonstrating the suitability of the two key conformal processes; the TMV-self assembly and the atomic layer deposition of the active material. At the same time, the higher energy density is retained at various current densities and rates, verifying the merit of this approach in increasing the energy density in a controlled manner while maintaining the advantages of nanostructured materials.

5.1 Design Considerations

The general design for the hierarchical electrodes is based on micropillar arrays which are coated uniformly with the virus-structured nanomaterials. The conceptual approach is similar to that presented in Chapter 3. The hierarchical electrode design adopted in this work is based on the use of micropillars as substrates for the assembly of the nanostructured active materials, rather than pores formed in silicon, as shown by other research groups [46]. The major requirement when pores in silicon are used is the electrochemical isolation of the structural bulk silicon which dictates the use of a barrier layer between the current collector and silicon. Previously, TiN has served as both the barrier layer and the conductive substrate [45]. While this is an efficient electrochemical barrier, it is generally limited to low current densities due to inferior conductivity compared to conventional current collectors. In addition to this limitation, in our work, due to poor attachment of the TMV on TiN as well as the inefficient combinations of available barrier/current collector films that could ensure both proper electrochemical operation and TMV attachment, micropillars were selected to form highly conductive 3D current collectors as well as facilitate very uniform viral self-assembly. Gold was selected as the material of choice for the micropillars due to the excellent TMV attachment properties as well as its electrochemical inertness in the voltage range of interest.

The cylindrical micropillar geometry was selected over other geometries (for example, trench, pores, or parallel plate arrays) based on key findings from that work. More specifically, it was experimentally observed that coating uniformity was better in pillar geometries probably due to more efficient concentration gradients for

reactants (TMV solution and electroless plating bath constituents) to diffuse to the structures.

The micropillars are fabricated through thick photoresist molds. As presented in Chapter 1, silicon molds have been used in the literature for electroplating of three-dimensional microstructures with very high aspect ratios. However, the fabrication process (particularly the substrate attachment and mold release) is more complex compared to a thick photoresist; hence the latter approach was selected for the first prototype hierarchical electrode development in this Dissertation. This choice of molding technique consequently affected the geometry of the microstructures since there are limitations in the aspect ratio that can be achieved in thick photoresist processes. Two photoresists were initially examined: KMPR 1000, a negative photoresist from Microchem Corporation, and AZ 9260, a positive resist from AZ Electronic Materials. Based on literature data and consultation with the manufacturers, reliable aspect ratios on the order of 6:1 and 3:1 to 4:1 can be obtained for KMPR and AZ9260, respectively [125]. As a result, optical photomasks were designed with circular openings having a diameter of 20 μm and a center to center spacing of 40 μm as the primary geometry. Using these dimensions and aiming at photoresist thicknesses ranging between 60 and 100 μm , the micropillars can be fabricated within the acceptable aspect ratios. As will be explained later in the chapter when the equation for surface area increase is given, the key parameter of interest is the aspect ratio of the electrodes. This implies that smaller diameters and spacings could be designed, combined with thinner photoresist thickness. However, as the hole diameter decreases limits of the contact mask aligner are reached so a safer approach

was adopted for the first demonstration. In all photomask variations, the micropillars occupied a footprint of 1 cm^2 , which could enable normalization and comparison with electrodes without 3D microstructures.

5.2 Device Fabrication

5.2.1 General Fabrication Scheme

The general fabrication scheme for the hierarchical electrodes is shown in Figure 5.1 below:

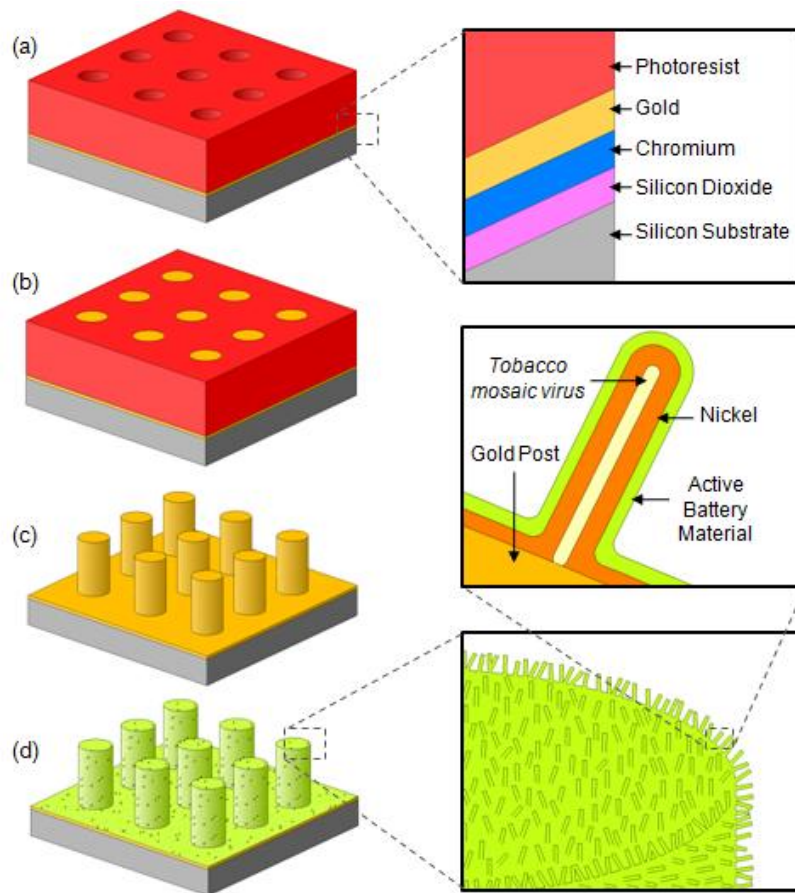


Figure 5.1: General 3-D electrode fabrication process;(a) mold patterning, (b) electroplating, (c) mold dissolution, (d) TMV self-assembly, metallization, and ALD of active material

The fabrication process begins with the thick photoresist patterning on a silicon wafer which has been coated with the electroplating seed layer (gold with a chrome adhesion layer). Depending on the type of photoresist used, one or multiple spin processes are performed to achieve the desired thickness. Following photoresist development, the wafers are descummed using O₂ plasma to remove any residues and gold electroplating is performed to form the micropillars inside the mold. The mold is then dissolved in an appropriate solvent and individual chips are coated with the TMV template. Finally, after TMV metallization, the active material is deposited using atomic layer deposition. The following subsections present these processes in more detail.

5.2.2 Mold Fabrication with KMPR

Due to the capabilities for higher aspect ratios, KMPR was the first photoresist process explored for the mold fabrication in this work. The process was developed based on the data sheet provided by the manufacturer. Layers of Cr (20 nm) and Au (250 nm) were deposited on silicon wafers where a SiO₂ film (~300 nm) was thermally grown. This layer is used primarily for electrochemical isolation of the substrate when TiO₂ was used as the active material. Following current collector and seed layer deposition, the wafers were cleaned in a typical AMI process (Acetone, Methanol, Isopropyl alcohol) and dehydrated on a hotplate at 150°C for 10-15 minutes. Before photoresist spinning, the wafers were pre-treated with a thin film of adhesion promoter which was spun at 3000 rpm for 30 s. The target thickness of ~ 80 μm was achieved using either a one or two spin process. For the one spin process, the final spin speed was set at 1500 rpm, while for the two spin process, the speed was 2300

rpm. For either process, a spread cycle of 600 rpm for 10 s was used to uniformly spread the photoresist across the wafer, followed by the final spin speed. A ramp of 300 rpm/s was used between the spread and final spin speeds. After spinning, the wafers were placed on a hotplate at 100°C for the soft-baking step. The time was set at 26 minutes for the one-spin process; for the two-spin process, 20 minutes for the 1st soft-bake and 30 minutes for the second soft-bake, since some solvent might still be trapped at the interface. The temperature was slowly ramped to the final value (300°C/h) to avoid any thermal stress build-up. Similarly, after completion of the soft-bake, the wafers were also allowed to cool down to room temperature by switching off the hot plate. Once the wafers have been properly cooled down, they were exposed with UV light using a dose of 2350 mJ/cm² at 405 nm. The dose was adjusted from the manufacturer data sheet to account for the gold substrate. After exposure, a second bake at 100°C was performed using a similar ramping scheme for 5 minutes. The wafers were again cooled down to room temperature and then developed using SU-8 developer for approximately 10 minutes. In this step, optical inspection under microscope was used to ensure clearing of the holes. Using this process, molds with thickness on the order of 80 μm could be fabricated.

There are two main limitations involved in the KMPR fabrication processes that prevented its routine use for the hierarchical electrode fabrication. The first is related to the polarity of the photoresist and the requirement for very small thickness variation. When the photoresist is not fully uniform across the entire surface of the wafer, the optical mask is not in direct contact with the underlying polymer in the entire exposed area. As a result, given that KMPR is a negative tone photoresist, light

can leak and scatter in these non-contact points and cross-link areas of the photoresist that should be developed away in the developer. This is illustrated very clearly in Figure 5.2 which shows a cross-section SEM image of a non-uniformly spin KMPR layer; it is observed that the holes in the photoresist that lies below the top surface are not developed properly. This nature of the exposure and development process posed a very stringent limitation in the uniformity of the photoresist layer.

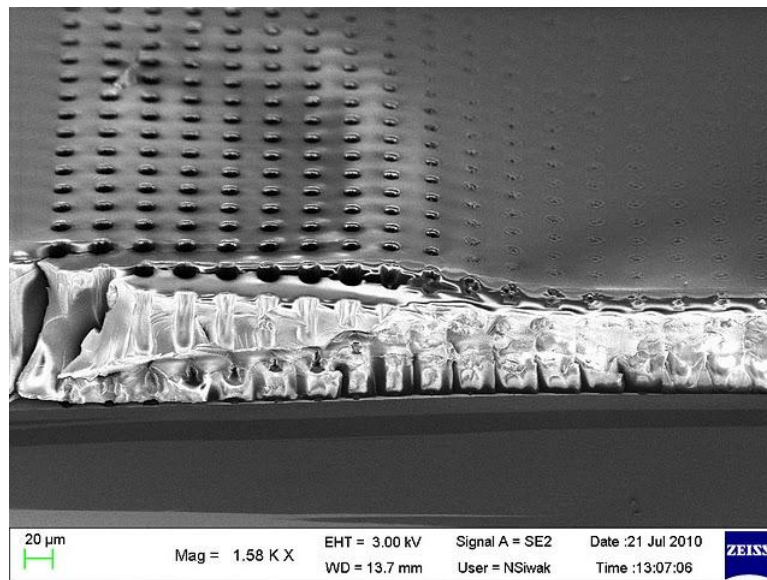


Figure 5.2: SEM image showing the impact of non-uniform KMPR spin on the hole development

While this problem could be compensated for by adjusting the spin parameters and soft-baking times and ramp, the primary limitation involved in the KMPR fabrication was the difficulty in dissolving the mold after fabrication. The electroplating details will be given in a following subsection; here, the mold removal issues after electroplating are briefly discussed. The manufacturer recommends immersion of the substrates in specialized solvent, Remover PG, whose main constituent is the solvent NMP (N-Methylpyrrolidone). The recommended process temperature is 80°C and the time varies based on the thickness of the resist. This

procedure was followed using multiple variations such as stirring, agitation, ultrasonication, overnight immersion, with only partially successful results; more specifically, residues remained on the substrate that were not removed even after prolonged treatment with O₂ plasma, which is known to remove polymers (Figure 5.3). The results did not improve significantly even when more specialized kits suggested by the manufacturer were used. It became apparent that significant attention would have to be directed towards optimizing photoresist removal parameters, which was beyond the scope of the project, particularly since positive photoresists allow for easier fabrication processes.

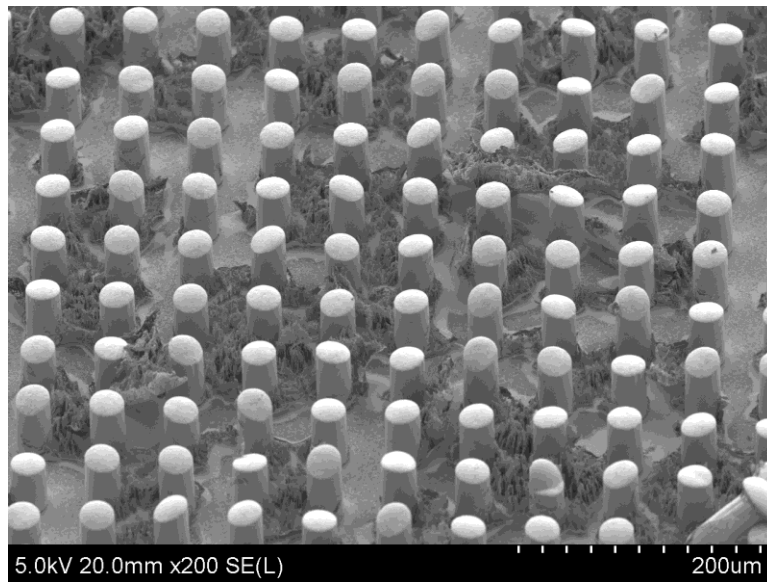


Figure 5.3: Characteristic SEM of attempt in KMPR mold removal after 1 hour treatment in Remover PG and O₂ plasma showing residues remaining across the wafer

5.2.3 Mold Fabrication with AZ 9260

Positive photoresists can alleviate the limitations discussed in the previous subsection. Any possible non-uniformity of the spun layer does not result in ineffective clearance of the holes, since in positive resists areas exposed to light are developed

away. In addition, removal of positive photoresists is a simple procedure that can be achieved using acetone bath treatment. The disadvantage of positive resists compared to negative for this application is the highest aspect ratio that can be fabricated. Based on literature reports, multiple spin processes can be used to give thicknesses up to 80 μm with aspect ratios between 3:1 and 4:1. Such a process was modified in the current work to produce micropillars with a target aspect ratio of 3:1.

The seed layer was deposited onto the wafer as described above. The electroplating mold was fabricated using a 3-spin process in positive AZ9260 photoresist. First, hexamethyldisilazane (HMDS) was spun at 3000 rpm for 30 s on the wafer as adhesion promoter. The first AZ9260 layer was spun at 1000 rpm for 40 s, followed by 105 s of soft-baking at 110°C. Similarly, the second and third layers were spun at 1000 rpm for 50 s and 800 rpm for 60 s and soft-baked at the same temperature for 160 s and 300 s, respectively. For every spin step, a spread cycle at 300 rpm for 10 s was used. In between each spin, edge bead removal was performed with EBR solvent. The solvent was dispensed using a pipette around the wafer edge while the wafer was spinning at 400 rpm for 10 s. After completion of this time, the wafer was spun at 800 rpm. Following the 3-spin process, the wafer was allowed to rehydrate overnight; this is important for such thick photoresists since adequate traces of water are required for successful completion of the process. The wafers were then exposed using UV light with a dose of 2400 mJ/cm^2 at 405 nm. Finally, the resist was developed in a AZ400K:DI water 1:4 mixture for 10 minutes. Figure 5.4 shows a cross-section SEM image of the resulting mold. The thickness of the photoresist is approximately 60 to 65 μm , as expected from the three-spin process. Interestingly, it

can be seen that the diameter of the pillars varies from top to down, being slightly enlarged on the top. This is attributed to the thickness of the photoresist and the imbalance between the exposure dose and development rate at the top and bottom of the mold [125].

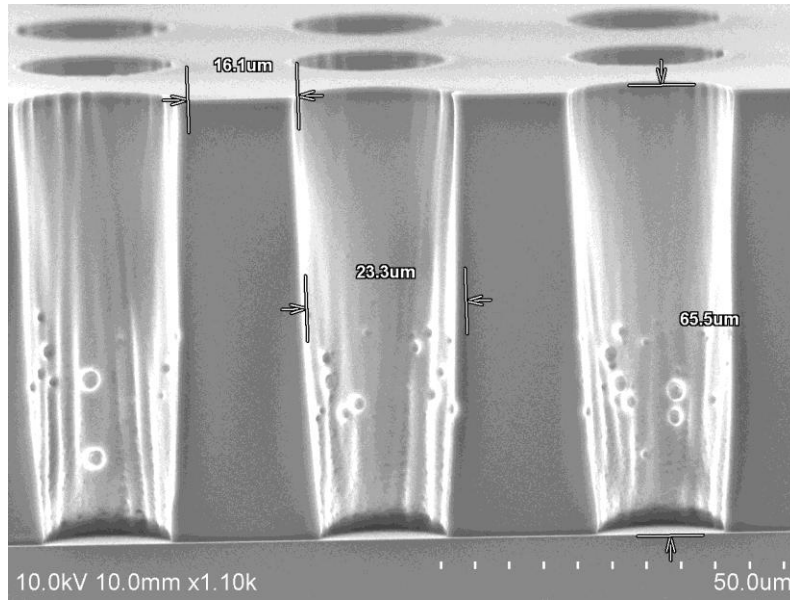


Figure 5.4: Cross section SEM image showing the photoresist mold fabricated with the AZ 9260 process

5.2.3 Gold Electroplating

After lithography, the wafers were treated with O₂ plasma at 75 W for 60 s to clear any residues from the holes. Determination of the proper parameters for this process is very critical. If the time and power are too little, residues might not be completely removed; on the other hand, excessive plasma treatment may result in gold splattering off the seed layers and onto the sidewalls of the mold. This prevents proper bottom-up electroplating as the gold that is re-deposited on the sidewalls acts as a seed layer as well and gold deposits on the walls much faster, forming hollow posts, as experimentally observed in practice.

Before electroplating, an additional treatment with 5% H_2SO_4 was performed to improve the hydrophilicity of the holes, as suggested in literature [125]. The electrolyte selected in this work was gold-sulfite solution at pH 7 purchased from Transene Company (TSG-250). This bath was preferred over cyanide-based solutions due to the reduced safety hazards. The neutral pH is also compatible with the thick photoresist process. The electroplating set-up is shown in Figure 5.5. It consists of a propylene tank with a propylene rod used to support the working and counter electrodes. The wafer to be plated was the cathode, while a niobium-clad platinum mesh (4 inch square) was used as the anode. The distance between the two electrodes was kept at 3 cm for consistency, using the adjustable holders. The whole tank was placed on a hotplate which provided mechanical agitation through a magnetic bar, while the temperature was at 50°C to ensure a bath temperature of 30°C .

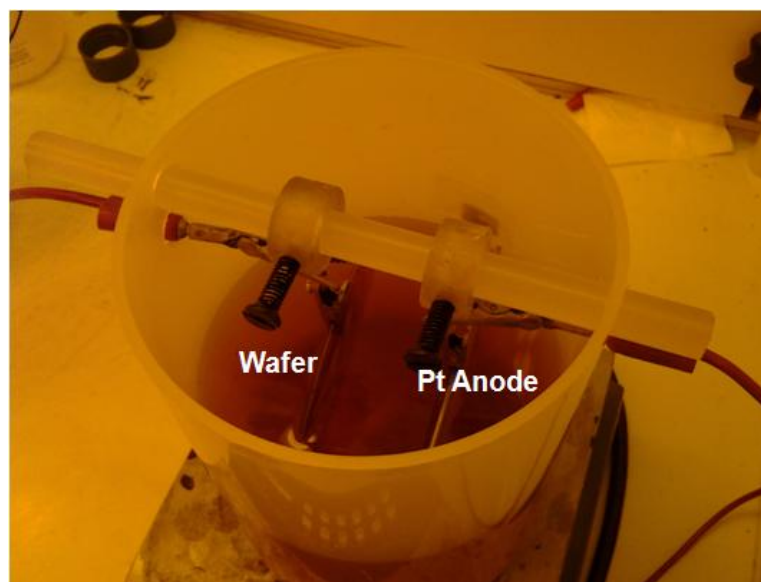


Figure 5.5: Optical image of the electroplating set up showing the tank on the hot plate and with the wafer and counter electrode marked

Electroplating was done at constant current densities based on previous work where the same plating bath was used and the deposition rate was calculated for different current densities [126]. The current densities selected were 2 mA/cm^2 and 4 mA/cm^2 for 2.5 h and 6.5 h, respectively. The lower current density was chosen to ensure that the plating begins without any voids; then it was increased to a higher value to facilitate faster electroplating. Overall, an average rate $6\text{-}7 \text{ }\mu\text{m/hour}$ was calculated. An optical image of micropillars electroplated through the photoresist mold is shown in Figure 5.6a. After electrodeposition, the wafers are diced in individual chips and then immersed in an acetone bath. This results in quick dissolution of the photoresist layer, leaving the micropillars on the gold-coated silicon substrate. Figure 5.6b shows an SEM image of the micropillars after mold removal.

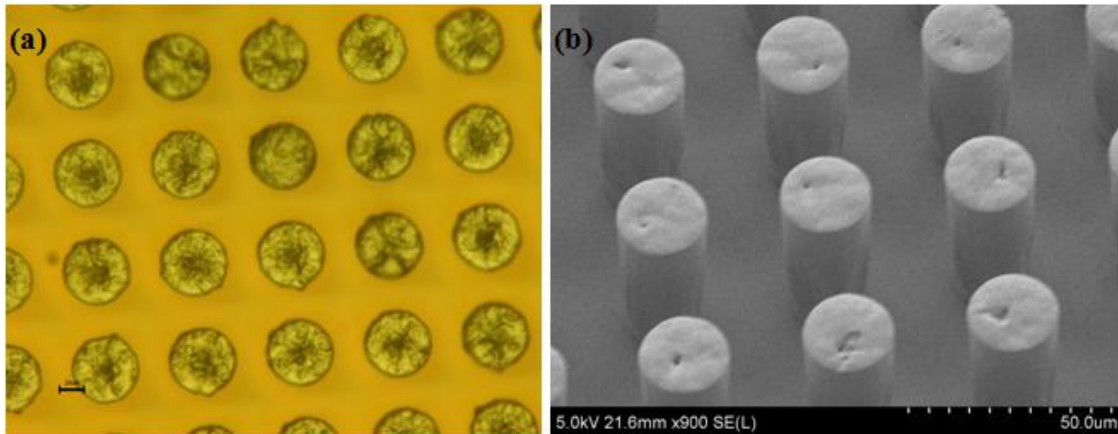


Figure 5.6: (a) optical image showing the top of electroplated micropillars through the photoresist mold, (b) SEM image of the gold micropillars after photoresist removal

5.2.4 TMV Nanostructure Assembly and Active Material Deposition

The next steps in the hierarchical electrode fabrication involve the TMV assembly on the micropillars as well as the deposition of the active material using ALD.

Overall, the process is similar to that described in Chapter 3. Some adjustments were made to ensure conformal deposition of the TMV in the pillar geometry, since diffusion of TMV particles may be a limiting factor in these dense structures. The samples were immersed in a TMV solution at a concentration of 0.2 g/L and agitated on a rocking platform during an overnight step. Next, they were immersed in a 0.1 g/L solution and left stagnant on the bench. This was done based on the findings presented in Chapter 3, where agitation resulted in partial removal of the TMV from the sidewalls. The Pd catalyst solution was left overnight, while nickel coating was performed with manual agitation to ensure the reactants reach all the crevices.

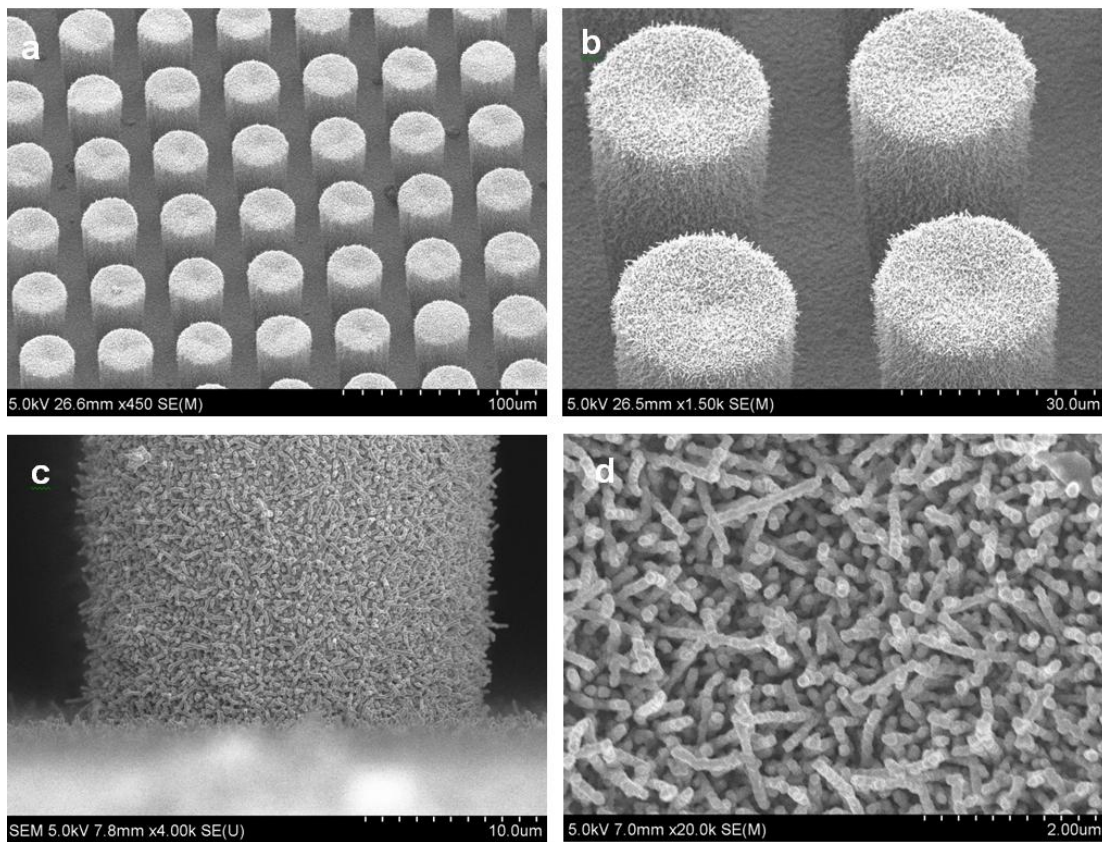


Figure 5.7: (a) Orthogonal view of a hierarchical electrode, (b) close up view of four micropillars shown in (a), (c) image showing the bottom of a micropillar, (d) close up view of the top of a micropillar

Figure 5.7 shows SEM images of hierarchical electrodes with V_2O_5 deposited as the active material. The orthogonal and side views of the micropillars show the excellent uniformity of the TMV coating across the entire surface and highlight the importance of the viral self-assembly. Figure 5.7d is a close-up view of the top of one micropillar, indicating the high porosity of the electrode.

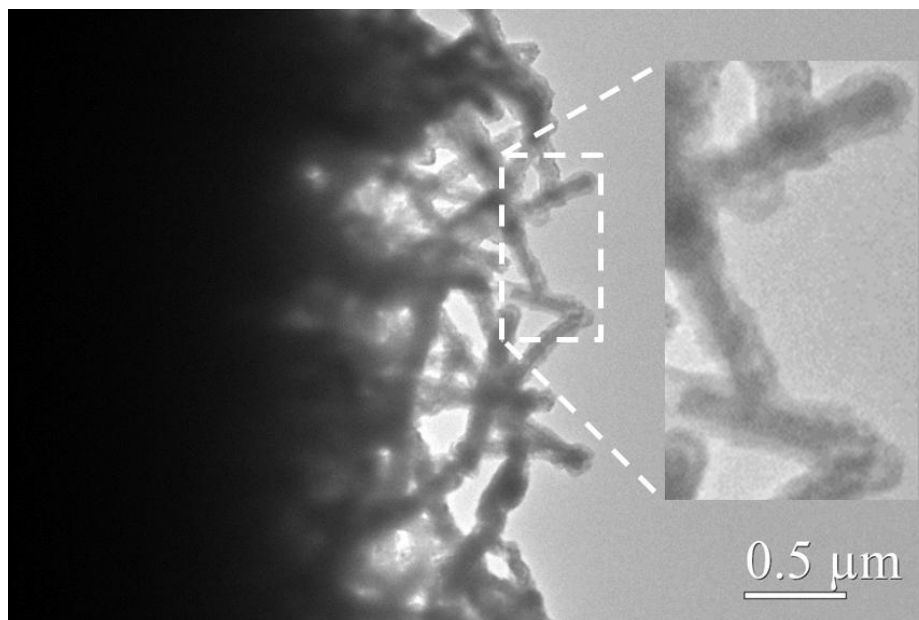


Figure 5.8: TEM image taken from the sidewall of a micropillar showing the uniform V_2O_5 coating across the entire geometry, regardless of the particle orientation

TEM images of the nanostructured TMV-templated core/shell electrodes were presented in Chapter 4, showing the uniformity of the ALD coating around the metalized viral particles. In addition to individual nanorods, TEM images were taken from the sidewalls of micropillars that were mechanically removed from the silicon substrate and dispersed onto TEM grids. Figure 5.8 shows the electrode nanostructure at the sidewall of the pillar, and it can be observed that the V_2O_5 coating is uniform regardless of the orientation of the particle. This is a very significant attribute of

ALD, which is ideally suited to create uniform, conformal coatings with precise control over film thickness.

In addition to hierarchical samples, control samples containing TMV nanostructures only on silicon wafers were also fabricated (i.e. without Au micropillars). The control samples were made with the typical process that was presented in the previous chapters, without the two overnight steps used for the micropillars. For flat substrates it was found that this process does not make any significant difference in the amount of material.

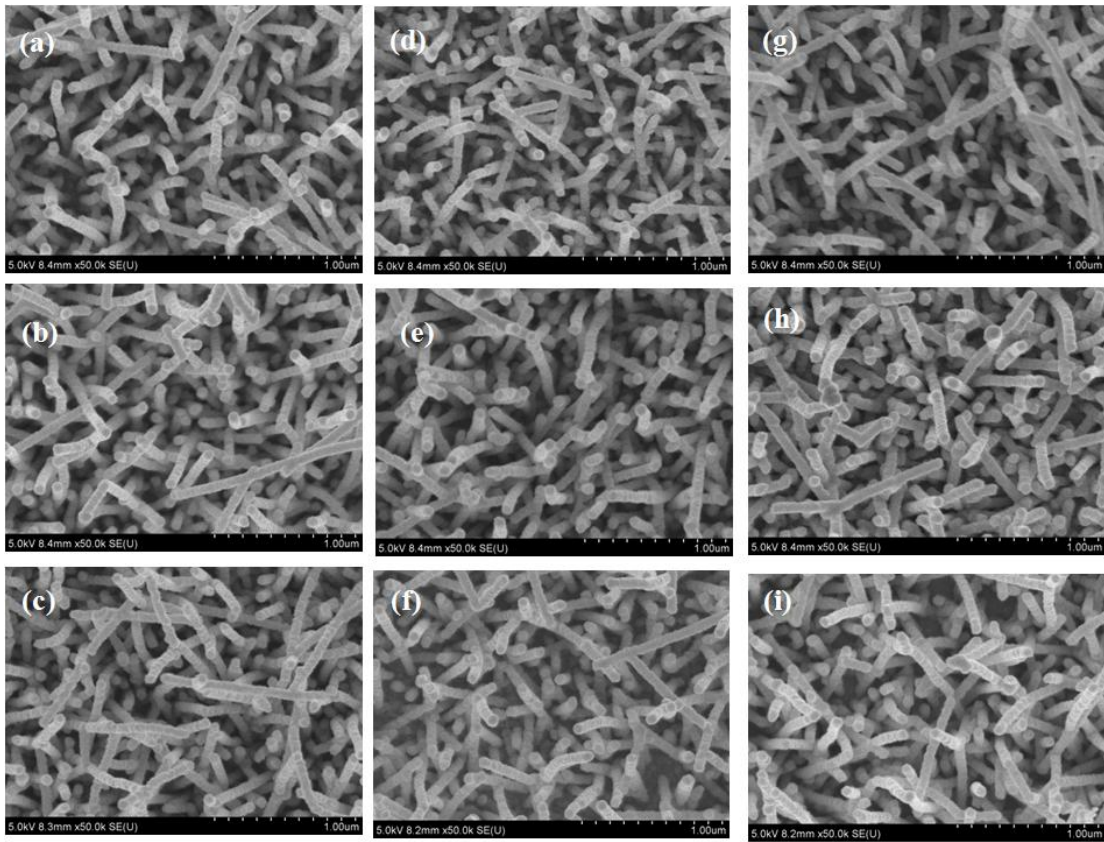


Figure 5.9: SEM images of nickel-coated TMV substrates at different concentrations: (a) - (c) at 0.1 g/L, (d) - (f) at 0.2 g/L, and (g) through (i) at 0.2 g/L and 0.1 g/L. The particle count in $1 \mu\text{m}^2$ cross sections for each of these samples was 46 to 47, showing no significant variation

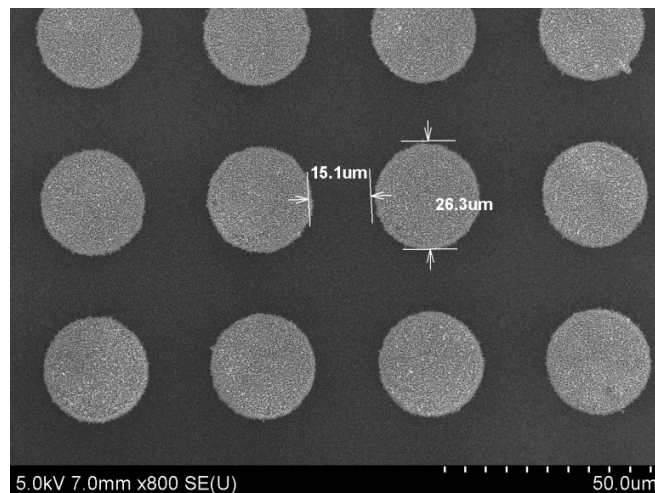
To verify this experimentally, nickel coated TMV samples were prepared using TMV concentrations of 0.1 g/L (A), 0.2 g/L (B) and two overnight steps of 0.2 g/L and 0.1 g/L (C). SEM images of the electrode morphology were taken along with particle counts in $1 \mu\text{m}^2$, following the protocol suggested in previous work by Royston *et al* [91]. This was further verified by mass measurements done on these samples before and after deposition of 400 cycles of TiO_2 using ALD. The average TiO_2 masses measured were 98.75 μg for (A), 89.5 μg for (B), and 100 μg for (C), indicating no significant difference in the mass loading between the samples prepared during the one overnight step at 0.1 g/L and the two overnight steps at 0.2 g/L and 0.1 g/L (for the sample at 0.2 g/L, the lower mass can be attributed to some variability caused during handling samples with tweezers). Consequently, nanostructured only samples were prepared using the 0.1 g/L concentration. This result is consistent with the previously published investigation by Royston *et al* [91] who suggested that the difference in surface coverage in the range of concentrations from 0.1 g/L to 1 g/L is minimal.

The active materials selected to explore the concept of the hierarchical electrodes were TiO_2 and V_2O_5 . The deposition process for TiO_2 was extensively described in chapters 3 and 4. The thickness for the TiO_2 was aimed at 22 nm, using 400 ALD cycles. Deposition of V_2O_5 was performed in the same BENEQ TFS 500 ALD reactor by alternate pulses of vanadium triisopropoxide (VTOP) and ozone at 170°C . An MKS O3MEGATM ozone delivery subsystem was employed to supply a stable 18 wt% flow of O_3 from a pure O_2 source. The deposition rate was measured to be 0.03 nm/cycle (where a cycle denotes one sequence of precursor pulses and purging

pulses in the ALD reactor). The V_2O_5 was deposited for 1000, 2000, and 4000 ALD cycles, aiming at target thicknesses of 30 nm, 60 nm, and 120 nm respectively. As in the case of the electrodes that were fabricated on steel disks and presented in Chapter 4, the mass of either the TiO_2 or V_2O_5 active material was determined by weight measurements before and after ALD deposition.

5.3 Surface Area Enhancement Estimation

In order to estimate the expected increase in surface area added by the micropillars, top-view and cross-sectional SEM images were taken as well to evaluate the diameter and height of the electrodes. Characteristic SEM images are shown in Figure 5.10. Examination of various samples revealed height variation between approximately 55-60 μm , while a variation in the diameter of the pillar across this height was also observed (ranging from roughly 21-22 μm to 27-28 μm from bottom to top). This diameter variation is attributed to the non-vertical sidewalls formed during photolithography, which is typical in thick positive photoresists and can be attributed to the difference in exposure dose and development rate between the top and bottom of the polymer mold.



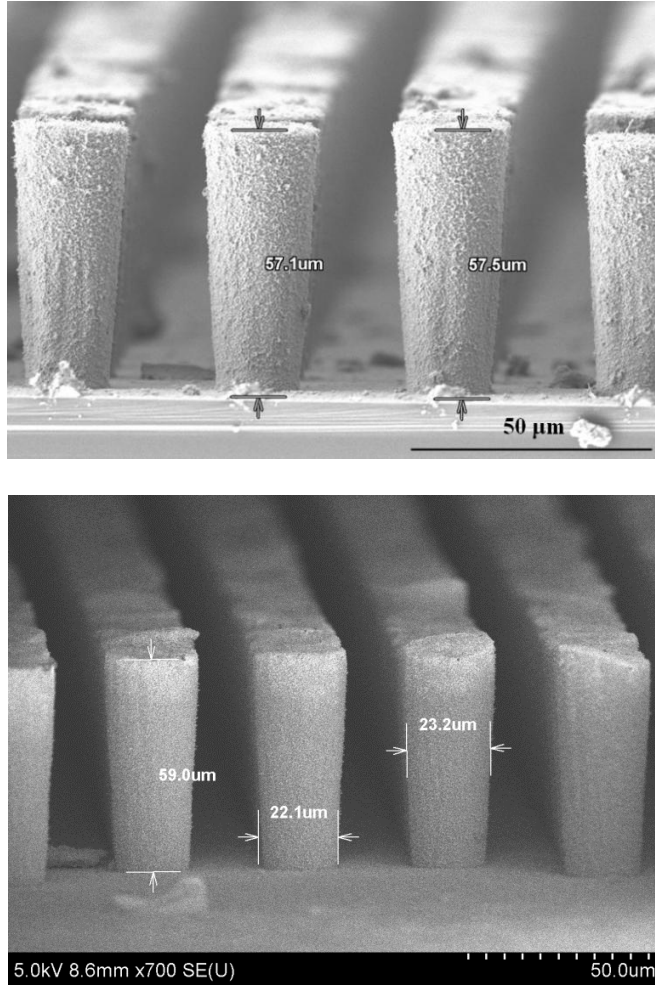


Figure 5.10: Characteristic top and side view SEM images used to determine the pillar dimensions

The increase in surface area A induced by the micropillars for a square pattern can be calculated by the following equation:

$$A = \frac{\pi dh}{s^2} + 1. \quad (1)$$

where d , h , and s are the diameter, height, and spacing of the micropillars, respectively. This equation is derived from a simple geometrical calculation that takes into four adjacent pillars which define a unit cell; the area enhancement for that unit

cell is given by equation (1). The theoretically expected areal gain extracted by the design parameters ($d=20\ \mu\text{m}$, $h=60\ \mu\text{m}$, $s=40\ \mu\text{m}$) that were discussed previously is 3.35. Based on the fabrication results on the range of heights and diameters measured with SEM characterization, the areal gain is estimated to be roughly between 3.4 and 4.2.

As shown in Figure 5.8, ALD produces uniform thin coatings across the entire micro/nano geometry, which implies that the added mass will be very closely related to the increase in surface area. Consequently, an experimental to investigate the effect of increase in area in the electrode architecture is to measure the added mass of the active material that is deposited using. To accomplish this, samples with and without micropillars were diced into square $10.5\ \text{mm} \times 10.5\ \text{mm}$ chips. The bar graph in Figure 5.11 plots the average added mass after 1000 ALD cycles of V_2O_5 for 4 sample types: flat gold coated silicon substrates, substrates with micropillars, substrates with virus structures only (denoted nanostructured only), and samples with both micropillars and viral nanostructures (denoted hierarchical). The measurements show added mass of $13\ \mu\text{g}$ for flat substrates, $41\ \mu\text{g}$ for substrates with micropillars only, $97\ \mu\text{g}$ for nanostructured only substrates, and $296\ \mu\text{g}$ for hierarchical substrates. The larger error bars for samples containing TMV are attributed to some variability in the coating uniformity from sample to sample.

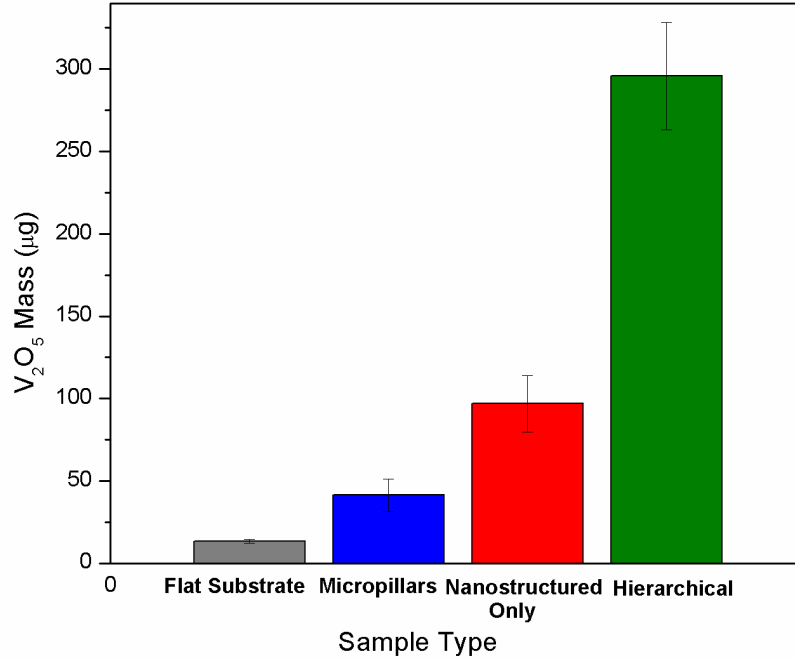


Figure 5.11: Bar graph plotting the average V_2O_5 mass deposited after 1000 ALD cycles on four types of samples including flat substrates, substrates with micropillars only, nanostructures only, and hierarchical electrodes

Since the chips had a side of 10.5 mm, the samples used for these experiments were 1.1 cm^2 in area with only 1 cm^2 covered by the micropillars, so this factor should be accounted for in eq. (1) to interpret the mass measurements results. Taking this into account, it is observed that the increase in added mass follows the anticipated trend of surface area increase. Specifically, a 3-fold increase in added mass is observed due to the micropillars while an ~ 7.5 -fold increase is estimated for virus-structured surfaces. Both of these results are in good agreement with previous measurements on the virus-induced surface area increase [91] as well as the estimations for the increase in area added by the micropillars in the current work. For the nanostructured only electrodes in particular, the measured increase in mass is in close agreement with a theoretical estimation for the ideal increase in area, if the

viruses are assumed as perfect cylinders with a diameter of 60 nm (40 nm for the Ni coating and 20 nm for the TMV particle) and a spacing of 70 nm (enough to accommodate the target thickness of V_2O_5 between adjacent particles). Using equation (1), an area enhancement of 8 is estimated, assuming up to layers of TMV particles align head to tail. While the above equation gives area increase between 12 and 25 for one and two layers of TMV, respectively (if the core/shell layers have a combined thickness of 20 nm – currently occupied by nickel only), the current energy storage application requires the existence of both layers to achieve significant capacity values.

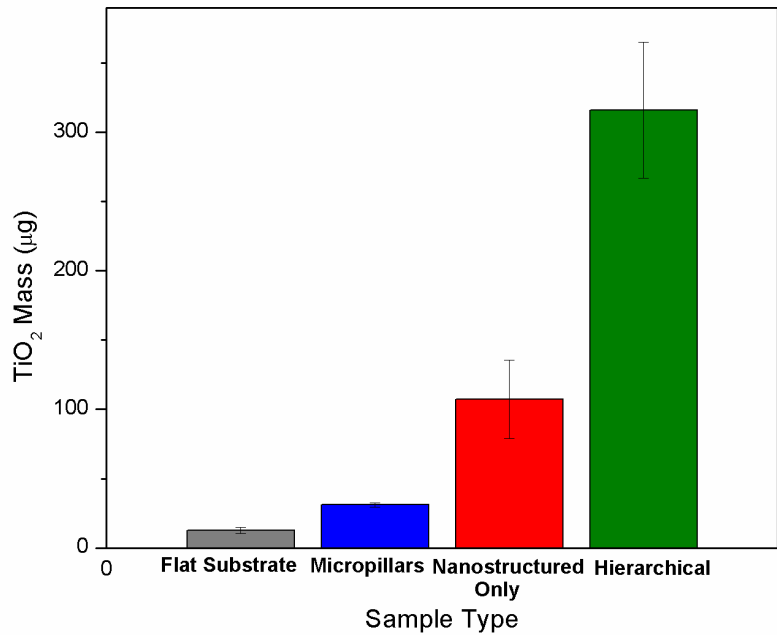


Figure 5.12: Bar graph plotting the average TiO_2 mass deposited after 400 ALD cycles on four types of samples including flat substrates, substrates with micropillars only, nanostructures only, and hierarchical electrodes

This result was further verified by similar weight measurements in the same types of samples with 400 ALD cycles of TiO_2 . Results from these tests are shown in Figure 5.12 where average masses of roughly 12 μg , 31 μg , 107 μg and 317 μg are

measured for flat substrates, substrates with pillars only, substrates with TMV nanostructures only, and hierarchical samples, respectively. Similar increases in the deposited mass are obtained for TiO_2 as well, indicating that the process is independent of the active material and is reliable in giving an estimate for the increase in area.

5.4 Electrochemical Testing Results – Teflon/Stainless Steel Cell (TiO_2 active material)

The hierarchical electrodes presented in this work were fabricated on silicon substrates. As a result, conventional coin cell methods cannot be directly used for the experimental testing due to the non-conductive nature of the substrate. To alleviate this limitation, the first generation of testing was facilitated by a custom designed experimental apparatus that enabled electrical connections to both electrodes from the top side. At the same time, particular attention was placed to the proper sealing of the cell, since any exposure to ambient can be catastrophic in a Li-ion battery cell.

Figure 5.13 shows an optical image of the custom-designed electrochemical cell that was used in the first round of testing. The cell consists of teflon and stainless steel manifolds that are arranged in alternating sandwiched structure. Teflon was selected due to its chemical resistance and electrochemical inertness in a Li-ion battery cell. However, it can be mechanically deformed when heated or strained and this could be a limitation in the proper sealing of the device, since dehydration bakes are required prior to electrode testing. To avoid this problem, stainless plates are used to apply pressure on the teflon pieces and keep them flat during cell packaging and testing. In this cell, all square pieces are 45 mm x 45 mm while the chip cavity is 16.5

mm x 16.5 mm. The thickness of the thinner parts is 2 mm while the thick teflon base is 12 mm thick. All pieces have machined through-holes 1.5 mm in diameter which facilitate the electrical connections to the electrode surfaces.

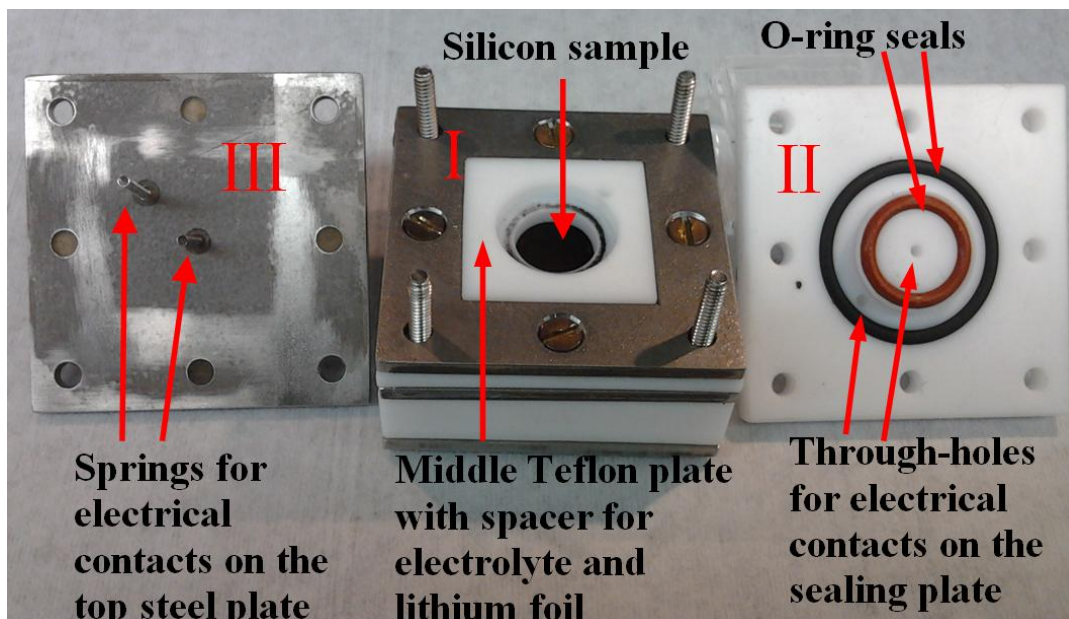


Figure 5.13: Optical image showing the custom-designed electrochemical cell used for the first generation of testing; the numbers I, II, III, indicate the three different components involved in the cell assembly

The device assembly takes place in an Argon filled glove box with O₂ concentration less than 0.2 ppm. It begins by placing silicon chips with hierarchical electrodes on the base of the package (part I). The silicon chips in this case were diced in 16 mm x 16 mm; the additional area is used to facilitate the top side connection to the working electrode from the package corners. After placement of the first steel plate, a second teflon piece is aligned on top; this piece has a rubber o-ring on the bottom with a diameter of 12 mm. This o-ring defines the electrode active area and provides the seal for the silicon chip. The top-side of this piece (shown in part I of Figure 5.13) has a machined cavity with a two-fold functionality. First, it creates a

physical separation between the working and counter electrode that is filled with electrolyte while it also allows placement of the counter electrode. The assembly proceeds by placing two pieces of polymer separator inside the cavity and then filling it with electrolyte (1 M LiPF₆ in 1:1 EC:DEC). The separator is used mainly as a precaution, since pressure on the top side may cause the pliable lithium electrode to bend significantly and short-circuit the cell. After electrolyte insertion, lithium foil is pressed against a stainless steel disk and the layer stack is placed on top of the cavity. At this point, a second stainless steel plate is used to compress the o-ring in the teflon and the whole assembly is screwed down as shown in Figure 5.13. Piece II is then placed on top of the stainless steel assembly. This piece has two o-rings to ensure proper seal of the counter electrode as well. Finally, the last stainless steel plate (part III) is used to apply pressure on the teflon and provide the electrical connections to the anode and cathode through springs that have glued to the bottom surface and brass pins on the top surface. Washers are then screwed on the alignment pegs and the sandwiched cell is wrapped with teflon and electrical tape to enhance the sealing quality. An optical image of a packaged device under operation is presented in Figure 5.14, where the electrical connections using alligator clips on the brass pins are shown.

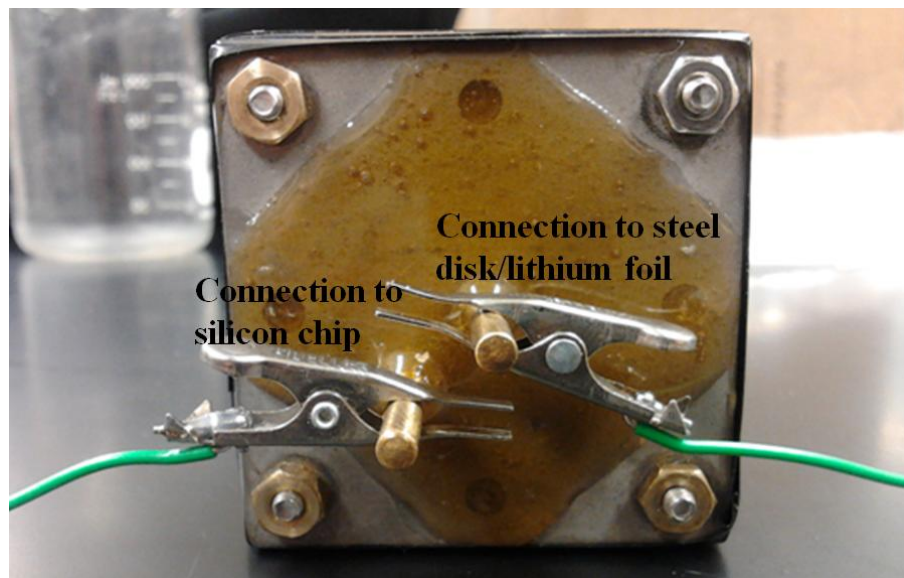


Figure 5.14: Assembled package under test showing the electrical connections to the electrodes. In this image, the electrical sealing tape as well as the epoxy used to glue the brass pins are also visible

The first round of experimental testing used 400 ALD cycles of TiO_2 as the active material on the hierarchical electrodes, fabricated using the process described in section 5.2. At the time of these preliminary experiments, the V_2O_5 material was still under development. It should be reiterated that both materials in this work are used primarily as model systems to investigate the merits of the hierarchical electrode technology rather as electrodes for performance optimization. Consequently, the choice of material in the experiments was driven by the simplicity in processing, assembly, and fabrication.

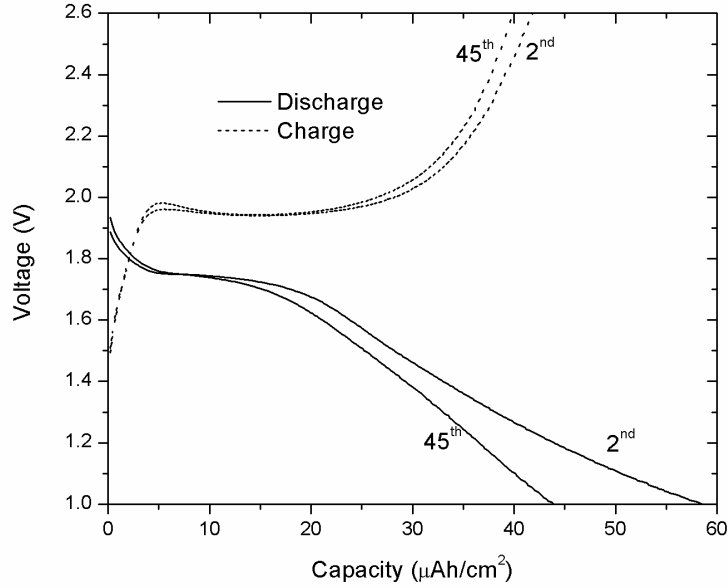


Figure 5.15: Discharge/charge for a hierarchical electrode cycled at constant current density of $26.5 \mu\text{Ah}/\text{cm}^2$

Figure 5.15 shows characteristic discharge/charge curves for the 2nd and 45th cycle of operation for a hierarchical electrode cycled galvanostatically at $26.5 \mu\text{A}/\text{cm}^2$. Proper device operation is verified from the graph, since the plateaus for discharge around 1.7 V and charge around 1.9 V are clearly observed. This behavior was characteristic of TiO_2 as was analyzed in Chapter 4. The capacity drops from $58.6 \mu\text{A}/\text{cm}^2$ in the 2nd cycle to $43.9 \mu\text{A}/\text{cm}^2$ in the 45th cycle. This indicates an average fading rate of 0.57% per cycle and verifies the cyclic stability of the electrode. Since extensive cycle life experiments were performed for the electrodes developed on the steel disks, further cycling was manually stopped.

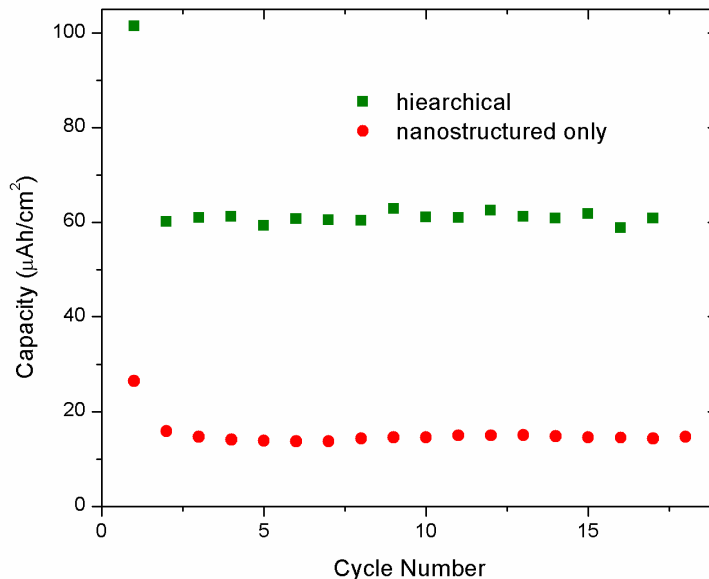


Figure 5.16: Discharge capacity vs. cycle number for hierarchical and nanostructured only electrodes cycled at a constant current density of 13 $\mu\text{Ah}/\text{cm}^2$

Figure 5.16 shows discharge capacity vs. cycle number data for hierarchical and nanostructured only electrodes for the first 17 cycles of operation, when testing was manually stopped. Galvanostatic cycling was performed at a current density of 13 $\mu\text{Ah}/\text{cm}^2$. The high capacity in the first cycle has been extensively addressed in Chapter 4 and is attributed to irreversible capacity in the underlying nickel layer as well as side reactions with the electrolyte. A capacity of $\sim 60 \mu\text{Ah}/\text{cm}^2$ is obtained for the hierarchical electrode while the nanostructured only electrode shows a capacity of $\sim 15 \mu\text{Ah}/\text{cm}^2$. This four-fold increase in capacity is attributed to the higher surface added by the micropillars. The value is at the higher end of the expected range for energy density increase as calculated previously. However, it is still consistent with the range of increase in surface area that has been estimated based on the experimental geometrical parameter measurements and the corresponding calculations. The factor of four can be attributed to the mass difference between the

two particular samples tested in this experiment. Overall, this result constitutes the first demonstration of the merit of the hierarchical approach in increase the energy density of the TMV-templated electrodes for the same device footprint.

5.5 Electrochemical Testing Results – Coin Cells (V_2O_5 active material)

5.5.1 Changes from Previous Set-up

Even though the teflon/stainless steel testing apparatus described in section 5.4 produced reliable and stable electrochemical results, some limitations in its use were progressively identified. The major disadvantage of this testing approach is that it does not allow multiple parallel tests. Specifically, due to the prohibiting unit cost (approximately \$1,500), only four cells were initially machined, including the pilot prototypes. As a result, a maximum of three to four experiments could be conducted in parallel, making the testing procedure slow. An additional limitation that emerged after repeated testing was the gradual degradation of the electrical contacts. More specifically, after repeated use, the springs would be deformed while the brass pins would be detached from the electrically isolating epoxy. In addition to that, corrosion of the brass material was observed during the rinsing and drying process from test to test. All these issues that mandated constant replacement of parts combined with the non-highly parallel testing capabilities, created the requirement for a more efficient testing scheme.

This issue was addressed by revisiting the coin cell assembly process that is used for electrodes with steel disk current collectors. As mentioned previously, the critical bottleneck is the non-conductive nature of the silicon substrate on which the electrodes are fabricated. To account for this, the fabrication process for the samples

was modified to create a contact around the entire silicon chip surface. Initially, this was attempted through the application of silver paste on the backside and sidewalls of the silicon chip. However, the Ag paste was found to be electrochemically unstable higher than 3.6 V, while exhibiting some irreversible capacity around 1.5 V as well. In addition, at higher current densities it was no longer an efficient current collector due to decreased conductivity. Finally, the successful implementation of a contact was accomplished by sputtering Cr/Au layers on both the top and bottom side of the individual chips before TMV deposition; as well as sputtering on the back side after ALD of the active material in case where the resistivity was still high (higher than a few ohms). Using this approach excellent electrical contact to the silicon chip was obtained with resistance values as low as $<1 \Omega$. In addition to the sputtering of backside contacts, the chips were now diced in 10.5 mm squares as in the case of the mass measurements to accommodate for the smaller space available in the coin cell. An optical image of a silicon chip in the coin cell along with an actual battery in the holder that is used for testing is shown in Figure 5.17. This testing approach has the disadvantage of adding more steps to the fabrication since two to three sputtering steps are required. On the other hand though, electrodes can be assembled using the traditional battery testing approach, which enables highly parallel testing of disposable cells.

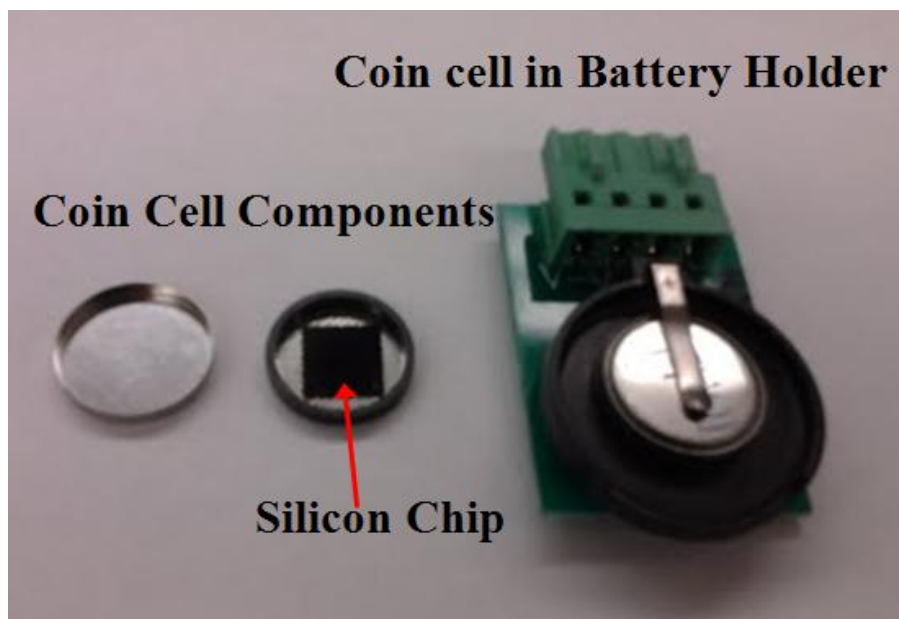


Figure 5.17: Optical image showing the silicon chip inside the coin cell components along with a packaged coin cell in the battery holder used for testing

An additional change that was made in the second round of testing was the replacement of the TiO_2 active material with V_2O_5 . As analyzed in Chapter 4, the existence of the Ni core underneath the active material shell creates some background and irreversible capacity that fades within the first cycles for the TiO_2 electrode. On the other hand, in the voltage range used for V_2O_5 testing Ni shows no background electrochemical signal. This was deemed more beneficial as a model system especially for the varying thickness experiments, where the ratio of the active material loading to the core loading in the Ni/ TiO_2 system could have an influence on the amount of background capacity.

5.5.2 Energy Density Analysis

V_2O_5 electrodes were prepared using the deposition parameters listed in section 5.2. After deposition, the electrodes were characterized using XRD to verify the

presence of crystalline material, as expected from the ozone-based deposition process. Figure 5.18 shows XRD data taken for V_2O_5 films deposited on flat gold-coated substrates, nanostructured only substrates (Ni-coated TMV on Au-coated Si) and hierarchical substrates (with micropillars and Ni-coated TMV). Samples containing TMV show additional [200] and [110] peaks to main [001] peak, due to the orientation of the particles. Interestingly, samples with micropillars show a decreased intensity in the XRD signal. This can be attributed to absorption of X-rays by the thick gold pillars.

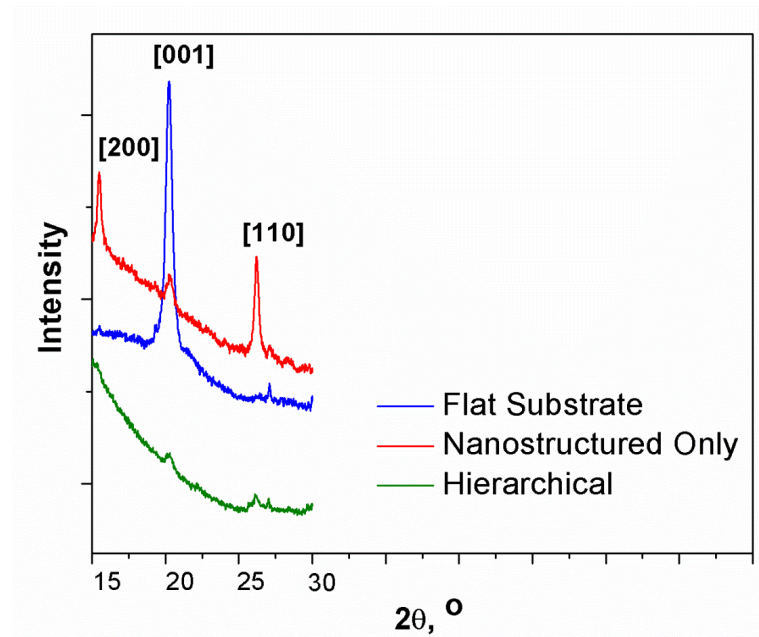


Figure 5.18: XRD data for V_2O_5 material deposited on three different substrates

Figure 5.19 shows Cyclic Voltammetry (CV) scans for electrodes with and without micropillars in the voltage range of 2.6 to 3.6 V. The thickness of V_2O_5 in these experiments was 30 nm (1000 ALD cycles). Two oxidation peaks at 3.35 V and 3.15 V as well as two reduction peaks at 3.25 V and 3.45 V can be observed for both the hierarchical and nanostructured only electrodes, which are characteristic for lithium insertion in/extraction from the V_2O_5 crystal structure, respectively. It can be

seen that the surface area under the curves as well as the peak currents are higher by a factor of three for the three-dimensional electrodes. This is in excellent agreement with the increase in mass and surface area.

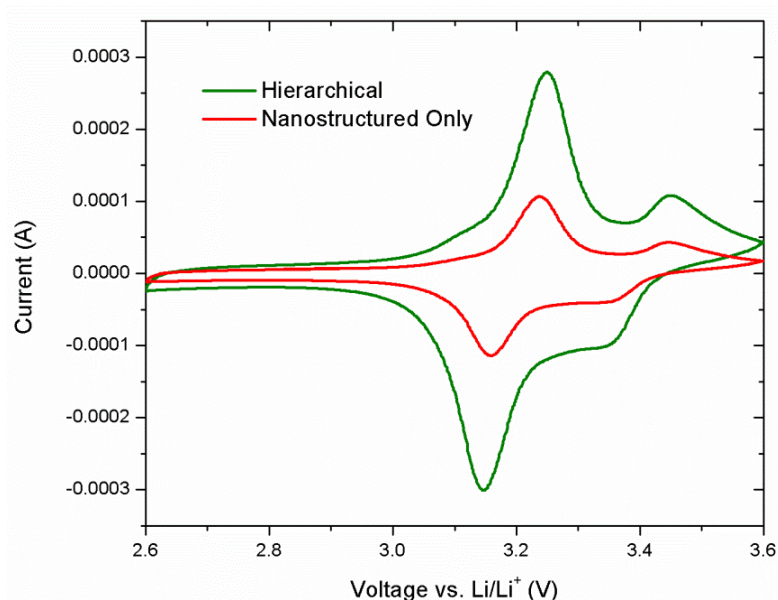


Figure 5.19: CV scans for hierarchical and nanostructured only electrodes with V_2O_5 active material taken in the 2.6 V to 3.6 V range with a 0.5 mV/s sweep rate

This feature is more clearly illustrated in Figure 5.20, which shows discharge/charge curves at a current of 10 μA for these two samples in the same voltage range. First of all, the plateaus at the discharge/charge cycles appear at similar voltages as the current peaks in Figure 5.19, consistent with the concept that the area under a CV curve corresponds to material capacity. The energy storage capacity for the hierarchical electrode is 38 $\mu\text{Ah}/\text{cm}^2$, while the nanostructured only electrode exhibits a capacity of 13 $\mu\text{Ah}/\text{cm}^2$, a 3-fold increase within the predicted range obtained Figure 5.11. Based on the mass measurements for these electrodes, the gravimetric capacities are 129 mAh/g and 134 mAh/g, respectively. These are within the range of the theoretical capacity for V_2O_5 (147 mAh/g) in the voltage range used

in these experiments [123]. As indicated in Figure 5.21, where the capacity versus cycle number for the first 35 cycles of operation is plotted, this 3-fold increase in energy density is demonstrated throughout the course of testing.

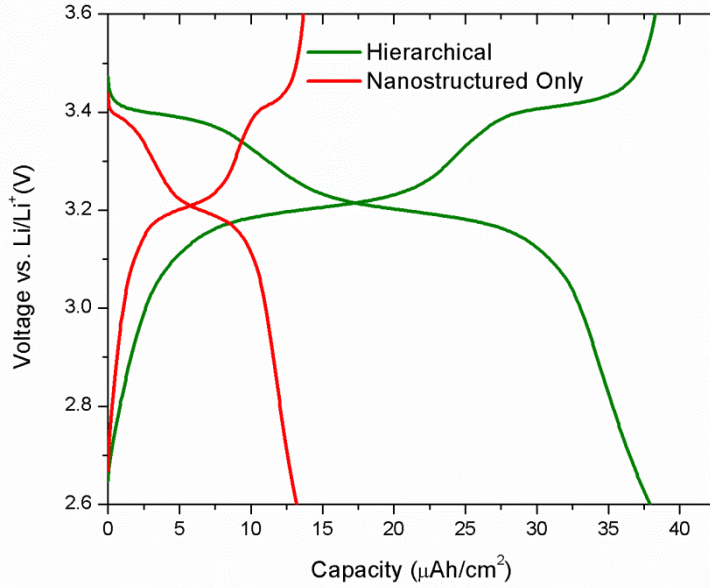


Figure 5.20: Characteristic discharge/charge curves during the 2nd cycle for hierarchical and nanostructured only electrodes with 30 nm of V₂O₅ (1000 ALD cycles)

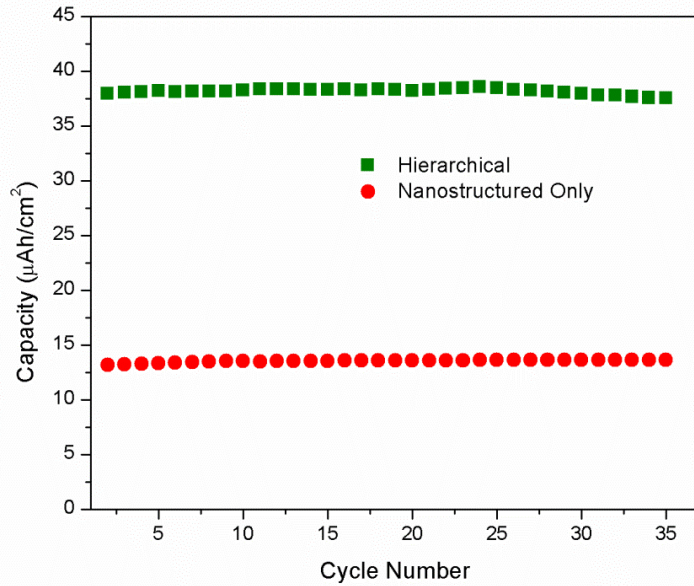


Figure 5.21: Capacity vs. cycle number for the first 35 cycles of operation for the electrodes shown in Figure 5.20

The effect of increasing the active material coating thickness in the hierarchical electrode architecture performance was also investigated. V_2O_5 was deposited on three-dimensional electrodes for 1000, 2000 and 4000 ALD cycles. Characteristic galvanostatic discharge/charge curves for three such samples at a current of $12 \mu\text{A}$ are shown in Figure 5.22. Capacities of $33 \mu\text{Ah}/\text{cm}^2$, $63 \mu\text{Ah}/\text{cm}^2$ and $86 \mu\text{Ah}/\text{cm}^2$ are obtained for 1000, 2000, and 4000 cycles of ALD, respectively. Interestingly, the capacity increase exhibits a non-linearity as the thickness of the active material increases from approximately 60 nm (2000 ALD cycles) to 120 nm (4000 ALD cycles). Interestingly, the capacity increase exhibits a non-linearity as the thickness of the active material increases from approximately 60 nm (2000 ALD cycles) to 120 nm (4000 ALD cycles).

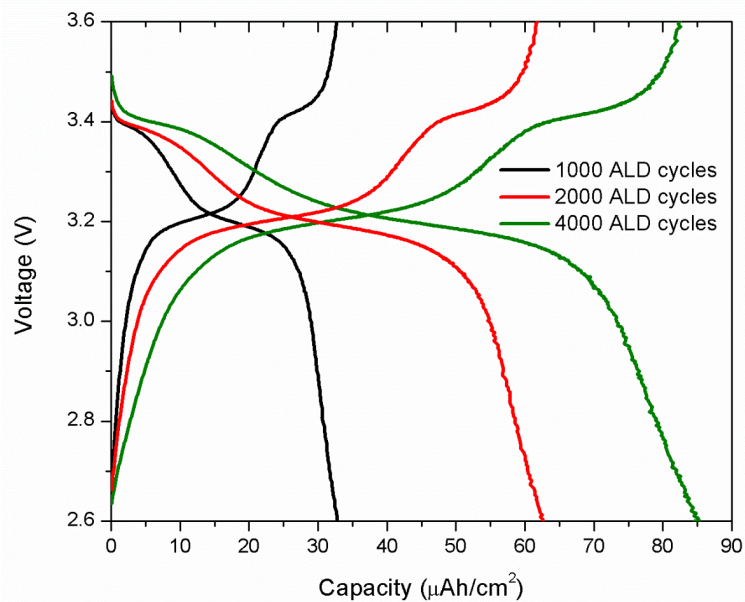


Figure 5.22: Galvanostatic discharge/charge curves for hierarchical electrodes at a current of 12 μA ; V_2O_5 was deposited for 1000, 2000, and 4000 ALD cycles, aiming at thicknesses of 30 nm, 60 nm, and 120 nm, respectively

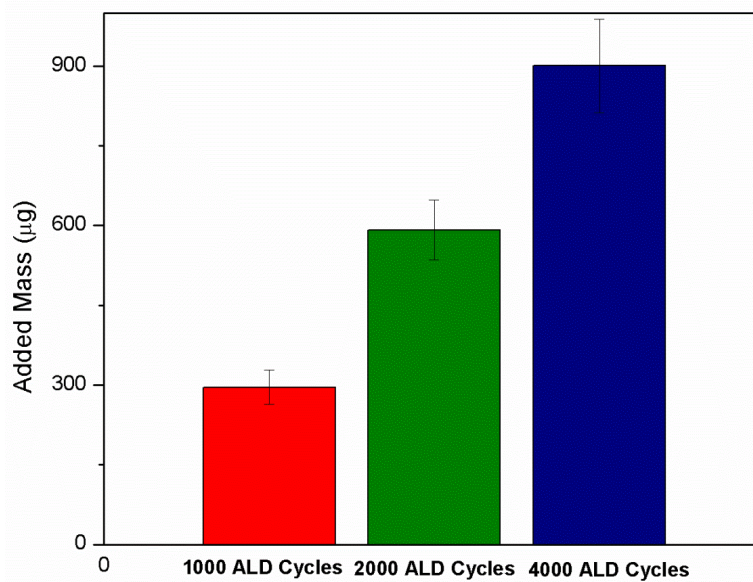


Figure 5.23: Added mass measurements for hierarchical electrodes containing V_2O_5 with different thicknesses; 1000, 2000, and 4000 ALD cycles correspond to thicknesses of 30 nm, 60 nm, and 120 nm, respectively

This behavior, as expected, is closely related to the increase in mass loading, as

measured for several samples with different V_2O_5 thicknesses. Figure 5.23 shows the average added mass measurements for these three types of samples, and can be used to explain the trend observed in Figure 5.22. The underlying cause of this behavior can be further understood if the micro/nano structure of the electrodes is taken into consideration. Figure 5.24 shows SEM images taken from the top of the micropillars for 1000, 2000, and 4000 V_2O_5 ALD cycles. While for thicknesses of up to 60 nm the three-dimensional nano-morphology of the electrodes is maintained, higher active material thickness results in loss of surface area and porosity.

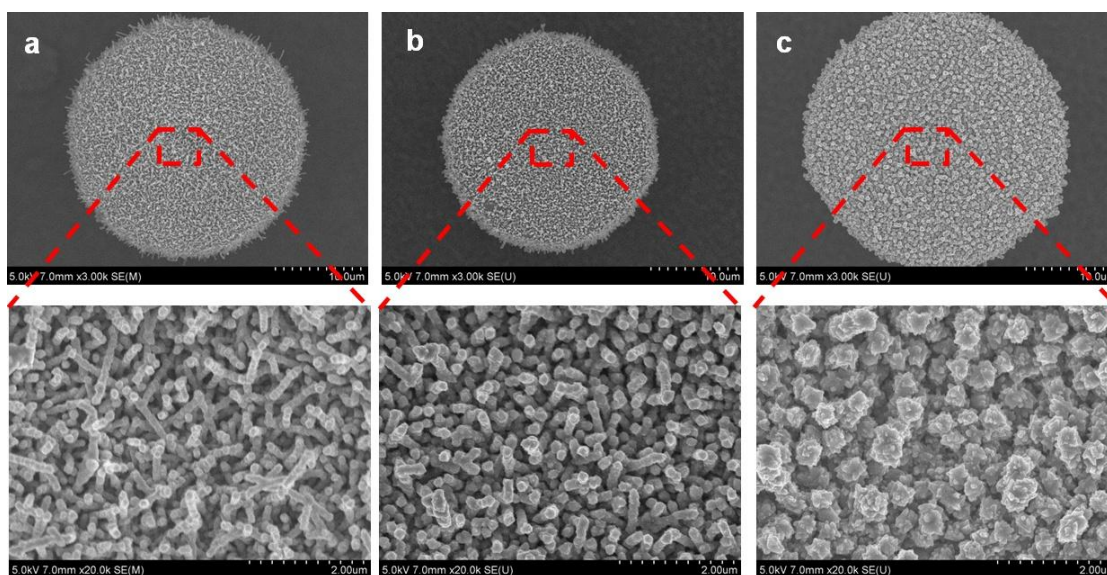


Figure 5.24: SEM images showing the top of micropillars for, a, 1000 ALD cycles of V_2O_5 , b, 2000 ALD cycles of V_2O_5 , c, 4000 ALD cycles of V_2O_5

Examination of cross-section TEM images taken from hierarchical samples with 2000 and 4000 ALD cycles of V_2O_5 verify the reduced porosity and effective surface area for the thicker active material and are shown in Figure 5.25. This is attributed to progressive blocking of open spaces between closely packed adjacent TMV nanorods with increasing deposition thickness, which results in partial planarization of previously accessible areas and consequent non-linear increase in added material

mass.

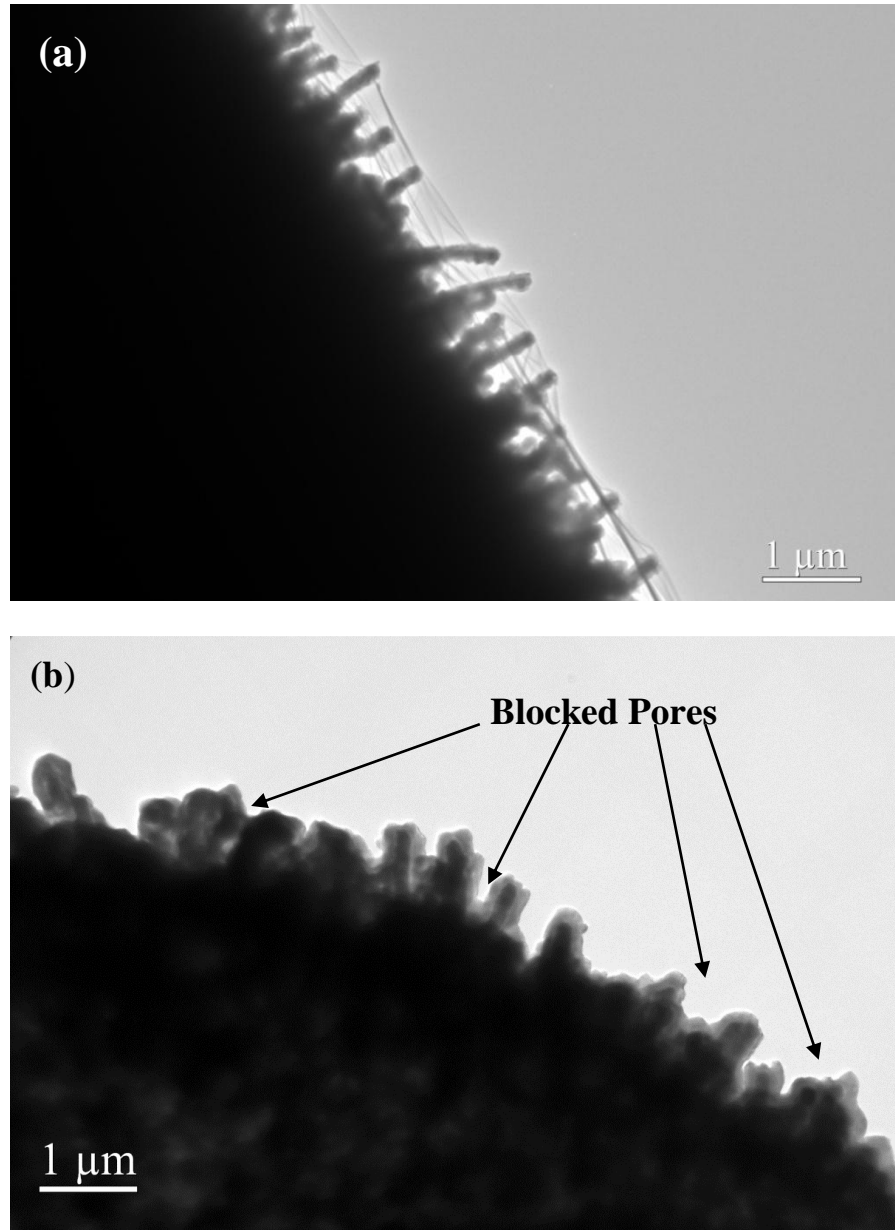


Figure 5.25: Cross-section TEM images of hierarchical electrodes with (a) 2000 ALD cycles and (b) 4000 ALD cycles of V_2O_5

5.5.3 Power Density Analysis

The behavior of electrodes with similar V_2O_5 thickness at different loads (applied currents) and current rates was also examined. The electrode thickness that was selected for these experiments was 30 nm, due to the less time required for V_2O_5 deposition. Since the active material is very thin, similar results can be obtained for the other thicknesses as well. In these studies, half cells were cycled in increments of 10 cycles for progressively increasing current values.

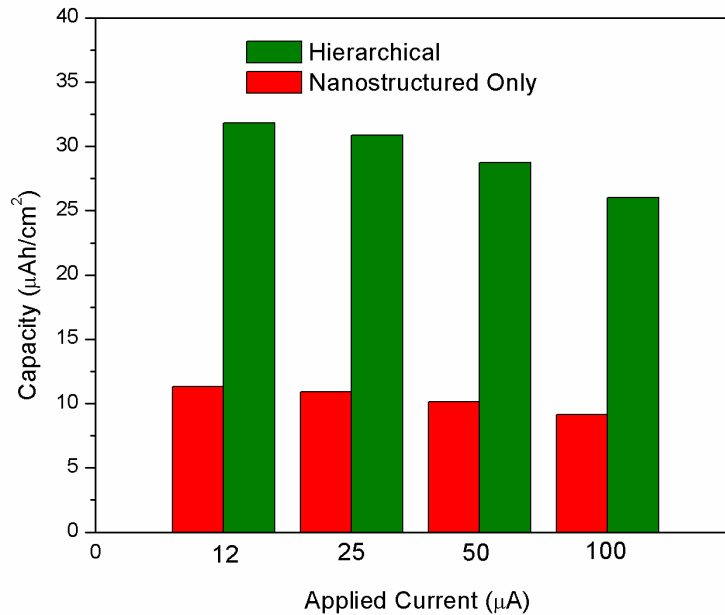


Figure 5.26: Average capacities for hierarchical and nanostructured only electrodes with 30 nm of V_2O_5 (1000 ALD cycles) at different current values (reminder: footprint is 1.1 cm^2)

Figure 5.26 shows the average capacities obtained for hierarchical and nanostructured only electrodes for different current densities. The applied currents of 12 μA , 25 μA , 50 μA , and 100 μA correspond to current densities of 11 $\mu\text{A}/\text{cm}^2$, 22.7 $\mu\text{A}/\text{cm}^2$, 45.5 $\mu\text{A}/\text{cm}^2$, and 91 $\mu\text{A}/\text{cm}^2$, respectively. The capacities obtained are 3 times higher for the hierarchical electrode for all current densities, indicating that the energy density scales by the same factor, independent of the battery load.

A similar trend is also observed when the samples are cycled at similar C-rates (it is noted that a rate of nC means that a battery is fully charged and discharged at $1/n$ hours). As shown in Figure 5.27a, the capacity remains 3 times higher for the hierarchical electrodes for all C-rates, while both the hierarchical and nanostructured only electrodes demonstrate similar rate capabilities that vary within 2-5%. The rate capability is described in terms of the percentage of capacity retention at each current rate, and it is plotted in Figure 5.27b. The data is presented based on the ratio of C_i/C_{inav} , where C_i is the capacity for each cycle, and C_{inav} is the average initial capacity for the lower C-rate. This result implies that the addition of the micropillars increases the energy density of the electrodes without affecting the high rate performance, which is characteristic of nanostructured materials, since higher energy densities are achieved without increasing the thickness of the active material.

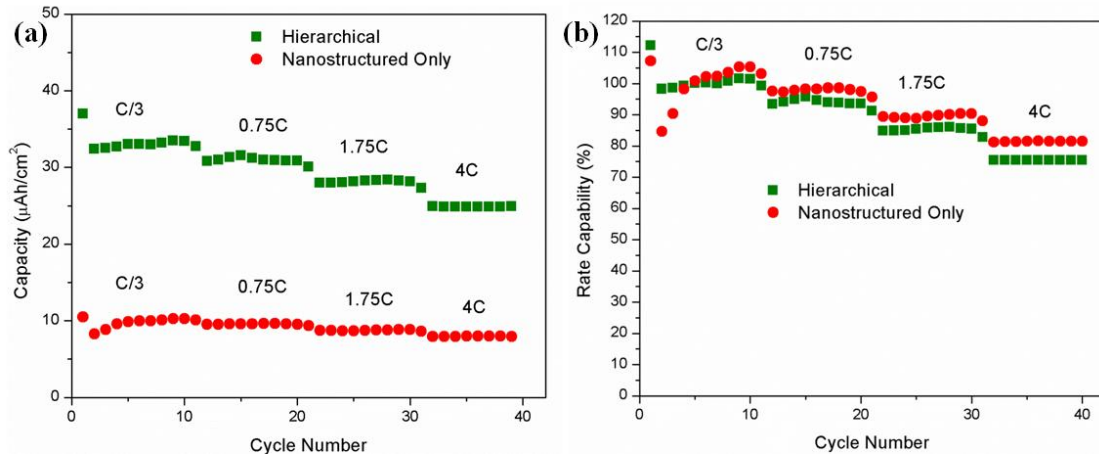


Figure 5.27: (a) Capacity vs. cycle number for electrodes with and without micropillars at different C-rates, (b) rate capability for the electrodes shown in (a) (V_2O_5 thickness is 30 nm - 1000 ALD cycles)

5.6 Discussion on the Hierarchical Electrodes

In this first prototype microbattery electrode architecture, the micropillars were

fabricated using a moderate aspect ratio of 2.5:1 to 3:1 to demonstrate the significant merits of this technology. In our previous work, equally uniform viral coating of gold-coated silicon-etched microstructures with aspect ratios as high as 9:1 has been accomplished [108]. Consequently, even higher energy density enhancement can be achieved with higher aspect ratio geometries, since the nanostructure component of the electrode is based on the TMV self-assembly. Even though V_2O_5 was used as a model material, when compared to previously reported data on V_2O_5 thin film electrodes, the capacities obtained even from this moderate geometry are comparable to those achieved for much thicker films [127]. More specifically, Nanove *et al* reported capacities of $\sim 38 \mu\text{Ah}/\text{cm}^2$ and $60 \mu\text{Ah}/\text{cm}^2$ for RF sputtered 2D electrodes with thicknesses of $1.2 \mu\text{m}$ and $1.8 \mu\text{m}$, respectively. In the current work, similar capacity values were obtained for geometries with V_2O_5 films as much as 30 to 40 times thinner due to the combination of high surface area nanostructures with three-dimensional micropillars. Further increase in the aspect ratio of micropillars can result in energy densities per unit area comparable to the values reported for state-of-the-art three-dimensional designs [37]. For example, based on equation (1), electroplating of gold micropillars with similar diameter ($20 \mu\text{m}$) through $300 \mu\text{m}$ silicon wafer molds can result in an area gain of 12.8, with a projected capacity of up to $320 \mu\text{Ah}/\text{cm}^2$ for a $60 \text{ nm } V_2O_5$ film.

A very important characteristic of this technology is the versatility it allows for the fabrication of different materials using various methods. In this work, gold current collectors and TiO_2 and V_2O_5 active materials were used, however other combinations can be selected to facilitate various electrode/current collector

combinations. For example, while gold is suitable for cathode electrodes, similarly nickel or copper micropillars could be used for anode materials, which have also been demonstrated in work done by our group. At the same time, active materials can be deposited with various conformal coating deposition techniques (such as electrodeposition, CVD, or sol-gel), in addition to atomic layer deposition.

In addition to the structural versatility of this technology, the most significant benefit of the hierarchical approach is highlighted if the results that describe the effect of increasing active material thickness in section 5.5.2 are further analyzed and their implications are explained. It was observed that a non-linear increase in added mass and energy density was obtained, accompanied by a reduction in surface area and porosity. While this might not be too much of a concern for V_2O_5 films that were deposited up to thicknesses of 3-4 μm with little capacity fading at various C-rates [127], this can be catastrophic if other materials are used such as Si or TiO_2 [112, 113]. In such electrochemical systems, high surface area to accommodate volume expansion during lithiation (Si, Sn) and store additional capacity at the grain boundaries (TiO_2), as well as thin active material coatings that mitigate the effects of poor electronic and ionic conductivity, are equally necessary. The hierarchical design proposed in this work is ideally suited for the fabrication of high energy and power density microbatteries based on these electrodes, since very high surface area nanostructured materials can be self-assembled onto microstructures. As a result, increasing the energy density can be accomplished solely by increasing the aspect ratio of the microstructures. This mitigates the need for additional mass loading, which in turns maintain the high surface area and porosity of the electrode.

5.7 Summary

In summary, the development of three-dimensional microbattery electrodes that consist of micro and nano components was discussed in this chapter. The electrodes are made of self-assembled nanostructured forests templated using *Tobacco mosaic virus* particles, which conformally coat three-dimensional microfabricated gold pillars. This constitutes the first demonstration of combining bottom-up biological self-assembly and top-down micromachining in a microfabricated energy storage device. In addition to the novel fabrication process, custom-made testing manifolds were designed and prepared to facilitate efficient battery testing on silicon substrates outside of an argon-filled glove box.

The active battery materials tested were TiO_2 and V_2O_5 , both deposited using atomic layer deposition across the entire micro/nano surface. Due to the excellent conformality achieved by both the viral self-assembly and the ALD process, the energy density of the three-dimensional electrodes can be increased by a factor that is in good agreement with the expected increase in surface area added by the micropillars. At the same time, thin active material coatings enable fast discharge/charge rates while maintaining higher energy densities. Even though TiO_2 and V_2O_5 were used as model materials, the process can be expanded to a variety of active materials that can be deposited using conformal deposition techniques, while microstructures with higher aspect ratio geometries can further increase the available energy densities. This technology can serve as the foundation for the development of next-generation energy storage devices with high energy and power densities for small-scale power applications.

Chapter 6 : Summary and Future Work

6.1 Summary of Work

This Dissertation presented the development of a paradigm shifting technology for the fabrication of three-dimensional microbattery electrodes. Existing technologies have been leveraging on the three-dimensional micro and nanostructured electrodes which independently possess attractive attributes for improving microbattery performance for small scale applications. More specifically, microstructured 3D electrodes increase the energy density due to increased surface for the same footprint but lack in power density due to the micro-sized distances for ion diffusion and electron transport. Nanomaterials enable very high rate performance as a result of reduced transport lengths, however, due to their high porosity, they suffer in energy density since the mass loading is smaller. The technology developed in this work combines advantages of both length scales. The electrode active material is made of high surface area nanostructured forests, which facilitates very high rate performance. This forest of active materials is self-assembled onto three-dimensional microstructures, which alleviates the problem of reduced mass loading and enables tunable energy densities.

The first prototype electrode device consisted of gold micropillars which have been electroplated onto silicon wafers through a thick positive photoresist mold. The nanostructures were templates on self-assembled *Tobacco mosaic virus* particles, which can uniformly coat the microstructures. Finally, the active battery material was deposited conformally throughout the entire surface using ALD of TiO_2 and V_2O_5 . In

this first geometry, the micropillars were designed with 60 μm in height, a diameter of 20 μm , and a center to center spacing of 40 μm . Based on these dimensions, an approximately 3-fold increase in surface area was estimated. Due to the conformal nature of both the virus coating process as well as the ALD of the active material, this increase in area was expected to correspond to an equivalent increase in mass loading and energy density. Experimental results verified that the increase in mass loading from nanostructured only to hierarchical electrodes followed the predicted area enhancement. Electrochemical characterization of the electrodes indicated a similar 3-fold increase in energy density. Equally importantly, this increase in energy density does not come at the expense of power density, as electrodes with and without micropillars showed similar rate capability. These results combined indicate the significant merit of this new technology. The electrode energy density can be adjusted by the geometrical characteristics of the micropillars while the power density can be maintained at high levels due to the small active material thickness.

There were a number of challenges that were faced and addressed throughout the development of this work. A first challenge was related to the integration of nanostructures in functional battery architectures. While nanomaterials offer notable benefits for energy storage devices, they cannot be easily integrated in device environments due to incompatibility in the synthesis process with standard microfabrication techniques. In this work, we leveraged on the self-assembly capabilities of the TMV to incorporate it in MEMS fabrication processes. A toolbox of biofabrication processes that included photolithographic patterning and self-

assembly onto complex 3D architectures was developed, which demonstrates an alternative and facile route to integration of nanostructures in functional devices.

The second major issue that was addressed in this Dissertation was the development of active battery materials using the TMV scaffold. The formation of inorganic coatings on the TMV using electroless plating reactions is limited to only a few materials, primarily metals. Other wet chemical processes available are not compatible with the stability windows of this biological molecule. On the other hand, Li-ion battery materials are mainly ceramic or semiconducting materials that cannot be easily synthesized using these techniques. To alleviate this limitation, the bottom-up biological TMV self-assembly and metallization was combined with traditional thin film deposition techniques. The main method that was explored was atomic layer deposition, due to its high suitability in depositing films over complex three-dimensional geometries with high degree of control over thickness. As a result, a unique electrode architecture has been developed where every TMV contains a metallic nickel core and an active material shell. From a battery standpoint, this constitutes a novel approach as it eliminates the need for binders and other conductive additives that are commonly used in ink-casted electrodes. This in turn enables the fabrication of highly porous nanostructured electrodes directly on current collectors and allows integration in microfabricated architectures.

Finally, challenges were involved in the electrochemical characterization of the MEMS devices. In previous published work, most MEMS microbatteries were tested inside argon filled glove boxes, since exposure of a Li-ion battery to moisture results in catastrophic failure. In this research, packaging and assembly techniques were

devised that facilitate testing outside a glove box in a reliable, repeatable manner. First, a teflon/stainless steel sandwiched cell was machined that enabled hermetic sealing of the device and electrical connections from the top-side of the apparatus. This approach was used in the first round of experimental testing which verified the functionality of the 3D hierarchical electrodes. In order to achieve highly parallel testing of multiple microbattery electrodes, the fabrication process was adjusted to create a back side metallic contact on the silicon chips. This allowed for assembly and testing inside standard coin cells, speeding up testing and experimental characterization.

6.2 Summary of Accomplishments

In summary, the main accomplishments of this work are summarized below:

1. Patterned-assembly and synthesis of TMV scaffolds

- Photolithographic patterning of coated TMV using lift-off with resolution as low as 2 μm , limited only by mask feature size and contact alignment mode
- Photolithographic patterning of uncoated TMV using lift-off in acetone and buffered developer, with retention of chemical functionality after patterning
- Assembly of metalized TMV in 3D geometries fabricated using commonly used MEMS materials, such as silicon, polymers and electroplated metals
- Synthesis of core/shell nanostructures by combining Ni-coated TMV with ALD thin-film deposition of TiO_2 and V_2O_5

2. Core/Shell nanocomposite electrodes for Li-ion batteries

- Ni/TiO₂ anodes with improved gravimetric capacity and rate capability compared to flat TiO₂ films as a result of increased surface area
- Ni/V₂O₅ cathodes with an up to 8-fold increase in energy density per unit area compared to flat V₂O₅ electrodes

3. Hierarchical three-dimensional microbattery electrodes

- Integration of bottom-up self-assembly with top-down microfabrication for the development of electrodes with both micro and nano components
- 3-fold increase in mass loading as a result of a 3-fold increase in surface area for hierarchical electrodes compared to electrodes with nanostructures alone
- 3-fold increase in energy density for several current densities and C-rates, showing scaling of capacity with simultaneous power density retention

6.3 Future Outlook

Based on the lessons learned during the fabrication technology development as well as the experimental results on the hierarchical electrodes, key areas were identified for future improvement. These address aspects of the work ranging from building block components, electrode and electrolyte materials, as well as fabrication processes that can further enhance device performance. These areas are addressed in the following sub-sections.

6.3.1 TMV coating

An area of research that will be in the fore front of future activities is the expansion of available materials for TMV coating. As indicated from the experimental analysis in Chapter 4, the existence of the metallic core is critical in the development of the self-assembled surface-attached electrodes as well as their improved electrochemical performance. However, it was observed that nickel can result in background capacities due to its electrochemical activity in wide range of voltage versus lithium. As a result, the development of more stable anode materials can be improved through the development of electrochemically inactive TMV coatings that serve as the core of the nanocomposite geometries. Such materials include gold, copper and aluminum, for which chemical synthesis techniques directly on the TMV must be developed, while maintaining the self-assembly characteristics of three-dimensional nano network.

6.3.2 Higher aspect ratio electrodes

The first prototype microbattery electrode geometry was based on a moderate electrode aspect ratio on the range of $\sim 3:1$. This choice was made to demonstrate the merits of this novel technology through a simpler fabrication process. Next-generation electrodes can achieve significantly higher energy densities if higher aspect ratio electrodes are used, which can tune the surface area accordingly. The approach that will be explored is electroplating of micropillars through silicon wafers. More specifically, in this process, hole patterns are etched using DRIE throughout the entire thickness of the wafer, which can result in very high aspect ratios, on the order of up to 25:1, based on previous literature results [125]. The molds can then be

bonded onto carrier wafers with patterned seed layers using established MEMS bonding techniques such as anodic or eutectic bonding. Through modifications in the electroplating set-up and method (for example, pulse plating), the molds can then be filled with metal and create the microstructured component of the electrode with higher surface area. Variations of this approach for even higher available areas can be explored as well, for example through the development of hollow pillars which take advantage of the additional interior circumference of the cylinders. Similarly, other approaches for creating the microstructured component can be pursued, such as carbon nanotube forests which have been shown to have very high aspect ratios [128]. All these approaches are compatible with the TMV self-assembly and can result in geometries with extremely high energy densities.

6.3.3 All-solid-state virus-structured microbatteries

In parallel with the improvements on the fabrication schemes for the hierarchical electrode components, simultaneous advancements in the electrode and electrolyte materials are necessary to alleviate a practical limitation in microbattery development, efficient packaging and integration in microsystems. In the current work, all devices were tested using liquid organic electrolytes and used lithium foil as the counter electrode. A device that is based on a lithium containing thin-film cathode and electrolyte will facilitate much simpler assembly.

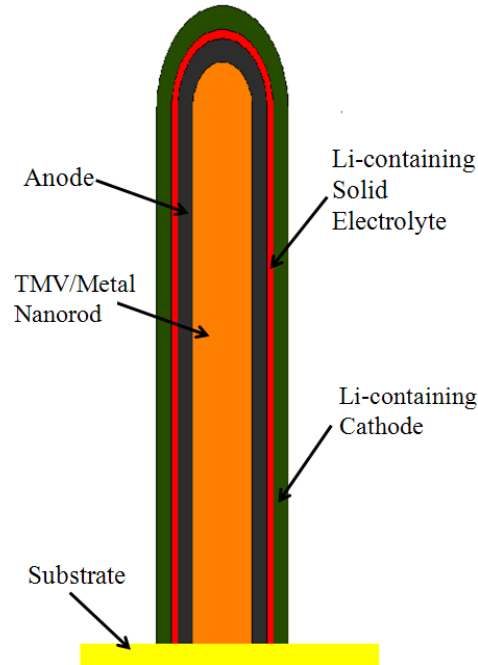


Figure 6.1: Conceptual schematic of envisioned battery architecture on a single virus nanoparticle

A conceptual schematic of the desired architecture is shown in Figure 6.1. The TMV metalized nanorod serves as the scaffold for the sequentially assembly of battery components. Specifically, anode, electrolyte and cathode can be developed conformally using a CVD or ALD process on the three-dimensional nano network, where a nanobattery is formed on every single virus particle. This envisioned architecture will greatly simplify device fabrication, since a single electroplating step can be used to form the three-dimensional micropillars, followed by the self-assembly and thin-film deposition as outlined in Figure 6.1. Such an all-solid-state microbattery device can be very easily integrated with other components of a microsystem and it requires minimal additional space for packaging and electrical interface. To accomplish this geometry, significant research focus must be directed towards novel processes for ALD based materials synthesis with lithium.

Bibliography

- [1] J. W. Judy, "Microelectromechanical systems (MEMS): fabrication, design and applications," *Smart Materials & Structures*, vol. 10, pp. 1115-1134, Dec 2001.
- [2] B. Warneke, M. Last, B. Liebowitz, and K. S. J. Pister, "Smart dust: Communicating with a cubic-millimeter computer," *Computer*, vol. 34, pp. 44-+, Jan 2001.
- [3] J. W. Long, B. Dunn, D. R. Rolison, and H. S. White, "Three-dimensional battery architectures," *Chemical Reviews*, vol. 104, pp. 4463-4492, Oct 2004.
- [4] J. N. Harb, R. M. LaFollette, R. H. Selfridge, and L. L. Howell, "Microbatteries for self-sustained hybrid micropower supplies," *Journal Of Power Sources*, vol. 104, pp. 46-51, Jan 2002.
- [5] T. S. Arthur, D. J. Bates, N. Cirigliano, D. C. Johnson, P. Malati, J. M. Mosby, E. Perre, M. T. Rawls, A. L. Prieto, and B. Dunn, "Three-dimensional electrodes and battery architectures," *Mrs Bulletin*, vol. 36, pp. 523-531, Jul 2011.
- [6] R. W. Hart, H. S. White, B. Dunn, and D. R. Rolison, "3-D microbatteries," *Electrochemistry Communications*, vol. 5, pp. 120-123, Feb 2003.
- [7] G. T. Teixidor, R. B. Zaouk, B. Y. Park, and M. J. Madou, "Fabrication and characterization of three-dimensional carbon electrodes for lithium-ion batteries," *Journal Of Power Sources*, vol. 183, pp. 730-740, Sep 1 2008.

- [8] Y. G. Guo, J. S. Hu, and L. J. Wan, "Nanostructured Materials for Electrochemical Energy Conversion and Storage Devices (vol 20, pg 2878, 2008)," *Advanced Materials*, vol. 20, pp. 4384-4384, Dec 2 2008.
- [9] P. G. Bruce, B. Scrosati, and J. M. Tarascon, "Nanomaterials for rechargeable lithium batteries," *Angewandte Chemie-International Edition*, vol. 47, pp. 2930-2946, 2008.
- [10] M. Beidaghi, W. Chen, and C. L. Wang, "Electrochemically activated carbon micro-electrode arrays for electrochemical micro-capacitors," *Journal Of Power Sources*, vol. 196, pp. 2403-2409, Feb 2011.
- [11] Y. Q. Jiang, Q. Zhou, and L. Lin, "Planar MEMS Supercapacitor using Carbon Nanotube Forests," in *Micro Electro Mechanical Systems, 2009. MEMS 2009. IEEE 22nd International Conference on*, 2009, pp. 587-590.
- [12] J. Chmiola, C. Largeot, P. L. Taberna, P. Simon, and Y. Gogotsi, "Monolithic Carbide-Derived Carbon Films for Micro-Supercapacitors," *Science*, vol. 328, pp. 480-483, Apr 2010.
- [13] P. C. Su, C. C. Chao, J. H. Shim, R. Fasching, and F. B. Prinz, "Solid oxide fuel cell with corrugated thin film electrolyte," *Nano Letters*, vol. 8, pp. 2289-2292, Aug 2008.
- [14] T. Kim and S. Kwon, "Design, fabrication and testing of a catalytic microreactor for hydrogen production," *Journal Of Micromechanics And Microengineering*, vol. 16, pp. 1760-1768, Sep 2006.

- [15] B. Y. Park and M. J. Madou, "Design, fabrication, and initial testing of a miniature PEM fuel cell with micro-scale pyrolyzed carbon fluidic plates," *Journal Of Power Sources*, vol. 162, pp. 369-379, Nov 2006.
- [16] J. D. Morse, R. S. Upadhye, R. T. Graff, C. Spadaccini, H. G. Park, and E. K. Hart, "A MEMS-based reformed methanol fuel cell for portable power," *Journal Of Micromechanics And Microengineering*, vol. 17, pp. S237-S242, Sep 2007.
- [17] T. Kim, J. S. Hwang, and S. Kwon, "A MEMS methanol reformer heated by decomposition of hydrogen peroxide," *Lab on a Chip*, vol. 7, pp. 835-841, 2007.
- [18] L. Hsi-wen and T. Yu-Chong, "Parylene-HT-based electret rotor generator," in *Micro Electro Mechanical Systems, 2008. MEMS 2008. IEEE 21st International Conference on*, 2008, pp. 984-987.
- [19] D. P. Arnold, F. Herrault, I. Zana, P. Galle, J. W. Park, S. Das, J. H. Lang, and M. G. Allen, "Design optimization of an 8 W, microscale, axial-flux, permanent-magnet generator," *Journal Of Micromechanics And Microengineering*, vol. 16, pp. S290-S296, Sep 2006.
- [20] H. B. Fang, J. Q. Liu, Z. Y. Xu, L. Dong, L. Wang, D. Chen, B. C. Cai, and Y. Liu, "Fabrication and performance of MEMS-based piezoelectric power generator for vibration energy harvesting," *Microelectronics Journal*, vol. 37, pp. 1280-1284, Nov 2006.

- [21] Y. B. Jeon, R. Sood, J. H. Jeong, and S. G. Kim, "MEMS power generator with transverse mode thin film PZT," *Sensors And Actuators A-Physical*, vol. 122, pp. 16-22, Jul 2005.
- [22] W. Glatz, S. Muntwyler, and C. Hierold, "Optimization and fabrication of thick flexible polymer based micro thermoelectric generator," *Sensors And Actuators A-Physical*, vol. 132, pp. 337-345, Nov 2006.
- [23] K. B. Lee and L. W. Lin, "Electrolyte-based on-demand and disposable microbattery," *Journal Of Microelectromechanical Systems*, vol. 12, pp. 840-847, Dec 2003.
- [24] F. Sammoura, K. B. Lee, and L. W. Lin, "Water-activated disposable and long shelf life microbatteries," *Sensors And Actuators A-Physical*, vol. 111, pp. 79-86, Mar 1 2004.
- [25] H. Jimbo and N. Miki, "Gastric-fluid-utilizing micro battery for micro medical devices," *Sensors and Actuators B-Chemical*, vol. 134, pp. 219-224, Aug 2008.
- [26] P. H. Humble, J. N. Harb, and R. LaFollette, "Microscopic nickel-zinc batteries for use in autonomous microsystems," *Journal Of The Electrochemical Society*, vol. 148, pp. A1357-A1361, Dec 2001.
- [27] P. Singh, S. Kaneria, V. S. Anugonda, H. M. Chen, X. Q. Wang, D. E. Reisner, and R. M. LaFollette, "Prototype silicon micropower supply for sensors," *Ieee Sensors Journal*, vol. 6, pp. 211-222, Feb 2006.
- [28] F. Albano, Y. S. Lin, D. Blaauw, D. M. Sylvester, K. D. Wise, and A. M. Sastry, "A fully integrated microbattery for an implantable

- microelectromechanical system," *Journal Of Power Sources*, vol. 185, pp. 1524-1532, Dec 2008.
- [29] J. B. Bates, N. J. Dudney, B. Neudecker, A. Ueda, and C. D. Evans, "Thin-film lithium and lithium-ion batteries," *Solid State Ionics*, vol. 135, pp. 33-45, Nov 2000.
- [30] B. J. Neudecker, N. J. Dudney, and J. B. Bates, "'Lithium-free" thin-film battery with in situ plated Li anode," *Journal Of The Electrochemical Society*, vol. 147, pp. 517-523, Feb 2000.
- [31] W. C. West, J. F. Whitacre, V. White, and B. V. Ratnakumar, "Fabrication and testing of all solid-state microscale lithium batteries for microspacecraft applications," *Journal Of Micromechanics And Microengineering*, vol. 12, pp. 58-62, Jan 2002.
- [32] B. Fleutot, B. Pecquenard, F. Le Cras, B. Delis, H. Martinez, L. Dupont, and D. Guy-Bouyssou, "Characterization of all-solid-state Li/LiPONB/TiOS microbatteries produced at the pilot scale," *Journal Of Power Sources*, vol. 196, pp. 10289-10296, Dec 2011.
- [33] K. Dokko, J. Sugaya, H. Nakano, T. Yasukawa, T. Matsue, and K. Kanamura, "Sol-gel fabrication of lithium-ion microarray battery," *Electrochemistry Communications*, vol. 9, pp. 857-862, May 2007.
- [34] C. C. Ho, J. W. Evans, and P. K. Wright, "Direct write dispenser printing of a zinc microbattery with an ionic liquid gel electrolyte," *Journal Of Micromechanics And Microengineering*, vol. 20, Oct 2010.

- [35] H. S. Min, B. Y. Park, L. Taherabadi, C. L. Wang, Y. Yeh, R. Zaouk, M. J. Madou, and B. Dunn, "Fabrication and properties of a carbon/polypyrrole three-dimensional microbattery," *Journal Of Power Sources*, vol. 178, pp. 795-800, Apr 1 2008.
- [36] C. L. Wang, L. Taherabadi, G. Y. Jia, M. Madou, Y. T. Yeh, and B. Dunn, "C-MEMS for the manufacture of 3D microbatteries," *Electrochemical And Solid State Letters*, vol. 7, pp. A435-A438, 2004.
- [37] F. Chamran, Y. Yeh, H. S. Min, B. Dunn, and C. J. Kim, "Fabrication of high-aspect-ratio electrode arrays for three-dimensional microbatteries," *Journal Of Microelectromechanical Systems*, vol. 16, pp. 844-852, Aug 2007.
- [38] F. Chamran, M. Hong-Seok, B. Dunn, and K. Chang-Jin, "Zinc-air microbattery with electrode array of zinc microposts," in *Micro Electro Mechanical Systems, 2007. MEMS. IEEE 20th International Conference on*, 2007, pp. 871-874.
- [39] A. Armutlulu, Y. Fang, S. H. Kim, C. H. Ji, S. A. B. Allen, and M. G. Allen, "A MEMS-enabled 3D zinc-air microbattery with improved discharge characteristics based on a multilayer metallic substructure," *Journal Of Micromechanics And Microengineering*, vol. 21, Oct 2011.
- [40] M. Nathan, D. Golodnitsky, V. Yufit, E. Strauss, T. Ripenbein, I. Shechtman, S. Menkin, and E. Peled, "Three-dimensional thin-film Li-ion microbatteries for autonomous MEMS," *Journal Of Microelectromechanical Systems*, vol. 14, pp. 879-885, Oct 2005.

- [41] D. Golodnitsky, V. Yufit, M. Nathan, I. Shechtman, T. Ripenbein, E. Strauss, S. Menkin, and E. Peled, "Advanced materials for the 3D microbattery," *Journal Of Power Sources*, vol. 153, pp. 281-287, Feb 28 2006.
- [42] M. Kotobuki, Y. Suzuki, H. Munakata, K. Kanamura, Y. Sato, K. Yamamoto, and T. Yoshida, "Fabrication of Three-Dimensional Battery Using Ceramic Electrolyte with Honeycomb Structure by Sol-Gel Process," *Journal Of The Electrochemical Society*, vol. 157, pp. A493-A498, 2010.
- [43] P. H. L. Notten, F. Roozeboom, R. A. H. Niessen, and L. Baggetto, "3-D integrated all-solid-state rechargeable batteries," *Advanced Materials*, vol. 19, pp. 4564-4567, Dec 17 2007.
- [44] J. F. M. Oudenhoven, L. Baggetto, and P. H. L. Notten, "All-Solid-State Lithium-Ion Microbatteries: A Review of Various Three-Dimensional Concepts," *Advanced Energy Materials*, vol. 1, pp. 10-33, Jan 1.
- [45] L. Baggetto, J. F. M. Oudenhoven, T. van Dongen, J. H. Klootwijk, M. Mulder, R. A. H. Niessen, M. de Croon, and P. H. L. Notten, "On the electrochemistry of an anode stack for all-solid-state 3D-integrated batteries," *Journal Of Power Sources*, vol. 189, pp. 402-410, Apr 1 2009.
- [46] L. Baggetto, H. C. M. Knoops, R. A. H. Niessen, W. M. M. Kessels, and P. H. L. Notten, "3D negative electrode stacks for integrated all-solid-state lithium-ion microbatteries," *Journal Of Materials Chemistry*, vol. 20, pp. 3703-3708, 2010.

- [47] N. C. Li, C. R. Martin, and B. Scrosati, "A high-rate, high-capacity, nanostructured tin oxide electrode," *Electrochemical and Solid State Letters*, vol. 3, pp. 316-318, Jul 2000.
- [48] Z. J. Zhang, C. Dewan, S. Kothari, S. Mitra, and D. Teeters, "Carbon nanotube synthesis, characteristics, and microbattery applications," *Materials Science and Engineering B-Solid State Materials for Advanced Technology*, vol. 116, pp. 363-368, Feb 2005.
- [49] X. Chen, Pomerantseva, E., Banerjee, P., Gregorcyk, K., Ghodssi, R., Rubloff, G. , "Ozone-based Atomic Layer Deposition of Crystalline V₂O₅ Films for High Performance Electrochemical Energy Storage " *Chemistry Of Materials*, 2011.
- [50] M. M. Shaijumon, E. Perre, B. Daffos, P. L. Taberna, J. M. Tarascon, and P. Simon, "Nanoarchitected 3D Cathodes for Li-Ion Microbatteries," *Advanced Materials*, vol. 22, pp. 4978-+, Nov 2010.
- [51] S. K. Cheah, E. Perre, M. Rooth, M. Fondell, A. Harsta, L. Nyholm, M. Boman, T. Gustafsson, J. Lu, P. Simon, and K. Edstrom, "Self-Supported Three-Dimensional Nanoelectrodes for Microbattery Applications," *Nano Letters*, vol. 9, pp. 3230-3233, Sep 2009.
- [52] G. F. Ortiz, I. Hanzu, T. Djenizian, P. Lavela, J. L. Tirado, and P. Knauth, "Alternative Li-Ion Battery Electrode Based on Self-Organized Titania Nanotubes," *Chemistry Of Materials*, vol. 21, pp. 63-67, Jan 13 2009.
- [53] G. F. Ortiz, I. Hanzu, P. Knauth, P. Lavela, J. L. Tirado, and T. Djenizian, "TiO₂ nanotubes manufactured by anodization of Ti thin films for on-chip

- Li-ion 2D microbatteries," *Electrochimica Acta*, vol. 54, pp. 4262-4268, Jul 2009.
- [54] C. K. Chan, H. L. Peng, G. Liu, K. McIlwrath, X. F. Zhang, R. A. Huggins, and Y. Cui, "High-performance lithium battery anodes using silicon nanowires," *Nature Nanotechnology*, vol. 3, pp. 31-35, Jan 2008.
- [55] L. F. Cui, R. Ruffo, C. K. Chan, H. L. Peng, and Y. Cui, "Crystalline-Amorphous Core-Shell Silicon Nanowires for High Capacity and High Current Battery Electrodes," *Nano Letters*, vol. 9, pp. 491-495, Jan 2009.
- [56] L. F. Cui, Y. Yang, C. M. Hsu, and Y. Cui, "Carbon-Silicon Core-Shell Nanowires as High Capacity Electrode for Lithium Ion Batteries," *Nano Letters*, vol. 9, pp. 3370-3374, Sep 2009.
- [57] W. Wang, R. Epur, and P. N. Kumta, "Vertically aligned silicon/carbon nanotube (VASCNT) arrays: Hierarchical anodes for lithium-ion battery," *Electrochemistry Communications*, vol. 13, pp. 429-432, May 2011.
- [58] X. L. Chen, "Tobacco mosaic virus Based Three Dimensional Anodes for Lithium Ion Batteries," Doctor of Philosophy, Department of Chemical and Biomolecular Engineering University of Maryland, College Park 2011.
- [59] N. Ma, E. H. Sargent, and S. O. Kelley, "Biotemplated nanostructures: directed assembly of electronic and optical materials using nanoscale complementarity " *Journal of Materials Chemistry*, vol. 18, pp. 954-964, 2007.
- [60] S. Sotiropoulou, Y. Sierra-Sastre, S. S. Mark, and C. A. Batt, "Biotemplated Nanostructured Materials," *Chem. Mater.*, vol. 20, pp. 821-834, Jan 17 2008.

- [61] S. Sotiropoulou, Y. Sierra-Sastre, S. S. Mark, and C. A. Batt, "Biotemplated nanostructured materials," *Chemistry Of Materials*, vol. 20, pp. 821-834, Feb 12 2008.
- [62] J. Y. Huang, X. D. Wang, and Z. L. Wang, "Controlled replication of butterfly wings for achieving tunable photonic properties," *Nano Letters*, vol. 6, pp. 2325-2331, Oct 2006.
- [63] E. K. Payne, N. L. Rosi, C. Xue, and C. A. Mirkin, "Sacrificial biological templates for the formation of nanostructured metallic microshells," *Angewandte Chemie-International Edition*, vol. 44, pp. 5064-5067, 2005.
- [64] Q. Gu, C. Cheng, T. Gonela, S. Suryanarayanan, S. Anabathula, K. Dai, and D. T. Haynie, "DNA nanowire fabrication," *Nanotechnology*, vol. 17, pp. R14-R25, 2006.
- [65] Z. Deng and C. Mao, "DNA- Templated Fabrication of 1D Parallel and 2D Crossed Metallic Nanowire Arrays," *NANO Letters*, vol. 3, pp. 1545-1548, Sept 30 2003.
- [66] Y. Hashimoto, Y. Matsuo, and K. Ijiri, "Fabrication of Silver Nanowires by Selective Electroless Plating of DNA Stretched Using the LB Method," *Chemistry Letters*, vol. 34, 2005.
- [67] J. M. Kinsella and A. Ivanisevic, "DNA-Templated Magnetic Nanowires with Different Compositions: Fabrication and Analysis," *Langmuir*, vol. 23, pp. 3886-3890, 2007.

- [68] H. Kudo and M. Fujihira, "DNA-Templated Copper Nanowire Fabrication by a Two-Step Process Involving Electroless Metallization," *IEEE Transactions on Nanotechnology*, vol. 5, pp. 90-92, March 2006.
- [69] Y. Ma, J. Zhang, G. Zhang, and H. He, "Polyaniline Nanowires on Si Surfaces Fabricated with DNA Templates," *J. Am. Chem. Soc.*, vol. 126, pp. 7097-7101, 2004.
- [70] K. Keren, M. Krueger, R. Gilad, G. Ben-Yospeh, U. Sivan, and E. Braun, "Sequence-Specific Molecular Lithography on Single DNA Molecules," *Science Magazine*, vol. 297, Jul 5 2002.
- [71] M. Reches and E. Gazit, "Casting Metal Nanowires Within Discrete Self-Assembled Peptide Nanotubes," *Science Magazine*, vol. 300, Apr 25 2003.
- [72] X. Liang, J. Liu, S. Li, Y. Mei, and W. Yanqing, "Magnetic and mechanical properties of micro/nano particles prepared by metallizing rod-shaped bacteria," *Materials Letters*, vol. 62, pp. 2999-3002, 2008.
- [73] R. Mogul, J. J. G. Kelly, M. L. Cable, and A. F. Hebard, "Synthesis and magnetic characterization of microstructures prepared from microbial templates of differing morphology," *Materials Letters*, vol. 60, pp. 19-22, 2005.
- [74] B. Zhang, S. A. Davis, N. H. Mendelson, and S. Mann, "Bacterial templating of zeolite fibres with hierarchial structure," *Chem. Commun.*, pp. 781-782, 2000.

- [75] M. T. Kumara, B. C. Tripp, and S. Muralidharan, "Exciton Energy Transfer in Self-Assembled Quantum Dots on Bioengineered Bacterial Flagella Nanotubes," *J. Phys. Chem.*, vol. 111, pp. 5276-5280, 2007.
- [76] D. J. Evans, "The bionanoscience of plant viruses: templates and synthons for new materials," *Journal of Materials Chemistry*, vol. 18, pp. 3746-3754, 2008.
- [77] Y. Huang, C.-Y. Chiang, S. J. Lee, Y. Gao, E. L. Hu, J. D. Yoreo, and A. M. Belcher, "Programmable Assembly of Nanoarchitectures Using Genetically Engineered Viruses," *NANO Letters*, vol. 5, pp. 1429-1434, 2005.
- [78] S.-W. Lee, C. Mao, C. E. Flynn, and A. M. Belcher, "Ordering of Quantum Dots Using Genetically Engineered Viruses," *Science Magazine*, vol. 296, May 3 2002.
- [79] C. Mao, D. J. Solis, B. D. Reiss, S. T. Kottmann, R. Y. Sweeney, A. Hayhurst, G. Georgiou, B. Iverson, and A. M. Belcher, "Virus-based Toolkit for the Direct Synthesis of Magnetic and Semiconducting Nanowires " *Science*, vol. 303, p. 213, 2004.
- [80] K. Keren, M. Krueger, R. Gilad, G. Ben-Yoseph, U. Sivan, and E. Braun, "Sequence-specific molecular lithography on single DNA molecules," *Science*, vol. 297, pp. 72-75, Jul 2002.
- [81] K. T. Nam, D. W. Kim, P. J. Yoo, C. Y. Chiang, N. Meethong, P. T. Hammond, Y. M. Chiang, and A. M. Belcher, "Virus-enabled synthesis and assembly of nanowires for lithium ion battery electrodes," *Science*, vol. 312, pp. 885-888, May 12 2006.

- [82] W. O. Dawson, D. L. Beck, D. A. Knorr, and G. L. Grantham, "CDNA CLONING OF THE COMPLETE GENOME OF TOBACCO MOSAIC-VIRUS AND PRODUCTION OF INFECTIOUS TRANSCRIPTS," *Proceedings of the National Academy of Sciences of the United States of America*, vol. 83, pp. 1832-1836, Mar 1986.
- [83] D. H. Gracias, M. Boncheva, O. Omoregie, and G. M. Whitesides, "Biomimetic self-assembly of helical electrical circuits using orthogonal capillary interactions," *Applied Physics Letters*, vol. 80, pp. 2802-2804, Apr 2002.
- [84] A. A. Balandin and V. A. Fonoberov, "Vibrational Modes of Nano-Template Viruses," *Journal of Biomedical Nanotechnology*, vol. 1, pp. 90-95, Mar 2005.
- [85] S. Y. Lee, E. Royston, J. N. Culver, and M. T. Harris, "Improved metal cluster deposition on a genetically engineered tobacco mosaic virus template," *Nanotechnology*, vol. 16, pp. S435-S441, Jul 2005.
- [86] M. Knez, A. Kadri, C. Wege, U. Gosele, H. Jeske, and K. Nielsch, "Atomic layer deposition on biological macromolecules: Metal oxide coating of tobacco mosaic virus and ferritin," *Nano Letters*, vol. 6, pp. 1172-1177, Jun 2006.
- [87] M. Knez, A. M. Bittner, F. Boes, C. Wege, H. Jeske, E. Maiss, and K. Kern, "Biotemplate synthesis of 3-nm nickel and cobalt nanowires," *Nano Letters*, vol. 3, pp. 1079-1082, Aug 2003.
- [88] M. Knez, M. Sumser, A. M. Bittner, C. Wege, H. Jeske, S. Kooi, M. Burghard, and K. Kern, "Electrochemical modification of individual nano-

- objects," *Journal of Electroanalytical Chemistry*, vol. 522, pp. 70-74, Mar 2002.
- [89] M. Knez, M. Sumser, A. M. Bittner, C. Wege, H. Jeske, T. P. Martin, and K. Kern, "Spatially selective nucleation of metal clusters on the tobacco mosaic virus," *Advanced Functional Materials*, vol. 14, pp. 116-124, Feb 2004.
- [90] E. Royston, "Assembly of inorganic nanomaterials using Tobacco mosaic virus," Doctor of Philosophy, Department of Chemical Engineering, Purdue University, Indiana, 2007.
- [91] E. Royston, A. Ghosh, P. Kofinas, M. T. Harris, and J. N. Culver, "Self-assembly of virus-structured high surface area nanomaterials and their application as battery electrodes," *Langmuir*, vol. 24, pp. 906-912, Feb 5 2008.
- [92] G. V. Gooding and T. T. Hebert, "A SIMPLE TECHNIQUE FOR PURIFICATION OF TOBACCO MOSAIC VIRUS IN LARGE QUANTITIES," *Phytopathology*, vol. 57, pp. 1285-&, 1967.
- [93] M. L. Gorzny, A. S. Walton, M. Wnek, P. G. Stockley, and S. D. Evans, "Four-probe electrical characterization of Pt-coated TMV-based nanostructures," *Nanotechnology*, vol. 19, Apr 2008.
- [94] R. J. Tseng, C. L. Tsai, L. P. Ma, and J. Y. Ouyang, "Digital memory device based on tobacco mosaic virus conjugated with nanoparticles," *Nature Nanotechnology*, vol. 1, pp. 72-77, Oct 2006.

- [95] E. Royston, S.-Y. Lee, J. N. Culver, and M. T. Harris, "Characterization of silica-coated tobacco mosaic virus," *Journal of Colloid and Interface Science*, vol. 298, pp. 706-712, 2006.
- [96] S.-Y. Lee, E. Royston, J. N. Culver, and M. T. Harris, "Improved metal cluster deposition on a genetically engineered tobacco mosaic virus template," *Nanotechnology*, vol. 16, pp. S435-S441, 2005.
- [97] K. Gerasopoulos, M. McCarthy, E. Royston, J. N. Culver, and R. Ghodssi, "Nanostructured nickel electrodes using the Tobacco mosaic virus for microbattery applications," *Journal Of Micromechanics And Microengineering*, vol. 18, Oct 2008.
- [98] E. S. Royston, A. D. Brown, M. T. Harris, and J. N. Culver, "Preparation of silica stabilized Tobacco mosaic virus templates for the production of metal and layered nanoparticles," *Journal Of Colloid And Interface Science*, vol. 332, pp. 402-407, Apr 15 2009.
- [99] C. L. Cheung, J. A. Camarero, B. W. Woods, T. Lin, J. E. Johnson, and J. J. D. Yoreo, "Fabrication of Assembled Virus Nanostructures on Templates of Chemoselective Linkers Formed by Scanning Probe Nanolithography," *Journal of the American Chemical Society*, vol. 125, pp. 6848-6849, 2003.
- [100] R. D. Piner, J. Zhu, F. Xu, S. Hong, and C. A. Mirkin, "'Dip-Pen' Nanolithography," *Science Magazine*, vol. 283, pp. 661-663, 1999.
- [101] K. Kobayashi, N. Tonegawa, S. Fujii, J. Hikida, H. Nozoye, K. Tsutsui, Y. Wada, M. Chikira, and M.-a. Haga, "Fabrication of DNA Nanowires by

- Orthogonal Self-Assembly and DNA Intercalation on a Au Patterned Si/SiO₂ Surface," *Langmuir*, vol. 24, pp. 13203-13211, 2008.
- [102] P. W. K. Rothmund, "Folding DNA to create nanoscale shapes and patterns," *Nature*, vol. 440, pp. 297-302, 2006.
- [103] S. Balci, D. M. Leinberger, M. Knez, A. M. Bittner, F. Boes, A. Kadri, C. Wege, H. Jeske, and K. Kern, "Printing and Aligning Mesoscale Patterns of Tobacco Mosaic Virus on Surfaces," *Advanced Materials*, vol. 20, pp. 2195-2200, 2008.
- [104] A. Bernard, J. P. Renault, B. Michel, H. R. Bosshard, and E. Delamarche, "Microcontact Printing of Proteins," *Advanced Materials*, vol. 12, pp. 1067-1070, 2000.
- [105] H. Yi, S. Nisar, S.-Y. Lee, M. A. Powers, W. E. Bentley, G. F. Payne, R. Ghodssi, G. W. Rubloff, M. T. Harris, and J. N. Culver, "Patterned Assembly of Genetically Modified Viral Nanotemplates via Nucleic Acid Hybridization," *NANO Letters*, vol. 5, pp. 1931-1936, 2005.
- [106] H. Yi, G. W. Rubloff, and J. N. Culver, "TMV Microarrays: Hybridization-Based Assembly of DNA-Programmed Viral Nanotemplates," *Langmuir*, vol. 23, pp. 2663-2667, 2007.
- [107] H. M. Yi, S. Nisar, S. Y. Lee, M. A. Powers, W. E. Bentley, G. F. Payne, R. Ghodssi, G. W. Rubloff, M. T. Harris, and J. N. Culver, "Patterned assembly of genetically modified viral nanotemplates via nucleic acid hybridization," *Nano Letters*, vol. 5, pp. 1931-1936, Oct 2005.

- [108] K. Gerasopoulos, M. McCarthy, P. Banerjee, X. Fan, J. N. Culver, and R. Ghodssi, "Biofabrication methods for the patterned assembly and synthesis of viral nanotemplates," *Nanotechnology*, vol. 21, Feb 5 2010.
- [109] A. W. Ott, J. W. Klaus, J. M. Johnson, and S. M. George, "Al₂O₃ thin film growth on Si (100) using binary reaction sequence chemistry (vol 292, pg 135, 1997)," *Thin Solid Films*, vol. 517, pp. 5950-5950, Aug 2009.
- [110] A. R. Spurr, "A LOW-VISCOSITY EPOXY RESIN EMBEDDING MEDIUM FOR ELECTRON MICROSCOPY," *Journal of Ultrastructure Research*, vol. 26, pp. 31-&, 1969.
- [111] R. E. M. McCarthy, K. Gerasopoulos, J. N. Culver, R. Ghodssi, E. Wang, "Biomimetic Superhydrophobic Surfaces Using Viral Nanotemplates for Self-cleaning and Drop-wise Condensation," in *2010 Solid-state sensor, actuator, and microsystems workshop (Hilton Head 2010)*, , Hilton Head Island, SC, USA, 2010.
- [112] K. Gerasopoulos, X. L. Chen, J. Culver, C. S. Wang, and R. Ghodssi, "Self-assembled Ni/TiO₂ nanocomposite anodes synthesized via electroless plating and atomic layer deposition on biological scaffolds," *Chemical Communications*, vol. 46, pp. 7349-7351, 2010.
- [113] X. L. Chen, K. Gerasopoulos, J. C. Guo, A. Brown, C. S. Wang, R. Ghodssi, and J. N. Culver, "Virus-Enabled Silicon Anode for Lithium-Ion Batteries," *Acs Nano*, vol. 4, pp. 5366-5372, Sep 2010.
- [114] S. W. Kim, T. H. Han, J. Kim, H. Gwon, H. S. Moon, S. W. Kang, S. O. Kim, and K. Kang, "Fabrication and Electrochemical Characterization of TiO₂

- Three-Dimensional Nanonetwork Based on Peptide Assembly," *Acs Nano*, vol. 3, pp. 1085-1090, May 2009.
- [115] Y. J. Lee, H. Yi, W. J. Kim, K. Kang, D. S. Yun, M. S. Strano, G. Ceder, and A. M. Belcher, "Fabricating Genetically Engineered High-Power Lithium-Ion Batteries Using Multiple Virus Genes," *Science*, vol. 324, pp. 1051-1055, May 22 2009.
- [116] K. T. Nam, R. Wartena, P. J. Yoo, F. W. Liao, Y. J. Lee, Y. M. Chiang, P. T. Hammond, and A. M. Belcher, "Stamped microbattery electrodes based on self-assembled M13 viruses," *Proceedings Of The National Academy Of Sciences Of The United States Of America*, vol. 105, pp. 17227-17231, Nov 11 2008.
- [117] Y. G. Guo, Y. S. Hu, W. Sigle, and J. Maier, "Superior electrode performance of nanostructured mesoporous TiO₂ (anatase) through efficient hierarchical mixed conducting networks," *Advanced Materials*, vol. 19, pp. 2087-+, Aug 17 2007.
- [118] Z. G. Yang, D. Choi, S. Kerisit, K. M. Rosso, D. H. Wang, J. Zhang, G. Graff, and J. Liu, "Nanostructures and lithium electrochemical reactivity of lithium titanates and titanium oxides: A review," *Journal of Power Sources*, vol. 192, pp. 588-598, Jul 2009.
- [119] L. Kavan, J. Rathousky, M. Gratzel, V. Shklover, and A. Zukal, "Surfactant-templated TiO₂ (anatase): Characteristic features of lithium insertion electrochemistry in organized nanostructures," *Journal of Physical Chemistry B*, vol. 104, pp. 12012-12020, Dec 2000.

- [120] D. H. Wang, D. W. Choi, J. Li, Z. G. Yang, Z. M. Nie, R. Kou, D. H. Hu, C. M. Wang, L. V. Saraf, J. G. Zhang, I. A. Aksay, and J. Liu, "Self-Assembled TiO(2)-Graphene Hybrid Nanostructures for Enhanced Li-Ion Insertion," *Acs Nano*, vol. 3, pp. 907-914, Apr 2009.
- [121] M. Wagemaker, W. J. H. Borghols, and F. M. Mulder, "Large impact of particle size on insertion reactions. A case for anatase Li_xTiO_2 ," *Journal of the American Chemical Society*, vol. 129, pp. 4323-4327, Apr 2007.
- [122] E. Hosono, S. Fujihara, I. Honma, and H. S. Zhou, "The high power and high energy densities Li ion storage device by nanocrystalline and mesoporous Ni/NiO covered structure," *Electrochemistry Communications*, vol. 8, pp. 284-288, Feb 2006.
- [123] M. S. Whittingham, "Lithium batteries and cathode materials," *Chemical Reviews*, vol. 104, pp. 4271-4301, Oct 2004.
- [124] E. Pomerantseva, Gerasopoulos, K., Chen, X., Rubloff, G. Ghodssi, R. , "Electrochemical performance of the nanostructured biotemplated V_2O_5 cathode for lithium-ion batteries," *Journal Of Power Sources*, 2011.
- [125] P. Dixit, C. W. Tan, L. H. Xu, N. Lin, J. M. Miao, J. H. L. Pang, P. Backus, and R. Preisser, "Fabrication and characterization of fine pitch on-chip copper interconnects for advanced wafer level packaging by a high aspect ratio through AZ9260 resist electroplating," *Journal Of Micromechanics And Microengineering*, vol. 17, pp. 1078-1086, May 2007.
- [126] A. R. Sankar, S. K. Lahiri, and S. Das, "Performance enhancement of a silicon MEMS piezoresistive single axis accelerometer with electroplated gold on a

proof mass," *Journal of Micromechanics and Microengineering*, vol. 19, Feb 2009.

- [127] C. Navone, J. P. Pereira-Ramos, R. Baddour-Hadjean, and R. Salot, "High-capacity crystalline V₂O₅ thick films prepared by RF sputtering as positive electrodes for rechargeable lithium microbatteries," *Journal Of The Electrochemical Society*, vol. 153, pp. A2287-A2293, 2006.
- [128] M. De Volder, S. H. Tawfick, S. J. Park, D. Copic, Z. Zhao, W. Lu, and A. J. Hart, "Diverse 3D Microarchitectures Made by Capillary Forming of Carbon Nanotubes," *Advanced Materials*, vol. 22, pp. 4384-4389, 2010.